# Conceptual Design and Performance Analysis of an Expander for the Recovery of Potential Energy Stored in Compressed Hydrogen

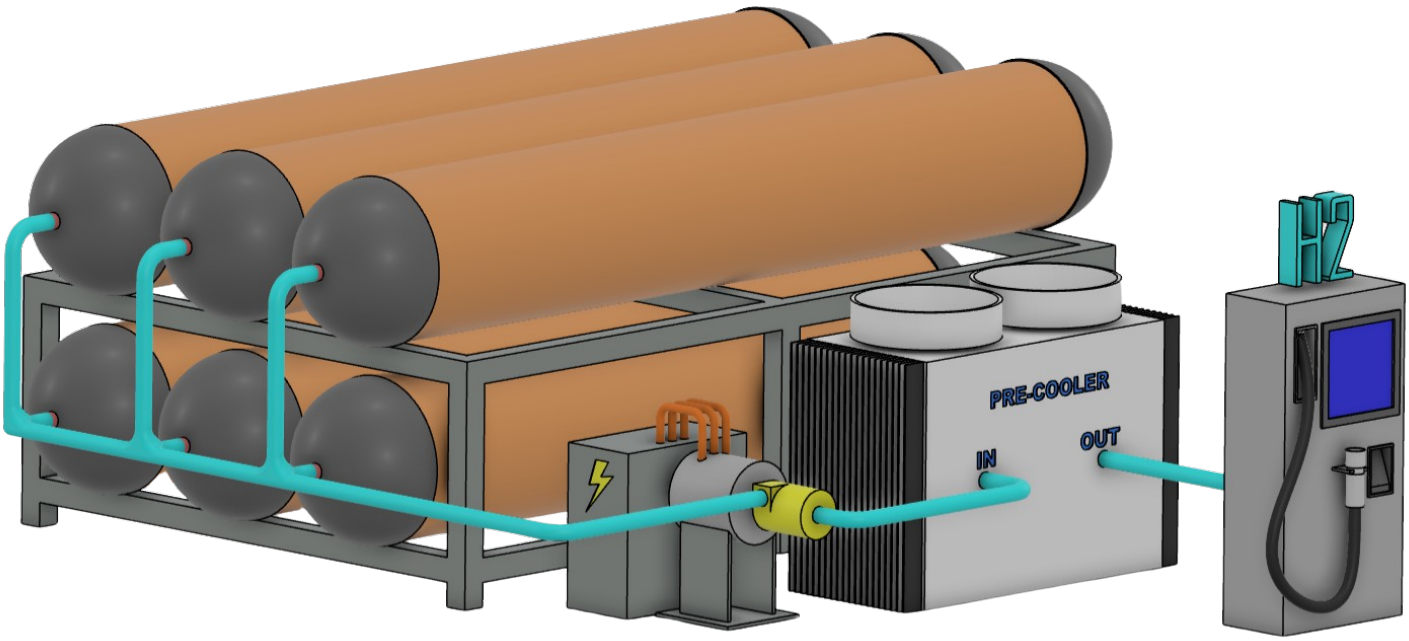


4533461 Tuur Knevels

April 30, 2024

# Conceptual Design and Performance Analysis of an Expander for the Recovery of Potential Energy Stored in Compressed Hydrogen

by

T. Knevels

to obtain the degree of Master of Science
at the Delft University of Technology,
to be defended publicly on the 13th of May, 2024 at 09h00.


| | | |
|---|---|---|
| Student number: | 4533461 | |
| Project duration: | November 1, 2022 - May 13, 2024 | |
| Thesis comittee: | Prof. dr. ir. P. Colonna, | TU Delft, committee chair |
| | Dr. M. Pini, | TU Delft, supervisor |
| | Dr. ir. W. Visser, | TU Delft, supervisor |
| | Ir. P.C. Roling, | TU Delft, external committee member |
| | Ir. A. Lautenschlaeger, | AYED-ENGINEERING GmbH, industrial supervisor |




TU Delft

# Acknowledgements

This thesis would not have been possible without the help and support of many people around me, from the guidance of my supervisors to the unwavering support of friends and family. For that I would like extend a token of gratitude to the following people:

To my weekly supervisors, Wilfried Visser and Alexander Lautenschlager for their continuous advice and guidance throughout the entire thesis project. As well as for their patience with my progress and for their understanding regarding my other endavours.

To my dear parents and my brothers for their continuous support and interest in my work. For supporting me throughout my studies and for allowing me to pursue all the other miscellaneous but tremendously impactful endeavours in life.

To my colleagues at Viritech for their continued support in offering me the possibility to work at flexible times and remotely from Delft. For allowing me to combine work and study and for providing me with an outlook after university.

To all of the amazing friends and connections in BEST for the deep friendships, for keeping me productively distracted, for accepting me working on my thesis at every possible occasion and for letting me sleep on your couches all across Europe.

To my dear friend Hector Ruiz for his unwavering support and for always being able to provide a listening ear, a friend like no other.

To the rest of my friends in Delft, old and new, for always being there on a Friday evening, for providing an outlook on life after graduation and for giving me a place detached from work, study or BEST, even though I will continue to ramble on about them regardless ;)

"*It's all rather complicated, but it makes a kind of sense if you think about it for a while.*"

$\sim$

Douglas Adams

*T. Knevels*
*Delft, April 30, 2024*

# Summary

In the scope of global decarbonisation, hydrogen has been identified as an essential energy carrier. Not only as an energy storage solution for further electrification in vehicles but also as a primary fuel source in processes that rely on chemical energy which cannot be easily electrified. However, at ambient conditions, hydrogen is also a very sparse gas with a low energy density, requiring it to be compressed for efficient storage and transport. This compression is a rather energy-intensive step, and the potential energy that is then stored in the compressed gas is practically always lost when it is eventually expanded through a valve.

This research is aimed at

1. Identifying a suitable application in which an expander could be applied to recover part of the potential energy stored in compressed hydrogen.
2. Providing a conceptual design and a thermodynamical analysis of this expander to assess its efficiency and feasibility.

In a first step, a literature study provided an overview of the current hydrogen landscape and the potential applications in which an expander could be applied. These have been evaluated and led to the selection of a hydrogen refuelling station as a suitable application for this purpose.

The second step was to develop a system model of a hydrogen refuelling station which is able to replicate a refuelling cycle and serve as an operating environment for the to-be-designed expander. This has been performed by modelling the key components in such a system: The storage tanks, the expander, a heat exchanger, the refuelling nozzle and the vehicle tanks. These are modelled for the duration of a single refuelling cycle in which system parameters can easily be adjusted. Concretely, this led to a set of process parameters and boundary conditions for the expander for each time step during the refuelling cycle.

The third step has been to select an expander type and perform initial design calculations. These are repeated for every time step of the process, leading to $n$ potential designs for $n$ time steps, each of which is then evaluated by the use of empirical loss models across the entire operating range. From this, it was possible to find which potential design (each optimised for its corresponding time step) would provide the best overall performance. This selected design and the operating conditions at its optimal performance point have then been used in a 3D CFD validation case using Ansys CFX.

The results indicate that employing a radial inlet turbine for the recovery of potential energy stored in compressed hydrogen in a hydrogen refuelling station can indeed lead to notable operational cost savings but also that there are several remaining practical challenges with this solution, specifically the extremely high rotational speeds required and the miniature design features. To address these, a sensitivity analysis of several system parameters and design assumptions has been included to provide guidance for future work. This does indeed indicate room for improvement in future design iterations.

Similar to previous work on this topic, this study has independently reached comparable conclusions in terms of how much energy can be recovered in this application and the practical challenges that are accompanied by this solution. However, a notable difference is that this work is the first that actually went through a proper and documented design procedure and performance analysis instead of relying on broad performance assumptions. Beyond that, it also covered a CFD validation case, an assessment of the practical limitations and a number of suggestions for future improvement based on a sensitivity analysis.

# Contents

# List of Figures

# List of Tables

# List of abbreviations

| Abbreviation | Definition |
|---|---|
| AFC | Alkaline Fuel Cell |
| APRR | Average Pressure Ramp Rate |
| DC | Direct Current |
| DMFC | Direct Methanol Fuel Cell |
| EDM | Electronic Discharge Machining |
| FC | Fuel Cell |
| GTR | Global Technical Regulations |
| H | Atomic hydrogen |
| $H_2$ | Molecular hydrogen |
| HRS | Hydrogen Refuelling Station |
| HTF | Heat Transfer Fluids |
| HV | High Voltage |
| ICE | Internal Combustion Engine |
| LH2 | Liquid Hydrogen |
| LOHC | Liquid Organic Hydrogen Carrier |
| MCFC | Molten Carbonate Fuel Cell |
| NIST | National Institute of Standards and Technology |
| NREL | National Renewable Energy Laboratory |
| PAFC | Phosforic Acid Fuel Cell |
| PEMFC | Proton Exchange Membrane |
| PEMFC | Polymer Electrolyte Membrane |
| RANS | Reynolds Averaged Navier-Stokes |
| SAE | Society of Automotive Engineers |
| SMR | Steam Methane Reformation |
| SOFC | Solide Oxide Fuel Cell |
| SST | Shear Stress Transport |
| UTES | Underground Thermal Energy Systems |

# List of symbols

| Symbol | Definition | Unit |
|---|---|---|
| $A$ | Area | $[m^2]$ |
| $a$ | Speed of sound | $[\frac{m}{s}]$ |
| $b$ | Blade height | $[m]$ |
| $C$ | Chord length | $[m]$ |
| $C_p$ | Specific heat for constant pressure | $[\frac{J}{kg \cdot K}]$ |
| $D$ | Diameter | $[m]$ |
| $D_s$ | Specific diameter | $[-]$ |
| $ER$ | Expansion ratio | $[-]$ |
| $H$ | Enthalpy | $[J]$ |
| $h$ | Specific enthalpy | $[\frac{J}{kg}]$ |
| $I$ | Rothalpy | $[J]$ |
| $L_a$ | Axial length | $[m]$ |
| $M$ | Mach number | $[-]$ |
| $\dot{m}$ | Mass flow rate | $[\frac{kg}{s}]$ |
| $m$ | Mass | $[kg]$ |
| $N$ | Rotor speed | $[\frac{rev}{s}]$ |
| $N_b$ | Number of blades | $[-]$ |
| $N_s$ | Specific speed | $[-]$ |
| $P$ | Power | $[W]$ |
| $p$ | Pressure | $[Pa]$ |
| $PR$ | Pressure ratio | $[-]$ |
| $R$ | Gas constant | $[\frac{J}{kg \cdot K}]$ |
| $Re$ | Reynolds number | $[-]$ |
| $S$ | Blade pitch | $[m]$ |
| $T$ | Temperature | $[K][^\circ C]$ |
| $t$ | Time | $[s]$ |
| $t$ | Blade thickness | $[m]$ |
| $u$ | Tip speed | $[\frac{m}{s}]$ |
| $\dot{V}$ | Volumetric flow rate | $[\frac{m^3}{s}]$ |
| $V$ | Volume | $[m^3]$ |
| $v$ | Absolute velocity | $[\frac{m}{s}]$ |
| $W$ | Work | $[J][Wh]$ |
| $w$ | Relative velocity | $[\frac{m}{s}]$ |
| $w$ | Specific work | $[\frac{J}{kg}]$ |
| $Z$ | Compressibility factor | $[-]$ |
| $\alpha$ | Absolute flow angle | $[^\circ]$ |
| $\beta$ | Relative flow angle | $[^\circ]$ |
| $\gamma$ | Heat capacity ratio | [-] |
| $\Delta$ | Difference | [-] |
| $\eta$ | Efficiency | [-] |
| $\mu_{JT}$ | Joule Thomson coefficient | $[\frac{K}{Pa}]$ |
| $\rho$ | Density | $[\frac{kg}{m^3}]$ |
| $\Phi$ | Flow coefficient | $[-]$ |
| $\Psi$ | Work coefficient | $[-]$ |
| $\omega$ | Rotational speed | $[\frac{rev}{s}][\frac{rev}{min}]$ |

# 1 Introduction

In the scope of global decarbonisation, hydrogen has been identified as an essential energy carrier. Not only as an energy storage solution for further electrification in vehicles but also as a primary fuel source in processes that rely on chemical energy and cannot be easily electrified. However, the processes of generating hydrogen and extracting useful energy from it do come at an inherent energetic loss, leading to an even bigger emphasis on the need for more efficient processes and infrastructure.

One of the key benefits of using hydrogen as an energy carrier, as opposed to pure electrification, is the fact that it can be stored and transported relatively easily without the need for larger battery installations and high-voltage infrastructure. However, at ambient conditions, hydrogen is still a very sparse gas with a low energy density. This requires it to be compressed to high pressures, typically 35 or 70 MPa, for it to be useful for most storage and transport solutions. However, this compression is also a rather energy-intensive step, and the potential energy that is then stored in the compressed hydrogen is practically always lost when the gas is eventually expanded for its end use. This presents an opportunity to investigate if and how some of the potential energy could be recovered, which is the focus of this thesis.

Concretely, this thesis focuses on the conceptual design and performance analysis of an expander system aimed at recovering the potential energy stored in compressed hydrogen.

In order to tackle this challenge as well as possible, the research started with a literature study exploring the most important actors in the hydrogen value chain in order to be able to present a solution in an application where its impact would be the most beneficial. This literature study on hydrogen storage, distribution and power systems is presented in Chapter 2.

This is followed by Chapter 3 in which the physical properties and models of hydrogen are explored. This led to the first assessment of several proposed hydrogen systems in which potential energy could be recovered. Leading to the the selection of hydrogen refuelling stations as the preferred operating system for this research.

Next, Chapter 4 delves into the details of how hydrogen refuelling stations operate and which different types exist. This is followed by the previous work that has been performed on the topic of recovering potential energy from compressed hydrogen in hydrogen refuelling stations and, finally, the development of a system model that is able to replicate a typical refuelling cycle in such a station, adapted to the needs of this thesis.

Chapter 5 goes into depth on the sizing and design of a turbine expander for this application and presents how its performance is modelled in the 1D system model and validated in a 3D CFD simulation.

The results of this work are laid out in Chapter 6 where the reader is first presented with a summary of all the input parameters and assumptions to the system model in Section 6.1, followed by the results of the overall refuelling process itself in Section 6.2. Next, the performance of the turbine in the 1D model and in the 3D validation case are presented in Section 6.3 and Section 6.4 respectively. As these are inherently very different models with different assumptions, Section 6.5 is dedicated to exploring the differences between the results of both of these models. Next, the overall impact of employing a turbo-expander in a hydrogen refuelling station is presented in Section 6.6. This is addressed from multiple points of view. On one hand, the effect of employing a turbo-expander, as opposed to a traditional expander valve, in a refuelling

station is covered, but also the energy recovery from the expander, the additional energy savings in other parts of the systems are treated as well as an economic assessment. Finally, Section 6.7 presents a sensitivity analysis on some of the design parameters and assumptions to explore in which direction the proposed design can be further improved in future work.

Finally, a set of concrete conclusions and recommendations for future work are presented in Chapter 7

# 2 Hydrogen storage, distribution and power systems

Hydrogen is often stated as a part of the future of sustainable energy systems. For this thesis, the general relevance of hydrogen as an energy carrier is considered a given and will not be dealt with in detail. However, in order to cover the various systems in which hydrogen is used and where energy could potentially be recovered from in a structured manner, Section 2.1 will provide a general introduction to and overview of the so-called hydrogen value chain. The following sections, 2.2 through 2.5, will each go into detail about a specific part of this hydrogen value chain, exploring the current applications and developments specific to that part and identifying applications that could be of interest to recover potential energy from.

## 2.1 Introduction to the hydrogen value chain

The hydrogen value chain is a concept that can be described as a series of connected stages in the process of producing, transporting, distributing, storing, and utilising hydrogen. It is a concept that specifically details all these stages from an industrial perspective as opposed to the more popularised term, "the hydrogen economy", which focuses on the macro-economical aspects of utilising hydrogen as a main energy carrier instead of fossil fuels.

In essence, the hydrogen value chain is an umbrella name that provides a general overview of the industries, technologies, processes and stakeholders involvde but which also covers the connections and dependencies between them.

In general, the production category covers all methods and upstream processes of producing hydrogen; this is further covered in Section 2.2. The transportation category relates to everything around transporting hydrogen from point A to point B. Specifically on the infrastructure and logistics side, such as large pipelines, trucks and ships. It is closely related to what would be called distribution, but the difference assumed in this work is that the term distribution refers more to connecting the end users to the system, whereas transportation is used to describe connections with much higher throughout and over larger distances. But there definitely is some overlap, and the two will be jointly detailed in Section 2.3. Storage refers to every method of storing volumes of hydrogen for it to be used later, and utilisation refers to all possible end uses. This could refer to generating power and heat or to the use of hydrogen as a base chemical. These will be further elaborated on in sections 2.4 and 2.5, respectively.

## 2.2 Hydrogen generation

Although atomic hydrogen $H$ is by far the most common element in the universe, it is often found as a part of other molecules and only rarely in its pure molecular form $H_2$. For human activities, this results in the need to generate molecular hydrogen ourselves. A popular method to distinguish between different generation methods and sources of hydrogen is to define them by color[1]. This is a popular depiction as it takes into account both the method and the origin of the energy used to generate hydrogen, which is an important aspect to take into consideration

[1]Please note that these colours are only a reference to the origin source and method of generation and do not represent the physical colour of hydrogen. In its pure form, hydrogen is a completely transparent and odourless gas.

when aiming to use hydrogen as a sustainable energy carrier.

At the time of writing the most elaborate distinction between different types of hydrogen includes 12 different colours as visualised in Figure 2.1 but the most commonly referred to are green, blue, black and grey hydrogen.

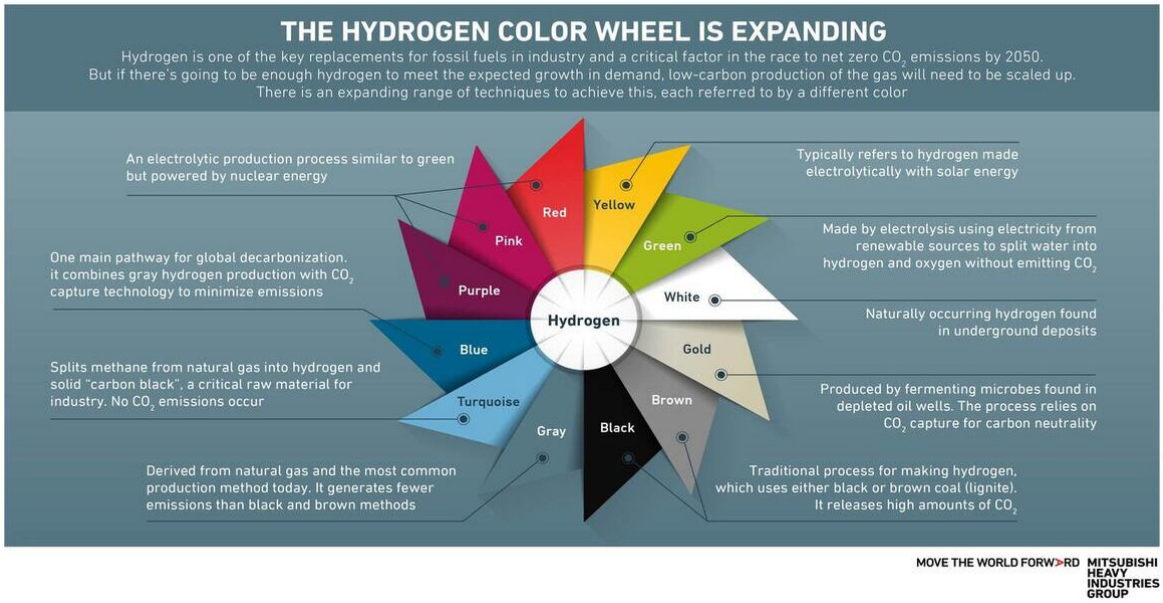


*Figure 2.1: Extensive overview of the different "colours" of hydrogen [1].*

As it currently stands, brown, black and grey hydrogen stemming from Steam Methane Reformation (SMR) or coal gasification are by far the most common methods of generating hydrogen, making up around 96% of global hydrogen production [2]. Unfortunately, these are inherently polluting processes that release 2.5 - 3 carbon molecules per molecule of hydrogen. Ater that, the next most common method of generating hydrogen is electrolysis which has the potential to be completely carbon neutral if combined with sustainable electricity. Other methods, such as organic processes with bacteria or through nuclear reactions, are far less common and will not be further analysed due to their relatively low share.

The general production of hydrogen from carbon molecules and electrolysis will each be covered in more detail in the following subsections: Subsection 2.2.1 and Subsection 2.2.2. Lastly, Subsection 2.2.3 covers the process of liquefying hydrogen. Although not technically a method of generating hydrogen, it does typically come upstream of transport and distribution and is therefore covered in this section.

### 2.2.1 Hydrogen production from carbon molecules

In general, each of these processes involves the heating of a source of carbon molecules and combining it with steam at high temperatures in order to split the molecules and form different combinations that result in molecular hydrogen and a different carbon molecule.

Steam methane reforming, for example, breaks down methane $CH_4$ (Stemming from higher hydrocarbons which have been pre-reforming in a different process) and water $H_2O$ in molecular hydrogen $H_2$ and Carbon dioxide $CO_2$ following Equation 2.1 [3, 4].

$$CH_4 + 2H_2O \rightleftharpoons CO_2 + 4H_2 \tag{2.1}$$

Similarly, coal gasification involves the blowing of oxygen and steam at high temperatures through coal resulting in an oxidation process which primarily leads to a gaseous combination of water vapour $H_2O$, molecular hydrogen $H_2$, carbon monoxide $CO$ and carbon dioxide $CO_2$. Although other by-products can also be produced. The end product is typically syn-gas, a combination of hydrogen and carbon monoxide from which hydrogen can again be extracted. The overall process to syngas is shown in Equation 2.2.

$$3C + O_2 + H_2O \rightleftharpoons H_2 + 3CO \tag{2.2}$$

Although both of these processes involve high temperatures and possibly high pressures in the reactor itself (20 - 30 bar for SMR), they also require further processing to result in pure hydrogen. Resulting in an end product that is not at particularly high pressure and thus requires further compression for most downstream applications.

### 2.2.2 Electrolysis

Electrolysis refers to a process in which a non-spontaneous chemical reaction occurs by passing a current through the media. In the context of hydrogen production, it specifically refers to the splitting of water molecules $H_2O$ in molecular hydrogen $H_2$ and oxygen $O_2$. Equation 2.3 provides an example of the process occurring in a Polymer Electrolyte Membrane (PEM) electrolyser, which typically operates at low temperatures (70 - 90°C) and pressures, but various other types exist, such as Alkaline Electrolysers which make use of a liquid alkaline solution as an electrolyte instead of a membrane and Solid Oxide Electrolysers which operate at much higher temperatures (700 - 800°C) [5].

As they are very reliant on the supply of electricity, the environmental sustainability of producing hydrogen with electrolysers is dependent on the source of electricity supplied to the system, but different from other hydrogen production methods, the electrolysis process does not inherently include carbon molecules.

$$2H_2O \rightleftharpoons O_2 + 2H_2 \tag{2.3}$$

### 2.2.3 Hydrogen Liquefaction

As a liquid, at atmospheric pressure and a temperature of 20 K, hydrogen has a density of 71.28 $kg/m^3$, roughly 800 times higher than that of gaseous hydrogen at atmospheric pressure and 1.79 times higher than gaseous hydrogen at 700 bar - both at 293 K or 20°C [6]. Based on this, it holds significant promise for transporting large quantities of hydrogen in an effective way. However, as the boiling point of hydrogen at atmospheric pressure is -253°C, it also requires significant infrastructure to liquefy hydrogen. Although there are many variations on specific installations, the general process of cooling a gas to such low temperatures is based on the Claude cycles, visualised in Figure 2.2 [7].

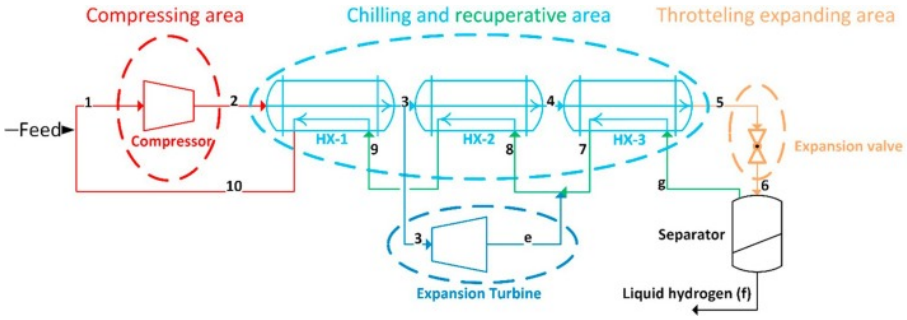


*Figure 2.2: Conceptual design of the simple universal Claude cycle [7].*

As the gas enters the system, it first gets compressed and passes through a series of heat exchangers where it is cooled in heat exchangers through interaction with other media such as liquid nitrogen, helium or oxygen. In the second step, part of the flow passes through a turbo-expander, lowering the pressure and significantly reducing the temperature through the expansion process. Next, there might be another interaction through a heat exchanger, after which the cold gas passes through an expansion valve. Expanding the gas to such low pressures that part of it liquefies. The remaining gas is reused as a coolant in the heat exchanger cycles and compressed to flow back through the system. Specific systems differ in terms of how many heat exchangers there are, which coolants they use, how much of the flow passes through the turbo-expander and the system's operating pressures [7, 8]. Figure 2.3 provides an example of how the basic Claude cycle can be appended to include more elaborate cooling processes with different media acting in it. In fact, the majority of research in the past 20 years on the topic of hydrogen liquefaction has been about these hybrid and pre-cooled systems [8].

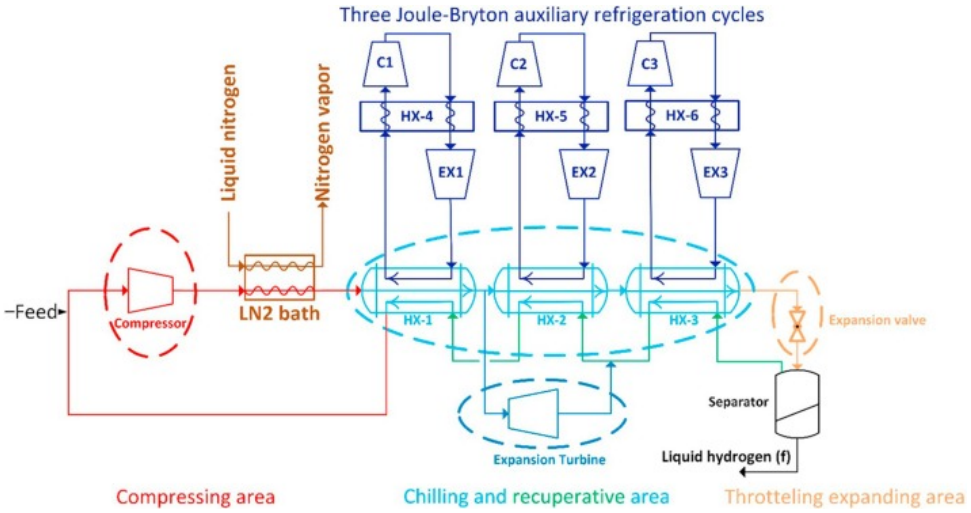


*Figure 2.3: Conceptual design of the liquid-nitrogen and Joule-Bryton pre-cooled Claude cycle [7].*

Installations of various sizes do exist, ranging from laboratory set-ups to full-scale industrial plants [7, 8]. Opposed to the Linde cycle, which only uses a throttling process, the Claude cycle, which uses a turboexpander, has been shown to improve the efficiency of a system as it holds the potential to reduce the energy costs involved in the cooling cycles significantly [8]. It has even been suggested that the expansion valve could be replaced with a turboexpander to further increase the efficiency of such a cycle, but no publications of real-world implementations of this have been found in the literature. To the author's understanding, presumably because

of the deteriorating effects of phase change and condensation in the expansion process on the turboexpander blades themselves.

## 2.3 Hydrogen transport and distribution systems

Another challenge of a sustainable future is the transportation and distribution of energy. Although most of the world indeed has a well-developed power grid for transporting electricity, it is primarily designed in a one-directional way. It is designed to transport electricity from a power plant to an end user but generally does not cope well with distributed generation through solar panels or wind turbines [9]. Apart from that, the losses of transporting electricity over large distances are significant as well [10]. The following section will elaborate on possible hydrogen transport and distribution systems.

### 2.3.1 Energy transport through hydrogen: Why?

Aside from scaling problems of the electricity grid, 55.9% of our current energy supply or 101,545 TWh of energy comes from natural gas and oil, mainly transported by ships or pipelines in liquid or gaseous forms [11]. Opposed to the current 27,812 TWh of electricity produced - of which 1,398 TWh is already being generated from oil and gas. Converting all of the energy stemming from oil and gas to electricity and transporting it as such would require a fourfold increase of the global capacity of the current electricity infrastructure and a 72-fold increase of conversion capacity in the form of power plants. It is almost ambiguous to state that replacing all of this oil and gas energy with sustainable sources and transporting it purely as electricity is not the most realistic scenario. Even when taking distributed generation and smart grids into account.

Alternatively, energy can also be transported in the form of hydrogen or associated hydrogen-based products. In fact, a large part of the current knowledge about gas transportation translates very well to using hydrogen gas, and existing gas infrastructure can be repurposed for the use of hydrogen or a hydrogen-natural gas mix [12, 13]. Indeed, on a €/MWh/km basis, transporting energy as hydrogen through pipelines can become significantly cheaper than transporting it as electricity and needing to expand the electrical grid [10]. Without taking into account conversion losses up to 1/8th when considering new gas infrastructure as opposed to new HV-DC lines [10, 14]. Even taking ±75 % conversion losses from electrolysis into account [15] and a gas turbine efficiency of ±40 % [16] or a fuel cell efficiency of 50-60 % [17, 18] this amounts to a lower cost per unit of energy per unit of distance.

Furthermore, using hydrogen or hydrogen-based products also allows for energy distribution between continents or reaching regions lacking infrastructure by transporting energy in a gaseous or liquid form via ship, road or railway tankers [19, 20]. Details of storing hydrogen in liquid or gaseous forms in tanks will be further covered in Section 2.4.

From this, it can be concluded that also for energy transportation hydrogen holds significant promise as an energy carrier. This includes pipeline infrastructure, electrolysis, re-electrification, refuelling and liquefaction plants, as well as LH2 terminals, tankers and connection ports for any other industrial applications.

### 2.3.2 Energy transport through hydrogen: How?

As presented, transporting energy with hydrogen is a viable energy transport method, but several actors are involved in transporting large volumes of hydrogen. The 3 main modes of

transporting hydrogen - via fuel trucks/trailers, via pipeline infrastructure or via tanker ships - are discussed. A lot of similarities can be drawn between the distribution of natural gas.

#### 2.3.2.1 Tube-trailers

The first mode of transporting hydrogen as a gas or as a liquid is through tube-trailers. These are essentially trailers with pressure vessels or a liquid hydrogen tank attached to them transported via road or railways. Typically used to supply hydrogen to locations that are either remote or lacking existing pipeline infrastructure. Naturally, this mode of transport is limited in capacity as only a certain amount of hydrogen physically fits on a single trailer. However, it has a high flexibility regarding where hydrogen can be supplied. The capacity of these trailers is highly dependent on the working pressure of the tanks on board. For gaseous hydrogen, common applications vary between 250 and 500 bar and can provide a capacity of up to 1,100 kg of hydrogen [21]. As of February 2023, the highest capacity trailer that was found in reference literature is limited to 517 bar and can transport up to 1,300 kg of hydrogen [22]. European-funded projects currently aim to develop new systems and regulations to allow for the transport of higher pressure tanks and increase this capacity above 1,500 kg at 700 bar. [23]. Transporting liquid hydrogen via trailers can provide higher capacities - up to 3,500 kg - due to its higher density and larger tank sizes but are limited in range due to the boil-off of the liquefied hydrogen [21].

#### 2.3.2.2 Pipelines

A second mode of transport is through pipelines. This allows for large amounts of hydrogen gas to be transported over large distances. Over 4,500 km of developed hydrogen pipeline networks already exist, predominantly in Europe and Northern America (as of 2016) [23]. However, studies on the development of a hydrogen backbone for Europe expect that it is possible for this to increase to 53,000 km by 2040 [24]. This also assumes that part of the existing natural gas pipelines will be retrofitted to transport hydrogen gas instead. The Dutch gas infrastructure operator Gasunie aims to repurpose up to 85% of the currently existing natural gas pipelines for hydrogen, made possible by an expected decrease in natural gas consumption [25]. However, hydrogen pipelines that are currently in existence are mainly used for industrial processes and not yet for large end-user consumption. As similarities can be drawn with natural gas pipelines, it should be noted that pressure levels highly change per country and are not always constant. The US-based HyLine operates around 1000 bar, whereas most natural gas pipelines operate at 13-100 bar [26]. The Europe-based Hydrogen Backbone is expected to have various pressure regimes, 10-20 bar and 30-50 bar [27].

#### 2.3.2.3 LH2 tankers

The third main mode of transporting hydrogen is via liquid hydrogen (LH2) tanker ships. This has the potential to transport large amounts of hydrogen between continents or islands where no existing pipelines or power lines are currently reaching. From an operational aspect, this is again very similar to LNG terminals, which are already commonplace. As of early 2022, the project HySTRA has been piloting a ship, the Suiso Frontier, to transport 87.5 tonnes of liquid hydrogen between Hastings, Australia and Kobe, Japan [28, 29]. Other studies from the Kawasaki Heavy Industries Group have also detailed plans for a larger vessel capable of transporting up to 160,000 $m^3$ or roughly 11,200 tonnes of hydrogen on the same route [30].

Although currently not yet in existence it holds a lot of potential for transporting large amounts of energy on par with the potential of LNG. Especially enabling the transport between regions with a lot of renewable energy potential and regions with less natural energy resources.

### 2.3.3 Hydrogen distribution to end users.

As described in Section 2.1, the distinction that is made between transport and distribution of hydrogen is that hydrogen distribution refers directly to connecting end users to a larger grid, whereas transport refers to systematically transporting large volumes of hydrogen over greater distances.

In order to properly describe the different relevant methods of hydrogen distribution, it makes the most sense to link this to descriptions of the end user. Generally, these can be considered to fall under one of three categories which will be shortly described in the following parts.

#### 2.3.3.1 Industrial users

Depending on their size, industrial users are typically centred around industrial parks and can benefit from larger infrastructure investments such as supply via dedicated pipelines. It is also not uncommon to see large storage tanks nearby, which get periodically refuelled via delivery trucks, either of which have already been mentioned in Subsection 2.3.2.

#### 2.3.3.2 Residential and building users

Residential and building users are quite often already connected to a pre-existing natural gas grid which can potentially be repurposed for the use of hydrogen or a hydrogen - natural gas fuel blend if such change is made on a large enough scale. Alternatively, individual storage tanks can also be installed and periodically refuelled, similar to heating oil in the past. It is also important to note that each of these would need to be paired with separate installations such as hydrogen central heating systems or stationary fuel cell systems for heat or electricity generation.

#### 2.3.3.3 Mobility sector

Finally, the mobility sector covers the perhaps most well-known use of hydrogen: as a fuel for hydrogen cars, busses, trains, trucks and aircraft. In this case, the final distribution node essentially refers to "how to get hydrogen in a vehicle tank". This is commonly done via gaseous hydrogen refuelling stations (HRS), which, depending on location and size, receive hydrogen via pipelines or supply trucks, store it in one or several buffer tanks at higher pressures and then expand and cool it during a refuelling process after which the hydrogen is deposited in the vehicle tank. A basic overview of such a hydrogen refuelling station can be seen in Figure 2.4

Alternatively, liquid hydrogen can also be used. This either gets supplied or liquefied on site, after which it gets deposited into the vehicle tank via liquid hydrogen refuelling stations, but the real-life applications of this are far less common than those of gaseous hydrogen.

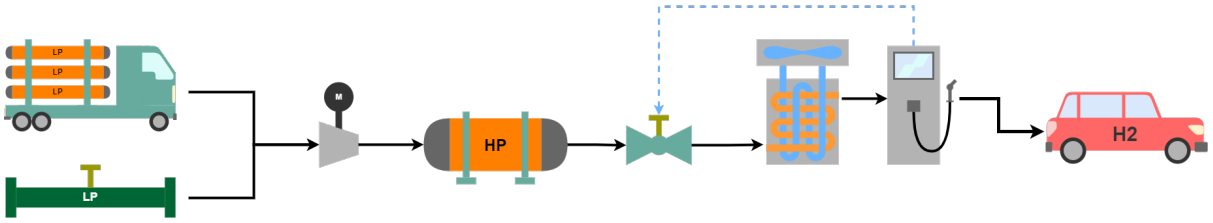


*Figure 2.4: Schematic configuration of a hydrogen refuelling system (HRS), adapted from Chen et al.[31].*

## 2.4 Hydrogen storage

With the ever-increasing need for and supply of renewable energy also comes a large challenge of matching supply and demand in all conditions [32]. Current electrical infrastructure systems are not always capable of dealing with these requirements. The lack of adequate energy storage systems in the world's energy grid results in a lot of non-utilised energy. Being able to store renewable energy when it is in high supply and use it when it is in high demand is therefore critical [32]. There are several different methods of storing energy on such large scales, including storing it in the form of hydrogen. To present the relevance of hydrogen as a carrier for energy storage, the main energy storage methods will be briefly described in Subsection 2.4.1. After having presented the relevance of hydrogen as a medium for energy storage, the most relevant storage methods of hydrogen will be further explored in Subsection 2.4.2.

### 2.4.1 Energy storage

There are several different methods of storing energy on large scales. These can be broadly categorised under the following categories with some examples:

- Electrical storage in (Ultra) capacitors
- Electrochemical storage in (Flow) batteries
- Chemical storage in synthetic fuels, hydrogen, ammonia or other Liquid Organic Hydrogen Carriers (LOHCs)
- Mechanical storage as a pressurised gas, pumped hydro technology or flywheels
- Thermal energy in Underground Thermal Energy Systems (UTES), Heat Transfer Fluids (HTF), underground rock beds, molten salt or metal systems or steam accumulators in tanks and underground caverns.

Each of these has its own relevance depending on the energy storage needs, availability of resources and even geological features. Capacitors and flywheels are, for example, very efficient and excellent for very short-term storage, such as grid balancing and offsets between peak energy demand and variable energy supplies from wind and solar in the timescale of minutes to hours. Batteries and thermal systems based on, for example, molten salt or molten aluminium are then again more relevant for storing energy on the timescale of hours to days as, inevitably, the state of charge and temperature drop. On the upside, each of these typically has relatively low conversion losses. Opposed to storing energy in chemicals at ambient temperatures such as ammonia, hydrogen, synthetic fuels or other LOHCs for which the conversion losses are significant. But these can be applied on a much broader range of timescales, up to weeks or

months, are relatively scalable, and the chemical carriers are typically much more transportable. In order to store large capacities of energy for even longer periods of time, one could consider underground thermal storage, pressurised gas storage in caverns and pumped hydro. These are more suitable to store energy for very long periods of time to, for example, cover seasonal differences and typically have very large capacities. But they are also bound to geographic features and less flexible to implement.

As can be deduced, chemical energy carriers are very broadly applicable, and in this context of sustainable, fossil-free, climate-neutral chemical energy carriers, hydrogen is a very powerful element. It can be used on its own as a storage medium and as a base for other modes of storage in the form of ammonia, synthetic fuels and other LOHCs. Each of these can be implemented very flexibly in terms of the storage duration, capacity and location. Furthermore, these gasses or liquids can be transported relatively easily and serve many applications. Moreover, hydrogen itself can also be used as a driving gas for pressurised gas storage in tanks or salt caverns.

### 2.4.2 Hydrogen storage solutions

Having established the relevance of hydrogen as a suitable energy carrier to both transport and store large amounts of energy the question arrives: How does one store hydrogen itself? The following subsection will cover the three major methods for storing hydrogen: high-pressure tanks for gaseous hydrogen, liquid hydrogen tanks and storage in salt caverns.

#### 2.4.2.1 High pressure tanks

High-pressure hydrogen tanks, or simply hydrogen tanks, are the most common form of storing hydrogen in its gaseous form, especially for mobile applications. These vessels are generally constructed out of filament-wound carbon fibre tanks with a non-permeable inner liner. These vessels can be classified under one of five different types, depending on the materials used for the liner and potential reinforcements thereof.

The large benefit of these vessels is their flexibility in implementing them. Diameter and length can relatively easily be designed to fit a desired design. Active work is being done on lightweighting, the design of conformal, non-cylindrical hydrogen tanks, and the integration of these tanks as structural elements in vehicles.

As mentioned, these are typically high-pressure tanks; this is to increase the volumetric density of hydrogen so that a suitable amount of hydrogen can be stored in a reasonable space. Currently, there are two main standards in terms of pressure levels for mobile applications, either up to 350 bar or up to 700 bar. The lower 350 bar standard still gets used in applications where size or capacity are less of a concern and costs are a more important consideration, such as in public transport vehicles like buses and trains. In recent years the 700 bar standard has become more prevalent as material science and production methods have progressed, and it has become clear that the increased capacity outweighs the added complexity and system weight. In other applications outside of the transport sector, other standards do exist.

High-pressure vessels typically get used to store hydrogen in small amounts, in the order of 1 to 10 kilograms and typically for relatively short amounts of time in the order of days to weeks as also these tanks are susceptible to some permeation and leakage.

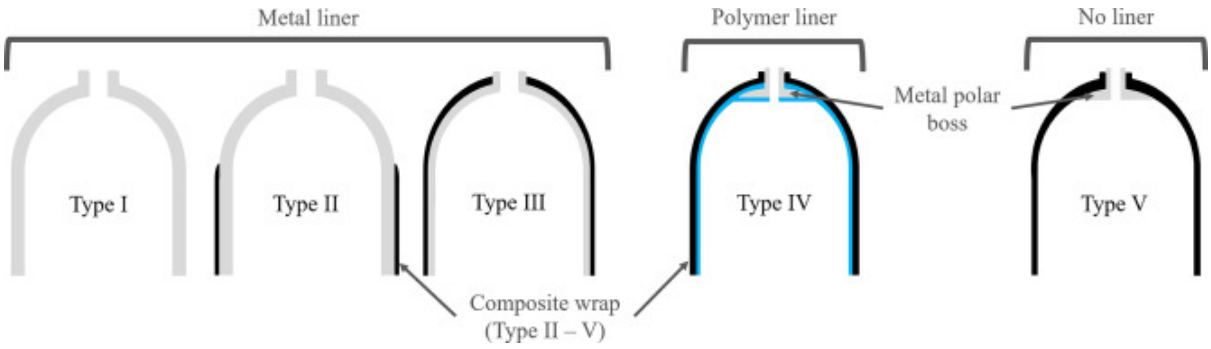


*Figure 2.5: A visualisation of different categories of high-pressure hydrogen tanks [33].*

#### 2.4.2.2 Liquid hydrogen tanks

Liquid hydrogen tanks store hydrogen in its liquid form. Due to the required low temperatures, 20.5 K, these need to be super-insulated, commonly achieved with a vacuum layer. The benefit of storing hydrogen in its liquid form is its density, allowing a lot more hydrogen to be stored in the same volume and without the safety risks involved in high-pressure tanks. Its downsides are the availability of liquid hydrogen in the supply chain, the energy required to liquefy it and the system complexity of a vessel able to maintain hydrogen at such low temperatures for extended amounts of time without it evaporating [34].

#### 2.4.2.3 Salt cavern storage

Salt cavern storage makes use of existing geological features to store hydrogen underground. This allows for very large capacities in the order of multiple GWhs and for longer periods of time, weeks to months. The storage method specifically holds merit for long-term seasonal energy storage and buffering the grid during peak demand or peak production hours of solar and wind energy [35, 36, 37].

## 2.5 Hydrogen applications

Previous sections already covered hydrogen generation, transport, distribution and storage as aspects of the hydrogen value chain. But of course, this all exists to serve a final use of hydrogen. In general, all end applications of hydrogen can be categorised into four categories. Whether it is used to drive a mechanical system and essentially make something move, to generate electricity, to generate heat, or wether it is used as a base material for its chemical properties. The processes behind each of these are elaborated on below.

### 2.5.1 Mechanical power

The most direct method of converting the energy stored in hydrogen into mechanical energy is through combustion, typically in a gas turbine, but other endeavours have also researched using hydrogen as a fuel in reciprocating internal combustion engines. However, the use of these is, thus far, far less common. Technically, either of these combust hydrogen and use the subsequent thermal energy of the combusted fuel to drive a piston or turbine, resulting in mechanical energy, but it is considered as such because it all takes place in the same system.

In each of these applications, the shaft power can be used directly to propel an airplane, a ship, a truck, or a car, but these can also be used to generate electricity for the grid.

#### 2.5.1.1 Gas turbines

Gas turbines in the energy supply sector are typically used to work as backup generators around intermittent power supply and demand, S off-grid energy solutions or as engines in aviation [38]. Depending on the application, several types of fuel can be used, but these are mostly polluting fossil fuels. However, industry-leading gas turbine manufacturers such as GE [39, 40, 41], Siemens [42], Kawasaki [43] and others[44, 45] are developing and deploying gas turbines fueled partially or completely by hydrogen. Next to the industry, research projects have also been looking into hydrogen as a substitute or secondary fuel in these applications [38, 46, 47, 48]. however, it should be noted that the combustion of hydrogen does still result in harmful $NO_x$ emissions and is therefore not completely "clean", even if the hydrogen is produced from a renewable energy source.

#### 2.5.1.2 Reciprocating internal combustion engines

As a combustible gas, hydrogen can also be used in reciprocating ICEs; a large advocate argument for this application is the familiarity with and widespread use of this ICE technology, especially in the mobility sector. It is however still plagued by the same issues as gas turbines, namely $NO_x$ emissions, hydrogen embrittlement and leakages which make it hard to implement on a large scale in the aforementioned transport sector due to cost and weight limitations [49, 50]. Select automotive manufacturers such as BMW [51] and Toyota [52] have worked on hydrogen-fueled ICEs, but to date, no such vehicle is available on the consumer market. However, in the maritime sector, MAN is developing 4-stroke reciprocating engines that would be able to run on a fuel blend of diesel and hydrogen [53].

### 2.5.2 Electrical power

If one wants to convert the energy stored in hydrogen directly into electrical energy this can be done through fuel cells. A fuel cell is a device where chemical energy is transformed into electrical energy and heat as long as its electrodes are supplied with the relevant reactants [18]. The membrane between the two supply channels typically allows for proton and neutron elements to pass through but not the electrons of the fuel used. The electrons are instead routed through an electrical circuit, effectively creating a current flow [18]. Various types of fuel cells exist, each based on different types of fuels and operating conditions. A non-exhaustive overview of these is provided in Table 2.1. However, perhaps the most well-known is the PEM (Proton Exchange Membrane or Polymer Electrolyte Membrane) fuel cell, represented in Figure 2.6. A low-temperature fuel cell that uses hydrogen and oxygen as fuel and, in doing so, does not emit harmful emissions. Major reasons for the "popularity" of PEM fuel cells are indeed the low operating temperatures, the emissions-free process, the use of non-toxic fuels - as opposed to ammonia fuel cells - and the relatively high efficiency of up to 60%. However, they do suffer from some drawbacks such as the need for platinum as a catalyst, the material properties of the membranes, requiring significant cooling, 40-60%, and the power density and cost per kW of the fuel cell itself compared to combustion engines or generators.

| Fuel cell type | Anode reactant | Active ion | Cathode reactant | Operating temp. [°C] | Efficiency [%] |
|---|---|---|---|---|---|
| Proton exchange membrane (PEMFC) | $H_2$ | $H^+$ | $O_2$ | 30-100 | 40-60 |
| Direct Methanol (DMFC) | $CH_3OH + H_2O$ | $H^+$ | $O_2$ | 20-90 | 20-50 |
| Phosforic Acid (PAFC) | $H_2$ | $H^+$ | $O_2$ | ~200 | 40-50 |
| Alkaline (AFC) | $H_2$ | $OH^-$ | $O_2$ | 50-200 | 50-60 |
| Molten Carbonate (MCFC) | $H_2$ | $CO_3^{2-}$ | $O_2 + CO_2$ | ~650 | >60 |
| Solid Oxide (SOFC) | $H_2$ | $O^{2-}$ | $O_2$ | 500-1000 | 50-60 |

*Table 2.1: Principle operation characteristics and properties of the most common fuel cell types [18].*

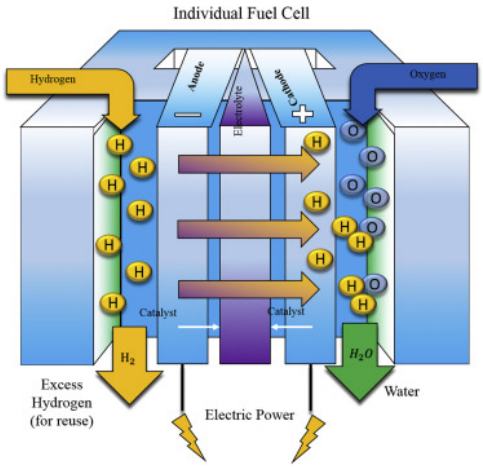


*Figure 2.6: Principle sketch of a PEM fuel cell [18].*

#### 2.5.2.1 Stationary power supply

One of the benefits of fuel cell systems is that they do not need to be connected to a grid system. Indeed, they require a fuel supply which can happen through a pipeline infrastructure, but this can also be provided through fuel tanks. This makes it an attractive solution for sustainable power supply solutions that are either temporary, in remote locations or as a source of back-power. Practical examples of temporary installations are energy installations at large events, construction works and emergency situations where grid access is non-trivial, but other applications also include backup power in data centres, hospitals and industry [54, 55, 56, 57, 58].

#### 2.5.2.2 Mobile applications

Next to the stationary applications, fuel cells can also be implemented in mobile applications. Various applications like cars, buses, transport trucks and trains already exist, and others, like

airplanes are currently under development. In fact, already six car brands, Toyota, Hyundai, Honda and Opel, Citroën and Peugeot under the Stellantis group have hydrogen cars on the market[59] and Hyundai, Daimler, Daf-VDL, MAN and Scania have hydrogen trucks available [60]. Examples of hydrogen buses in operation have been present all over the world for several decades, ranging from pilot projects in the '90s to full-scale operation in more recent years[61] and several train lines operating on hydrogen exist in Germany and China [62, 63]. Various development programs for the use of fuel cells in aviation applications are also happening by student teams, universities and aircraft manufacturers [64, 65, 66, 67, 68, 69, 70, 71]. By 2030 it is expected that 1 in every 12 cars sold in Germany, Japan and South Korea will be powered by Hydrogen and that there will be a fleet of more than 350,000 hydrogen trucks for freight transport [72].

In general, for mobile fuel cell applications, the consensus appears to be that it is especially relevant for applications that require continuous operation and a large range without significant weight penalties. A prime example of this is freight transport by truck [73]. Smaller vehicles, such as small city cars, benefit less from the perks of a fuel cell system than just a battery system due to the increased system complexity. Exempted to this might be demographics in which large-scale electrification is not feasible but where gas infrastructure already exists; an example is the Indian automotive market [74].

### 2.5.3 Thermal power

Another application would be any other process in which fossil fuels get burned to achieve high temperatures without the desire to convert to mechanical or electrical energy. This is relevant for a large part of the heavy industry, accounting for up to 20% of global greenhouse gas emissions. Specifically, cement factories and steel furnaces prove interesting for decarbonisation via hydrogen [75]. The cement industry contributes up to 8% of the global CO2 emissions, 40% of which comes directly from the combustion of fossil fuels [76, 77, 78]. In the steel industry (which also contributes to 8-9% of global CO2 emissions) up to 20% of carbon emissions can be saved by substituting hydrogen as a fuel in combustion processes [79, 80, 81].

### 2.5.4 Hydrogen as a base material

Apart from using hydrogen as a fuel or as a means of transporting energy, it can also be used for its chemical properties. In the steel industry, hydrogen can be used as a reduction agent to turn various forms of iron oxide in pure iron and water as a byproduct; see equations 2.4 through 2.6 [82]. Furthermore, hydrogen can also be used to produce ammonia. Aside from storing, transporting or consuming hydrogen in fuel cells, ammonia can also be used directly in fertilisers [83].

$$Fe_2O_3 + 3H_2 = 2Fe + 3H_2O \tag{2.4}$$

$$Fe_3O_4 + H_2 = 3FeO + H_2O \tag{2.5}$$

$$FeO + H_2 = Fe + H_2O \tag{2.6}$$

# 3 Recovery of potential energy stored in compressed hydrogen

This chapter will first provide an explanation of the physical processes that occur when expanding idealised and real gasses in Section 3.1. Next, the thermodynamical properties and specifics of expanding hydrogen will be covered in Section 3.2. This is followed by Section 3.3 in which each step in the hydrogen value chain from generation until end application will be analysed for its potential of serving as an application in which potential energy can be recovered from compressed hydrogen. The final trade-off is presented in Section 3.4 and lastly, the most promising application, hydrogen refuelling stations, will be elaborated upon in Chapter 4.

## 3.1 Ideal and real gas models

In order to model the behaviour of a gas in a computational model or simulation is required to have a numerical representation of the gas and its behaviour. There are generally two methods of doing so, either one assumes the gas to behave as an ideal gas and accepts certain limitations to their model, or one aims to simulate real gas behaviour through a more complex set of equations and coefficients specific to that gas. The following two subsections will elaborate on each of these.

### 3.1.1 Ideal gas models

The ideal gas assumption is a simplifying way of representing the behaviour of gas through essentially a single equation, the ideal gas equation of state: Equation 3.1. In which $p$ represents the pressure, $V$ the volume of the gas, $n$ the number of moles of gas, $R$ the universal gas constant and $T$ the temperature of the gas.

$$pV = nRT \tag{3.1}$$

This equation represents the following assumptions about the physical behaviour of gas particles.

- Gas particles are point masses with a negligible volume
- There are no inter-molecular forces or interactions between the gas particles
- Any collisions between gas particles are perfectly elastic
- Any changes in the kinetic energy of the gas particles are only dependent on temperature

In essence, the ideal gas assumption, represented by Equation 3.1, provides a linear relation between the pressure, density and temperature of any gas which, for certain pressure and temperature ranges can be considered a close enough approximation of the real gasses behaviour.

### 3.1.2 Real gas models

In reality, a gas does not follow such a linear relation between pressure, temperature and density and a multitude of models exist to predict this more accurately. Popular examples include Van

der Waals, Peng-Robinson, Redlich-Kwong, and Betti-Bridgmann equations. Most of these rely on higher-order equations that include several coefficients with values specific to each gas. These models are often compared to experimental data from the National Institute of Standards and Technology (NIST) and their relative accuracy has already been extensively described in other research. Generally, a trend can be seen that some models are tailored to provide more accurate predictions for specific temperature and pressure regimes, whereas others provide a less accurate but more broadly applicable prediction.

Alternative to real gas models it is also possible to provide equations based on a data fit which can work for a specific gas in a specific range but would not be broadly applicable, or adaptations can be made to the ideal gas model by determining polynomial fits to the behaviour of specific heat constants. Figure 3.1 shows a comparison between several real gas models, a data fit, reference values from NIST and the results of the ideal gas model.

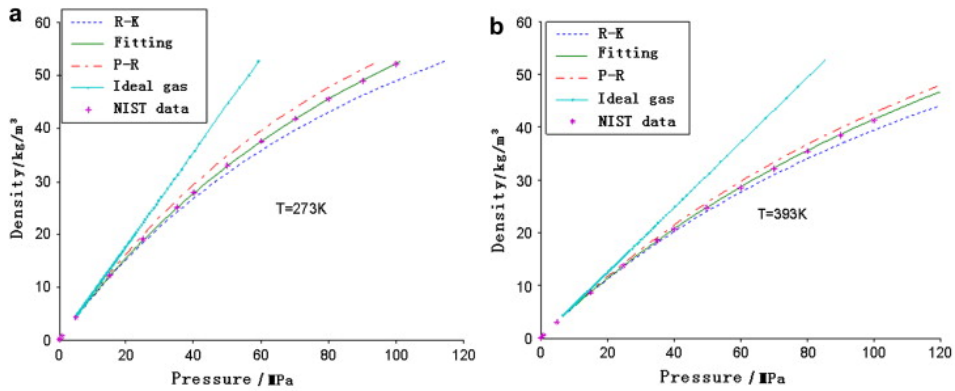


*Figure 3.1: Comparison of real-gas state equations of hydrogen, (a) T = 273 K, (b) T = 393 K [84].*

### 3.1.3 Compressibility factor

It should be noted that real gas calculations are computationally more expensive and therefore, a trade-off between using a real gas model or using the ideal gas assumption is always a good idea.

One method of doing this is through the comprehensibility factor, which is defined as the ratio between the specific molar volume of the real gas and the ideal gas at a certain pressure and temperature, as shown in Equation 3.2. If a gas were to have ideal behaviour, the value of the compressibility factor would be equal to 1.

$$Z = \frac{V_{real}}{V_{ideal}} \tag{3.2}$$

If the value of the compressibility factor is known for every pressure and temperature combination within the to-be-analysed range, Equation 3.3 can also be used as an adapted equation of state.

$$PV = ZnRT \tag{3.3}$$

Analysing the value of the compressibility factor can also be used as a decision-making criterion

when deciding between adopting an ideal gas assumption or attempting to adopt a real gas model.

## 3.2 Properties of hydrogen

As described in Section 3.1, gasses can be modelled either as an ideal gas or as a real gas and the compressibility factor is one way of approaching this. This section will aim to show how close the behaviour of hydrogen is to that of an ideal gas, which methods can be adopted to best represent the behaviour of hydrogen and will provide a physics-based explanation of why the behaviour of hydrogen is as it is.

### 3.2.1 Compressibility factor of hydrogen

As described in Section 3.1, the compressibility factor of a gas be calculated for distinct combinations of pressure and temperature. Figure 3.2 shows the compressibility factors of hydrogen, air, nitrogen and helium over a range of pressures and temperatures that can be expected in different hydrogen applications. These values directly stem from the open CoolProp library in Python which calls reference values from NIST.

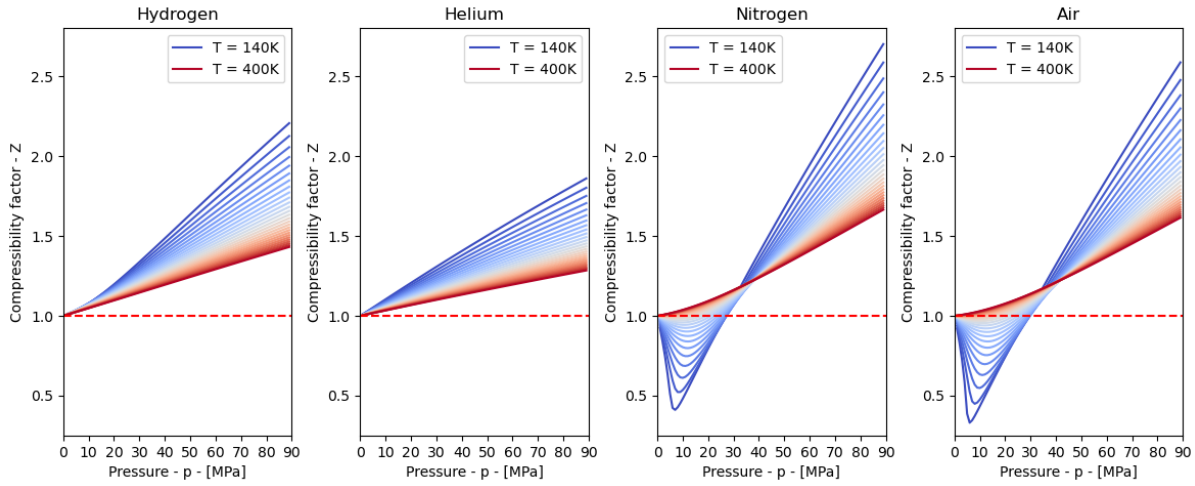


*Figure 3.2: Compressibility factors of hydrogen, helium, air and nitrogen for pressures between 1 and 90 MPa and temperatures between 140 and 400 K.*

As can be observed, for increasing pressures, the value of the compressibility factor of hydrogen rises steeply to values well above 1. Although one could argue that the simplified ideal gas assumption can be used for a calculation as long as one could provide an estimate of how much certain values would be over or under-estimated, it should be noted that the compressibility factor also varies a lot with pressure. Hence, for an expansion process in which the pressure significantly changes, this is likely not a suitable assumption as the error between the two states would also be different.

Furthermore, as can be observed, the variation of the compressibility factor of hydrogen is very different to that of air and nitrogen but similar to that of helium. As the compressibility factor is essentially a representation of the real equation of state of a gas it can be deduced that there are differences in how the pressure, temperature and density of a gas relate to each other between different gasses. In fact, this is closely related to a different behaviour often associated

with hydrogen known as the Joule-Thomson effect.

### 3.2.2 Joule-Thomson effect

The Joule-Thomson effect stipulates a temperature change in a gas when throttled through a valve or orifice without any heat exchange with the environment [85]. It is best represented by the Joule-Thomson coefficient as shown in Equation 3.4. Interestingly however, is that for select gasses such as hydrogen and helium, the Joule-Thomson coefficient is negative (for temperatures above 200K), as opposed to positive for most other gasses. In practice, this means that when hydrogen is expanded in an isenthalpic process, it will rise in temperature. This could be considered counter-intuitive when one is used to processes with different gasses, such as air, that feature a positive Joule-Thomson coefficient. [85].

$$\mu_{JT} = \left(\frac{\delta T}{\delta P}\right) \tag{3.4}$$

Figure 3.3 shows the Joule-Thomson coefficient for various gasses over a range of temperatures. Again it can be seen that hydrogen (for temperatures above 200 K) and helium have a negative Joule-Thomson coefficient as opposed to other gasses such as $CO_2$, $N_2$ and also air [86]. Clearly, there has to be a correlation between the Joule-Thomson coefficient $\mu_{JT}$ and the compressibility factor $Z$ and indeed, for gasses with $Z < 1$, the molar volume is lower than that assumed in an ideal gas and vice versa for $Z > 1$, the molar volume is larger [87]. This has a direct effect on the intermolecular attraction and repulsion forces as explained below:

- From the concept of Van Der Waals forces, it results that when a gas expands, and the distance between molecules increases, so does the potential energy between the molecules. If the expansion is indeed isenthalpic without any work done or heat exchanged, this means that the internal energy stays constant. But as the potential energy increases, this means that the kinetic energy has to decrease, resulting in a temperature decrease.
- On the other hand, as a gas expands and becomes more sparse, there are fewer collisions between different molecules. During a collision, kinetic energy is exchanged for potential energy and with fewer occurring collisions, this results in a reduction of the potential energy and an increase in kinetic energy, translating to a temperature increase.

As can be seen, these effects counteract each other, and the balance between these effects determines whether or not the temperature increases or decreases upon isenthalpic expansion. In practice, if the temperature is below a certain conversion temperature $T_{conv}$, $\mu_{JT}$ is positive and the temperature will decrease further upon expansion. However, if the temperature is above $T_{conv}$, $\mu_{JT}$ is negative and the temperature will increase. As can be seen in Figure 3.4, and also deducted from any T-S diagram of a medium, the magnitude in which temperature varies for a given change in pressure, $\mu_{JT}$, is also pressure dependent.

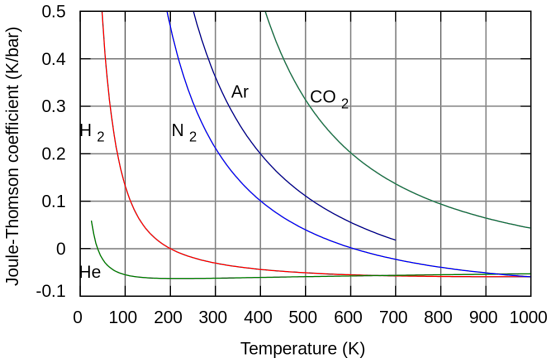


*Figure 3.3: A visualisation of the Joule Thomson coefficient of various gasses at a constant pressure [86].*

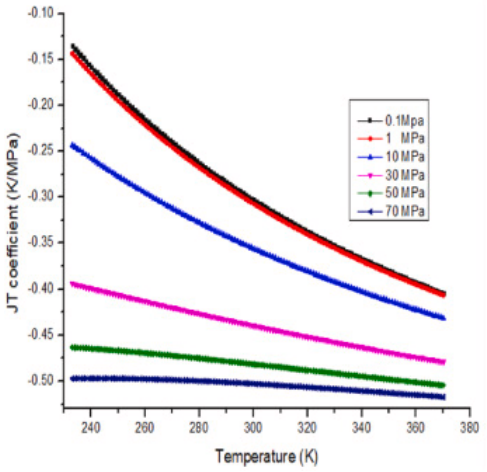


*Figure 3.4: JT coefficient curves of hydrogen at various pressures [88].*

## 3.3 Potential energy recovery of different hydrogen systems

It is quite well understood that when a gas gets compressed into a vessel, this vessel then stores a certain amount of potential mechanical energy. So aside from compressing gasses for storing larger amounts in smaller spaces, a second use of compressed gasses is extracting this potential energy, typically in the form of mechanical movement. Examples include any form of pneumatic actuators in mechatronic systems, to powering equipment in specific environments where electrical systems cannot be used because of the risk of sparks, electrocution or short-circuiting and many more [89]. In industrial applications, compressed air is, for example, also referred to as the fourth utility, after electricity, natural gas and water [89].

However, either of these cases uses a compressed gas, typically air, directly as a means to power a certain mechanical movement.

Opposed to that are other processes in which a pressure reduction is already present but where it serves no other use than just the expansion in itself. Quite often, Joule-Thomson expansion valves are used to create this pressure reduction or expansion, which then translates into a temperature shift. In the case of liquefaction of gasses, as explored in Subsection 2.2.3, this can indeed be of purpose, but rather often, this is just a side effect of a different process rather than the goal in itself.

This section will explore how much energy could theoretically be recovered in various applications of hydrogen.

As presented in Chapter 2, the field of hydrogen is quite extensive and not all hydrogen systems or applications can be directly compared in a qualitative way. However, in a best-effort attempt to do so based on some estimates and early assumptions, Subsection 3.3.1 will first provide a way to calculate the amount of potential energy that could theoretically be recovered in an adiabatic expansion process. Next, Subsection 3.3.2 through Subsection 3.3.5 will cover several systems that do show promise and after that Subsection 3.3.6 will briefly mention some applications that will not be considered further and provide quantitative reasoning as to why that is the case. Finally, a trade-off is presented in Section 3.4.

### 3.3.1 Potential energy estimates assuming adiabatic expansion

When considering a finite amount of high-pressure gas stored in a vessel of fixed volume, Equation 3.5 can be used to estimate the amount of energy that could be extracted adiabatically [90].

$$U = \frac{p_{t,1} V_1}{\gamma - 1} \left( 1 - \left( \frac{p_{t,2}}{p_{t,1}} \right)^{\frac{\gamma-1}{\gamma}} \right) \tag{3.5}$$

Equation 3.5 assumes a certain amount of gas to be stored in a vessel. For applications with a continuous supply, the term $V_1$ can be changed to $\dot{V}_1$, the volumetric flow rate. As per a unit analysis in Equation 3.6 and Equation 3.7, this would then result in energy over time, $J/s$ or power in $W$.

$$U = \frac{p_{t,1} V_1}{\gamma - 1} \left( 1 - \left( \frac{p_{t,2}}{p_{t,1}} \right)^{\frac{\gamma-1}{\gamma}} \right) = \frac{\left[\frac{N}{m^2}\right] \cdot \left[m^3\right]}{[-]} \cdot [-] = [N] \cdot [m] = [J] \tag{3.6}$$

$$\dot{U} = \frac{p_{t,1} \dot{V}_1}{\gamma - 1} \left( 1 - \left( \frac{p_{t,2}}{p_{t,1}} \right)^{\frac{\gamma-1}{\gamma}} \right) = \frac{\left[\frac{N}{m^2}\right] \cdot \left[\frac{m^3}{s}\right]}{[-]} \cdot [-] = [N] \cdot \frac{[m]}{[s]} = \frac{[J]}{[s]} = [W] \tag{3.7}$$

Although this method can be used to provide an initial estimation of how much energy could potentially be recovered for certain applications, there are a few important notes that should be kept in mind when analysing the results:

- No expansion process is 100 % efficient. Hence a certain amount of energy will not be able to be recuperated in the form of mechanical energy through an expander and will instead, through the losses such as friction, cavitation, turbulence and others induce a temperature change additional to the inherent temperature change that comes from the expansion process itself.
- This calculation assumes an adiabatic expansion which might or might not be true for every application.
- This calculation is originally based on total pressure values at each station which are dependent on a certain flow speed. When analysing the potential of each application later in this section, this is not yet known and static pressure values are used instead. Given the relatively high static pressures of most hydrogen applications and assuming that the flow speeds through these systems are not excessively high, the difference between static and total pressures will therefore be considered negligible for these initial estimates.

### 3.3.2 High-pressure storage vessels

High-pressure storage vessels typically store hydrogen at pressures up to 700 bar. However, most hydrogen applications, specifically mobile applications, only use it at lower pressures of 5 - 15 bar. Typically, the pressure in the system gets reduced by a spring-loaded pressure relief valve, and all the potential energy of the gas being compressed to such magnitudes is lost to thermal effects tied to the expansion process.

After surveying several available hydrogen vehicles that use high-pressure tanks, an average tank with a capacity of 5 kg and a pressure rating of 700 bar at ambient temperature is assumed.

Expanding this amount of hydrogen to 20 bar leads to a theoretical 3.72 kWh of energy that could be recovered. Assuming 85% efficiency [31] to convert the potential energy into mechanical energy through a turbo-expander and a 90 % efficient generator coupled to the shaft that still results in 2.845 kWh of electrical energy that can be used to directly to drive the vehicle or power any other processes. Compared to alternative electric vehicles that feature a similar range such as the Tesla P100 with a battery capacity of up to 100kWh, it can be seen that this is not an insignificant amount of recovered energy.

Naturally, this final value is only representative of the assumed average pressure vessel and pressure vessels of other sizes for different end applications (other vehicles such as trains, buses and trucks or stationary applications such as off-grid energy systems, generators or industrial processes) would result in different total values. However, this is taken as a tangible example to provide an estimate that can easily be put into perspective.

### 3.3.3 Salt cavern storage

As described earlier in Subsection 2.4.2, salt caverns can potentially be used to store large volumes of hydrogen for extended amounts of time. However, current applications remain limited as they are highly dependent on the availability of said salt caverns, which are also used for the storage of natural gas and oil. There are currently five existing examples of hydrogen storage in salt caverns, in Teesside (UK), Clemens (USA), Moss Bluff (USA), Spindletop (US) and Kiel (Germany) with pressures ranging between 45 and 150 bar [91]. Other research projects are ongoing for future implementations in the Netherlands, USA, Germany, France and Turkey [35, 36, 37]. When stored at 200 bar, it is estimated that the compression costs would be up to 9% of the energy stored in the hydrogen itself, but it is estimated that up to 70% of that expenditure can be recovered through a recovery device such as a turboexpander [92]. A planned project in Salt Lake City (USA) is estimated to be able to store up to 150,000 MWh of energy as hydrogen in such a cavern. Assuming a working pressure of up to 200 bar we can use the 9% rule to deduce that 13,500 MWh would be required to compress the hydrogen to this level and that up to 9,450 MWh of this could potentially be recovered per storage cycle [36].

Assuming that the mentioned 150.000 MWh of energy storage refers to the energy that can be used after the hydrogen is converted to electricity again (with 60% efficiency), this is equal to 250,000 MWh or 900,000 GJ worth of hydrogen that is stored in the cavern. Assuming the higher heating value of hydrogen, 141.9 MJ/kg [93] this leads us to a capacity of around 6,351.44 tonnes of hydrogen, which at 200 bar and standard temperature of 15°C results in a volume of 425,415 $m^3$. Again, assuming an expansion to 20 bar, this results in 10,253 GJ or 2,848 MWh. Which is quite a bit lower than the other assumption. Of course, there are several very big assumptions in these calculations, and they should also be considered as such but this can give an idea of the scale of this application and what that would mean for the practical design and implementation of an expander.

### 3.3.4 Pipelines

As mentioned before in Subsection 2.3.2, pipelines are a promising way of transporting large amounts of energy over large distances. Although specific networks of hydrogen pipeline infrastructure exist it is not as widespread as that of natural gas. When looking at existing hydrogen pipeline networks and also taking natural gas infrastructure pipelines as an example, it can be seen that depending on the size of a specific branch and the transported volume, there are in general various different pressure levels. In theory, each junction where there is a pressure

differential will either require a compressor or has the potential of a pressure recovery device. Given the vast volumes of gas passing through existing gas pipeline networks, the potential is large, even if the pressure head is not. However, with the large variability between sizes and pressure levels of pipeline infrastructure, it would be difficult to provide a general one-size-fits-all solution or estimate how much energy a single device could recover.

### 3.3.5 Hydrogen refuelling stations

In hydrogen refueling stations, hydrogen typically flows from a large high-pressure buffer tank to a lower-pressure tank in a vehicle. Although the pressure differential obviously decreases as the refuelling process progresses, there is a significant pressure differential between the two sides where energy can potentially recovered.

However, aside from only the pressure differential, Chen et al. [31] have shown an additional potential of adding a turboexpander in a refuelling cycle. As per refuelling standards for automotive applications, most in-vehicle storage vessels are only rated up to 85°C. However, as explained in Section 3.1, this expansion process in the refuelling cycle results in the gas increasing in temperature significantly. So much that, per the SAE J2601 and UN GTR13 regulations [94, 95], the hydrogen gas needs to be precooled to between -33 and -40°C to not let the final tank temperature overshoot the limit of 85°C. This cooling process is rather energy intensive and as Chen et al. has shown, a turboexpander could potentially be used to not only recover energy from the pressure differential but also to use the expansion process to pre-cool the hydrogen, essentially saving energy in the refrigeration cycle. In total, it is predicted that this could recover and save up to 1.647 kWh per refuelling cycle [31].

In order to provide a first estimate of how much energy could be recovered through the expansion process, a few assumptions are made:

- The buffer tank provides hydrogen at a pressure of 700 bar.
- To be consistent with previous calculations, the amount of hydrogen in each refuelling cycle is assumed to be 5kg, which at 700 bar and 15°C equals 0.124 $m^3$ or 124 litres.
- As the to-be-refuelled tank changes in pressure during the cycle an average is taken between a full (700 bar) and an empty tank (50 bar) at 375 bar.

This results in an initial estimate of 3.54 MJ or 0.983 kWh. Applying an 85% expander efficiency and a 90% generator efficiency leads to 0.442 kWh per refuelling cycle.

### 3.3.6 Other disregarded hydrogen systems

Chapter 2 provided a general overview of the most important elements in the hydrogen value chain. However, when searching for an application in which potential energy from compressed hydrogen can be recovered, several of the mentioned systems are simply not applicable.

Firstly, electrolysers are not further explored as they typically operate at relatively low pressures and the generated hydrogen leaves the system at pressures between 1 and 5 bar and, as has been explained in Section 2.3, most transport and distribution systems operate at higher pressures. Hence on a system level, compression is required as opposed to expansion. Following the same reasoning, SMR plants are discarded. Although these do operate at higher pressures than electrolysers, they are generally still well below the pressures at which hydrogen is stored and on the lower end of the pressures that can be expected in a pipeline network.

Secondly, liquefaction plants. Many articles on the topic of hydrogen liquefaction indeed show that there can be a turboexpander involved in the cooling process. However, due to the multitude of listed examples and processes, it can be concluded that turbo-expanders are already very commonplace in the liquefaction industry. Indeed, a lot of energy is recovered by expanding hydrogen and indeed, a lot of energy is saved by cooling the gas through this process rather than through heat exchangers but for the scope of this study, it is deemed not very relevant as it is already commonplace and well established.

Thirdly, liquid hydrogen tanks, although liquefaction plants will be mentioned in the following subsection, the tank systems and installations to store liquid hydrogen also operate at rather low pressures with only a minimal pressure difference to the applications that they aim to provide with fuel.

Last are most of the end applications of hydrogen, neither the combustion processes found in internal combustion engines and furnaces, the electrochemical processes in fuel cells or the processes involving hydrogen as a reduction agent in metallurgy present an inherent step in their process in which an expansion is present from which potential energy can be recovered. Each of these processes are however supplied with hydrogen, typically from pressure vessels or via gas pipelines. So instead of exploring these specific end applications, their respective storage and distribution systems will be analysed.

## 3.4 Selection of the most suitable application to recover potential energy from.

Following the brief analysis of several systems that could be suitable to recover potential energy from, this section aims to provide a trade-off between the analysed systems. This results in one application that shows the highest promise, which will be explored in more detail and used as a basis to develop a conceptual expander design. Please note that due to the difference between these systems, this trade-off is rather quantitative.

Some aspects that have been taken into consideration are:

- Scale in terms of the number of possible installations.
- In- and outlet pressure levels and their variability.
- Capacity in terms of the amount of hydrogen expanded.
- Limitations on size, weight and cost.

These aspects are shown in Table 3.1

Based on this, it appears that there is less immediate relevance for the case of salt cavern storage simply because of the lack of existing installations and the lack of similarity between them as the ones that do exist vary greatly in terms of pressure and capacity. The conceptual design of an expander for this system would be very specific and tailored to one specific installation. Next, applications for systems based on high-pressure storage vessels - mostly mobile applications - are questionable because of the cost, size and weight limitations of mobile applications as well as the relatively small system throughput or mass flow. The case of pipeline infrastructure remains plagued by a lack of clarity surrounding operating pressures and throughput of the system.

Hydrogen refuelling stations seem more promising because of the existence of standard fuelling protocols, resulting in any solution of an expander being more broadly applicable. As a bonus,

applications in refuelling stations allow for pressure recovery and a reduction in cooling requirements, which comes with another significant operational energy saving. Chen et al. [31] has already shown the economic feasibility. Furthermore, it is also the only application for which some previous work has been found on the topic of recovering potential energy from compressed hydrogen.

Based on these considerations, the following chapter will dive deeper into the specifics of hydrogen refuelling stations.

| | **Advantages** | **Disadvantages** |
|---|---|---|
| High pressure storage vessels | • Majority of mobile and off-grid applications, large market, potential for standardised components.<br>• Typically a large $\Delta p$. | • Size, weight and cost limitations for mobile use.<br>• Large operating window, varying inlet pressure<br>• Limited capacity due to tank volume.<br>• Large off-design operation |
| Salt cavern storage | • Large capacity, volumetric size of salt caverns.<br>• Size, weight & cost are quasi irrelevant. | • Relatively low pressures.<br>• Few existing applications.<br>• Limited potential due to geographic needs.<br>• Large infrastructure, no standard components. |
| Pipelines | • Relatively constant in- and outlet conditions.<br>• Size, weight & cost are irrelevant. | • Uncertainty about pressure levels. Not the same for all applications.<br>• Large investment needed for infrastructure. |
| Hydrogen refuelling stations | • Can also be used to reduce cooling requirements.<br>• Large market, supply for mobile applications.<br>• Size, weight & cost are irrelevant.<br>• Standardised process, potential for standard components. | • Variable in- and outlet pressures.<br>• Large off-design operation. |

*Table 3.1: An overview of the strong and weak points of several applications in the hydrogen value chain considering the implementation of hydrogen expanders.*

# 4 Hydrogen Refuelling Stations (HRS)

As Section 3.4 concluded that hydrogen refuelling stations were the most suitable application to recover potential energy from, this chapter will be dedicated to the details of such stations. First, Section 4.1 will provide a more in-depth overview of the operation of hydrogen refuelling stations and the two main types that are considered after which Section 4.2 will go over previous research on the topic of recovering potential energy from compressed hydrogen in hydrogen refuelling stations. Next, Section 4.3 explains the model that has been written for this thesis with a detailed overview of the assumptions and governing equations behind each component in the system model.

## 4.1 HRS system overview

As covered in Section 2.5, an important application of hydrogen is the electrification through fuel cells. For mobile applications, this also requires refuelling stations where end consumers can refuel their vehicles or trailers meant for the transport of hydrogen can be filled up.

Although there are many different operators of such refuelling stations, each of which can implement slightly different system architectures, the general system layout of a refuelling station can be represented by the schematic in Figure 4.1.

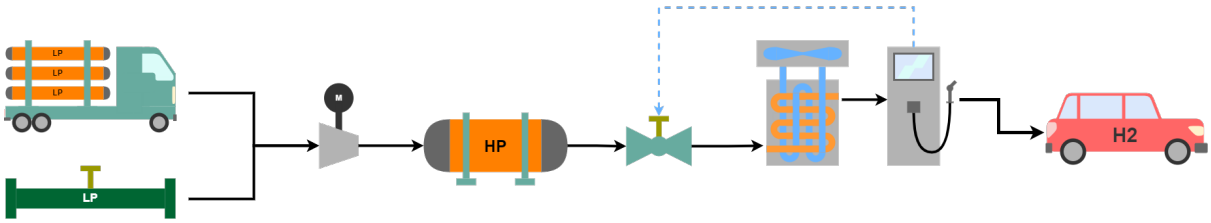


*Figure 4.1: Schematic configuration of a hydrogen refuelling system (HRS), adapted from Chen et al.[31].*

As can be seen in Figure 4.1, from the supply point, the hydrogen gas is compressed up to either 500 or 900 bar and stored in a series of buffer tanks [96]. After these buffer tanks, there are control valves present to regulate the outflow of hydrogen, which then gets pre-cooled to approximately -40°C, after which it gets dispensed in the vehicle, typically up to either 350 or 700 bar [31].

A few notes that can be made about this general layout: Firstly, the control valves typically regulate the mass flow through the system based on the maximum allowed Average Pressure Ramp Rate (APRR) which is a value set and monitored by the refuelling station based on ambient, vehicle and station conditions in order to prevent overheating of the tank. The exact protocols which determine the APRR can be found in the SAEJ2601 regulations [94]. Secondly, the purpose of the cooling cycle is to pre-cool the hydrogen as both the expansion through the reduction valve and its injection in the final tank introduce a temperature increase and the final temperature in a vehicle tank should remain under 85°C, per regulations SAEJ2601 and UN GTR13 [94, 95].

There are two different physical mechanisms through which this heating happens. Firstly, in the expansion valve, the gas is typically throttled isenthalpically and by virtue of the Joule-Thomson effect explained in Section 3.2 and shown in Figure 3.4 hydrogen will indeed heat up.

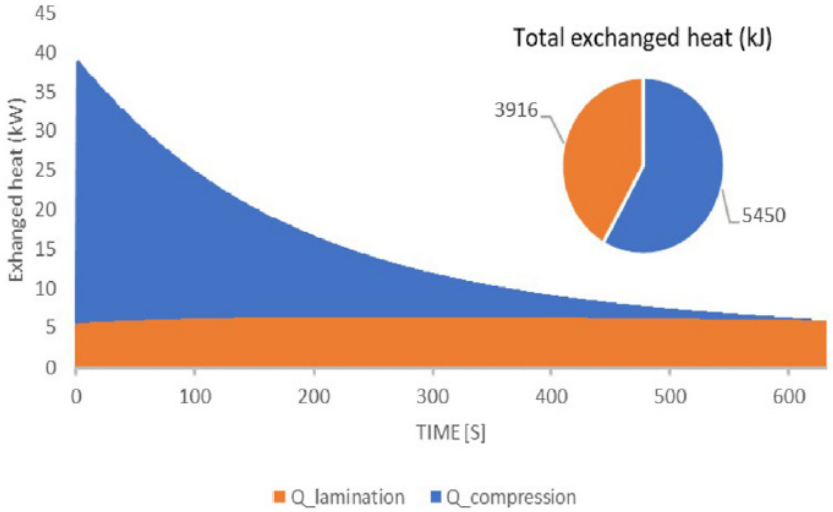


*Figure 4.2: Relative contributions of the heat exchanged in the isenthalpic expansion process and tank compression of a hydrogen refuelling cycle from Caponi et al. [97]. $Q_{lamination}$ represents the heat exchanged in the expansion process through an isenthalpic valve and $Q_{compression}$ represents the heat exchanged in the final compression of hydrogen in the vehicle tank.*

The second part of the heating stems from the heat of compression occurring in the vehicle tank itself [97]. An example of the different contributions of either part can be seen in Figure 4.2 as presented by Caponi et al. [97].

However, not every refuelling station is built around the exact same architecture as there are differences in the overall size and capacity of the system, the number of buffer tanks, and the delivery pressures the station is designed around. In an attempt to provide a holistic overview and design an eventual model around sensible parameters, the following two subsections 4.1.1 and 4.1.2 will provide an overview of the two main types of refuelling stations.

### 4.1.1 Single buffer refuelling stations

As shown in Figure 4.1, the most basic version of a hydrogen refuelling station is built up in the following way: Hydrogen is supplied at pressures up to 200 bar via pipelines or tube trailers. From there, it is locally compressed to the desired higher pressure in a buffer tank. The pressure in this buffer tank generally varies between 750 and 900 bar. Once stored in a buffer tank, the system is ready to refuel vehicles. During refuelling, the tank valves open, and hydrogen starts flowing through the system. The first component in this system is a reduction valve, which is actively controlled and reduces the pressure to match the pressure in the vehicle tank and limit the pressure ramp rate in the vehicle tank. A side effect of expanding hydrogen through a reduction valve is that its temperature rises due to the negative JT coefficient, as explained in Section 3.2. If left unchecked, this would lead to a significant temperature increase downstream of the expansion valve and eventually in the vehicle tank, which is undesirable. In fact, the properties of the materials used in the vehicle tanks dictate general gas temperature limits of -40°C and 85 °C inside a type IV pressure vessel. In order to ensure that these temperature limits are met throughout the entire refuelling process, the next component in the refuelling station is a heat exchanger, also referred to as chiller or pre-cooler, which typically cools the hydrogen gas down to -33°C. After the heat exchanger the hydrogen flow passes through the dispenser which includes all the safety features to ensure a secure connection to the vehicle system and might have an active communication to on-board sensors in the to-be-refuelled vehicle. This

communication line can provide real-time information about the gas temperature in the vehicle tank which can be used to control the regulation of the expansion valve more accurately. If such a communication line is absent, refuelling stations typically use pre-defined protocols that depend on the initial tank pressure and ambient temperature conditions. Once passed through the dispenser, the hydrogen flow works through the vehicle system and ends up in the vehicle tank.

As the system operates through multiple refuelling cycles, the pressure in the large buffer tank will eventually reduce, which could limit the pressure until it can refuel a vehicle. Because of this, HRS, just like regular gas stations, should be periodically refuelled when supplied by tube trailers.

As all the gas passing through the system is at some point compressed to a very high pressure (750 - 900 bar) and then expanded to vehicle level, it can be easily understood how an HRS has relatively low energy efficiency. One solution to make this process more energy efficient is refuelling stations with multiple buffer tanks at various pressures, also called cascade refuelling stations.

### 4.1.2 Multi-buffer refuelling stations

For the largest part of the process, multi-buffer or cascade refuelling stations operate in the same way as a single buffer refuelling system with the one exception that instead of a single large high-pressure tank, the buffer system consists of multiple tanks at various pressure levels. The literature shows that the generally agreed-upon optimal amount of buffer tanks is 3 [98].

For further reference in this thesis, a system with 3 buffer tanks will be assumed. In such a system, there are low, medium and high-pressure tanks. As an "empty" vehicle arrives with a low internal tank pressure, the refuelling cycle will start refuelling the vehicle from the lowest pressure buffer tank, typically around 250 - 350 bar, until an equilibrium or a minimum expansion ratio is achieved. After this, the refuelling station switches to the medium-pressure tank, which will continue refuelling the vehicle until an equilibrium is reached. Finally, the high-pressure tank continues until the vehicle tank reaches its desired pressure. These three steps will be referred to as "phases" of the refuelling cycle in any further discussion. An example of this system layout can be seen in Figure 4.3

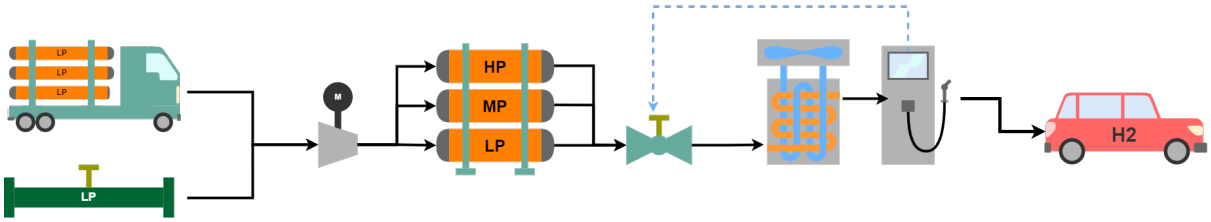


*Figure 4.3: Schematic configuration of a hydrogen refuelling system (HRS) with three different buffer tanks.*

Although this is inherently a more complex system to operate, this type of refuelling station has several distinct advantages over single-buffer systems:

- As not all the gas that passes through the system needs to be compressed to the highest pressure, there is less energy expenditure in terms of compressing hydrogen between the supply and the buffer tanks.

- As there is a lower expansion ratio over the expansion valve in each of the three phases of the refuelling process, there is a lower temperature increase over the expander, resulting in lower cooling requirements for the downstream heat exchanger.
- Since less mass flows out of the highest pressure tank, the pressure in the highest pressure tank drops less per refuelling cycle than for an equivalent system with a single buffer tank. Hence, the amount of refuelling cycles that a system can have for a given amount of stored hydrogen in the buffer tank is higher [99].
- As several buffer tanks hold lower maximum pressures, these can be manufactured to lower specifications, resulting in cheaper infrastructure costs.

These benefits show that multi-buffer systems would be preferred even for traditional hydrogen refuelling stations as they generally result in lower operating costs. This conclusion has also been confirmed by several other studies that looked into optimisations of hydrogen refuelling stations and processes:

- Caponi et al. found an energy reduction of 20 % in the generated heat and 10 %, 18 % and 32 % reductions in the energy spent on compressing hydrogen to the various buffer tanks [97].
- Xiao et al. found a 34 % overall reduction in energy consumption for a 3 cascade HRS as opposed to a single buffer system [100].
- Rothuizen et al. found an optimum of 3 cascade tanks, resulting in a 12 % and 17 % reduction of energy usage for cooling and compression respectively [98, 101].

### 4.1.3 Recovering potential energy from compressed hydrogen in an HRS

When considering recovering potential energy in an HRS it naturally makes sense to do this for the most relevant or most representative type of system. Considering the arguments presented in the previous subsection, a multi-buffer system is naturally the most logical choice. However, when considering the feasibility of implementing energy recovery systems in existing systems, it would be sensible to consider which type has in fact been built more. Unfortunately, retrieving data on the exact system architecture of existing HRSs has proven unsuccessful.

However, when considering recovering energy from compressed hydrogen through an expander, there is one more possible advantage of a multi-buffer system architecture: The variability of the expansion ratio of the expander.

For a short illustrating comparison, the following parameters will be assumed:

- The minimum vehicle pressure is 50 bar.
- The maximum vehicle pressure is 700 bar.
- Single-buffer station pressure is 900 bar.
- Multi-buffer station pressures are 250, 500 and 900 bar in the respective buffer tanks.
- The capacity of the buffer tanks is sufficiently large with respect to the vehicle tank that the mass exchanged in a single refuelling cycle does not affect the pressure in the buffer tanks.
- Each buffer will continue to be used until an equilibrium is reached between the buffer tank and the vehicle tank or until the maximum pressure of the vehicle is reached.

In a single-buffer system, the expansion ratio over the expander would thus vary between 18 and 1.28. Whereas for a multi-buffer system the expansion ratio would range between 5 and 1 for the lowest pressure buffer tank, between 2 and 1 for the middle pressure tank and between 1.8 and 1.28 for the highest pressure buffer tank.

Regardless of the type of expander that would be used to recover energy from this expansion process, it would be designed around a single design point but its efficiency would be determined by how well it performs in off-design conditions. Logically, the closer its off-design operating points are to the design point, the more efficient it would operate overall. From this, it can be reasoned that designing an expander for a multi-buffer system would be inherently more efficient than designing one for a single-buffer system as the range of the operating condiitons is smaller.

## 4.2 Previous work on recovering potential energy in an HRS

As mentioned in Section 3.4, hydrogen refuelling stations are the sole application for which research on recovering potential energy has been found in open literature. The available published literature consists of the following three sources from Burgess, 2018 [102, 103], Yoshida, 2019 [104] and Chen, 2022 [31], each of which will be covered in the following subsections.

### 4.2.1 Burgess, 2018

**Turboexpander: Alternative Fueling Concept for Fuel Cell Electric Vehicle Fast Fill** [102, 103]:

These two publications present the publicly available results of a research program conducted by the National Renewable Energy Laboratory (NREL) of the Department of Energy (DOE) in the USA, which was co-funded by Toyota and Honda. The premise of the research included the conceptual development of a turboexpander for fast-fill procedures in hydrogen refuelling stations to lower the costs of dispensing hydrogen, specifically to mitigate the cooling requirements that come from expanding hydrogen through a valve. The initial project objectives included a performance analysis and initial sizing of such a system as well as the fabrication of a test set-up and subsequent system testing.

As far as is available in the publicly available literature, this project concluded with two conceptual turbine designs, a radial inlet turbine and a drag turbine, which were to be implemented in a test set-up. The initial drag turbine design resulted in the following sizing parameters: Diameter = 0.75 inch (19.05 mm), $\omega$ = 200,000 rpm, and it would need to be manufactured with 0.0002 inch (0.0508 mm) tolerances. No further information on a radial inlet design was disclosed, and unfortunately, no other project updates or details on calculation methods have been published after this.

### 4.2.2 Yoshida, 2019

**Thermodynamic analysis of high-pressure hydrogen gas refuelling system with turboexpanders** [104]:

This research focused on the thermodynamic simulation of integrating a turboexpander in a hydrogen refuelling station and its effects on the energy requirements of the required cooling system of the HRS. It assumed the refuelling of a 150-liter hydrogen tank (with a capacity of

approximately 5 kg) in 3 minutes. It provides the assumption of a radial inlet turbine design with a 10 mm rotor diameter and a rotor speed of $\omega$ = 1,000,000 RPM with an assumed isentropic efficiency of 65%. Using these parameters, the study resulted in estimates of the turbine outlet temperature and how it would affect the subsequent cooling requirements of the chiller.

It is also interesting to note that the authors filed for a patent application of such an expander system in 2017. However, following the previously mentioned publications from NREL, this patent filing has supposedly been withdrawn [102, 103, 105].

### 4.2.3 Chen, 2022

**Dynamic simulation of the potential of integrating a turboexpander in a hydrogen refuelling station** [31]:

This publication from 2022 is the first and so far only publicly available publication that considers the energy recovery from expanding hydrogen between a high-pressure and a low-pressure state and includes this in the energy budget of the system. However, the focus of the research is still primarily focused on the system model of the refuelling station instead of the expander's design. Some relevant assumptions include a 174-litre vehicle tank with a 7 kg capacity, a maximum mass flow rate of 60 g/s (following refuelling protocols) and an expander efficiency of 60%. It draws conclusions about the economic feasibility of an expander in an HRS based on infrastructural and operational cost savings as well as development costs. Specifically, a 52% operational cost saving on the energy expenditure of the pre-cooler and a $210.000 capital cost saving based on the cost of pre-cooler installations and estimated development costs of the turbo-expander. however, apart from a single mention of an rotor speed of 1.000.000 RPM it fails to detail how this expansion is achieved.

### 4.2.4 Research gap

Based on these sources and the trade-off presented in Section 3.4 it is clear that refuelling stations indeed pose a suitable application in which energy can be recovered from compressed hydrogen. However, the review of the past studies also highlights a clear research gap surrounding the actual design of such an expander.

All three refer to turboexpanders designed to operate at extremely high rotational speeds. The study by NREL shows any mention of an actual design, but even that is limited to a single mention of sizing charts from Balje [106] to provide estimates on the specific speed and diameter of certain types of turbomachinery. Yoshida et al.'s study mentions an assumed diameter and rpm but no reference to where those estimates originate. Lastly, the study by Chen et al. only mentions the same RPM limit, likely in reference to the study by Yoshida et al.

Next to the lack of any geometric design parameters of proposed expanders, neither of the three studies provides any reasoning for the predicted efficiencies. Regarding the modelling of the expansion over the expander, the study by Yoshida et al. only refers to the assumed efficiency and calculated enthalpy values. It appears that this assumes a single calculation of the temperature ratio from the expansion ratio following isentropic relations with the assumed efficiency applied to it. The study by Chen et al. goes into slightly more detail by providing the equation used to estimate the temperature at the turbine outlet, which is indeed only based on the pressure ratio and an "equivalent process index". However, this so-called "equivalent process index" is calculated through a 6th-degree polynomial equation based on the pressure ratio and includes 6 different numerical coefficients which are not explained or referenced at all.

However, the form of this polynomial equation does remind of similar equations used in real gas models to predict the heat capacity ratio of a gas. It is the author's assumption that this equation is used to provide a more real prediction of the expansion process than the standard isentropic relations but without more details on the actual coefficients or equations used, this remains an assumption.

Lastly, all three studies refer solely to single-buffer systems. Given the previously explained large variability of expansion ratio during a refuelling cycle in a single-buffer system, a similar turboexpander, applied to a multi-buffer system with less variability in its expansion ratio, should yield an increase in efficiency.

## 4.3 System model of the hydrogen refuelling station

As a trade-off between various hydrogen applications has been performed in Section 3.4, specific literature regarding recovering potential energy from compressed hydrogen in hydrogen refuelling stations has been explored in Section 4.2 and the general system layout of a refuelling station has been explored in Section 4.1. This section will continue with establishing a computational model of an HRS. The aim of this model is first to predict the effect of an expander throughout the entire refuelling process. Second, to determine a suitable design point for the expander and third, to analyze the performance of a designed expander over the entire refuelling process, both at the design point and in off-design conditions.

Although the model should be based on the architecture of an actual HRS it should be noted that blindly adopting such a system architecture, and specifically the control of the system, would likely lead to sub-optimal results for the performance of the expander. Because of this, several adaptations have been made to the boundary conditions, system parameters and the control strategy of the system. These will be presented and explained in Subsection 4.3.1 together with a few other simplifications and assumptions. Next, Subsection 4.3.2 will provide a top-level overview of the constructed system model as well as delve into the specific calculation steps and governing equations of each component in the system model.

### 4.3.1 Adaptations for a refuelling station system model

First, several physical assumptions have been made to simplify the modelling of the system:

- The system is assumed to be adiabatic, with no heat exchanged between system components and the ambient environment.
- The connecting pipework of the system is assumed to be frictionless.
- The system is modelled as a quasi-steady state; every time step is considered as its own steady state with no transient behaviour over time. However, between two time steps, old values are used as input to the boundary conditions or as initial guesses of variables. As these are iterated over time the whole model does show a dynamic operation.

The adiabatic assumption is a limitation as several others have studied the effect of heat dissipation to the environment on the energy efficiency in hydrogen refuelling stations. Specifically, the heat transfer between the buffer tanks, vehicle tank, expander and the ambient environment. However, as the aim is to design and model the effect of a turboexpander in a generic refuelling station, these calculations would require material specifications and assumptions of operating conditions that fall beyond the scope of this thesis. Furthermore, the connecting pipework is

assumed to be frictionless, resulting in no losses energetic losses between system components. This is considered because the overall effect of the expander on the system is expected to be far more significant than the losses in pipework and because these calculations would also require specifications beyond this thesis's scope such as the length of the actual pipework. A further reason is that friction losses in pipework are easily mitigated as they are almost inversely related to the cube of the diameter, hence a small change in pipe diameter can result in a significant reduction of friction losses. One exception to either of these assumptions is the chiller. As will be explained in Subsection 4.3.5, this part is designed to introduce a temperature change and also results in a significant pressure drop.

Next, there are several assumptions implemented that affect the operation of the system:

- Assumed tank volumes.
- Assumed initial tank pressures.
- Assumed fixed pressure losses.
- Assumed vehicle specifications.
- Assumed mass flow limits.

In order to accurately predict the expansion ratio over the expander, the buffer tanks are modelled to have a finite volume and defined initial pressures. These were initially tailored to the results of an optimisation study of multi-buffer refuelling stations by Xiao et al [100] but have since been altered to prioritise optimal expander performance by providing an as similar as possible expansion ratio in each phase of the refuelling process. The previously mentioned chiller and also the dispenser have been assigned a fixed pressure loss as will be further detailed in Subsection 4.3.5. A hydrogen vehicle has been assumed with a fixed tank volume and pressure limits which mimics a light goods vehicle such as a delivery van or a small truck. Do note that variations of this will be covered in Chapter 6 when discussing the results.

Although the value of the assumed corrected mass flow rate had initially been scaled to limit the achieved mass flow rate to 60 g/s, as dictated by SEAJ2601 refuelling protocols, this has later been scaled up to a limit of 120 g/s to improve the viability of the expander design. The change has been considered valid as the value of 120 g/s has been proposed as a realistically achievable limit for heavy-duty refuelling protocols and because the rationale behind the limit in regulations is tied to the temperature increase that a higher mass flow would introduce in a typical expander. However, as previous work has predicted and as the results in Chapter 6 will show, this effect is not present when a turboexpander is applied as the gas will cool down upon expansion instead of heat up. An effect of the increased mass flow, however, is that the refuelling time is also significantly sped up, which can be considered a positive side effect.

Finally, a few assumptions have been made regarding the design of the turboexpander and its effect on the control of the mass flow rate through the system.

- A single-stage radial inlet turbine will be used.
- The mass flow is limited by a fixed corrected mass flow rate and controlled by the performance of the turboexpander as opposed to a constant APRR.

The decision of using a single-stage radial inlet turbine design is primarily based on the examples provided in the available literature on this type of application. It is further supported by the mechanical simplicity of rotating turbomachinery and the simplicity of a single-stage design.

Furthermore, for a single-stage design, a radial turbine can achieve relatively high expansion ratios which would be favourable for this application.

The way in which the mass flow through the system is controlled has been significantly changed. In traditional refuelling stations, this is controlled by the station to maintain a steady Average Pressure Ramp Rate (APRR) on the vehicle side which leads to a specific profile of mass flow over time through the system. However, when implementing a recovery device such as a turboexpander, it might be more beneficial to tune the mass flow so that the expander can operate as efficiently as possible. As will be shown in Subsection 4.3.4, this has been put into practice by assuming a fixed corrected mass flow rate which translates to an actual mass flow rate dependent on the expansion ratio over the expander.

### 4.3.2 Top level model overview

The general top-level procedure of the calculations in the system model can be observed in Figure 4.4. It could be described as a quasi-steady-state model in the sense that it performs a series of static calculations at defined stations in the system for a single time step and that this is repeated for several time steps until a condition is met. So for a complete refuelling cycle, the in- and outputs of these calculations indeed vary over time, but there are no transient states or transfer rates of variables between these time-steps. Once all the stations have been analysed, several parameters are used to update the initial assumptions, and the process is repeated.

The model starts with initialising certain conditions (pressure, temperature and mass) in the buffer tanks, together with an initially assumed mass flow which leads to inlet conditions of the expander. Based on the inlet conditions of the expander and the initial values of the to-be-refueled vehicle, an expansion ratio can be determined, leading to a detailed calculation of everything that occurs in the expander. This includes calculating the velocity components at different points in the expander, 1D geometrical design calculations, power calculations and efficiency predictions. The calculations of the expander also provide a new updated value for the mass flow. These calculations then lead to updated conditions at the expander outlet from which the calculations at the nozzle of the HRS can be calculated. Eventually, this then leads to updated conditions in the vehicle tank.

Once the calculations have been performed for a single time step, several values, such as the mass flow and expander outlet conditions, are used to update the initial conditions in the buffer tanks and determine a new expansion ratio. The calculation steps are then repeated until the vehicle tank reaches its target pressure. The assumed time step is 1 second.

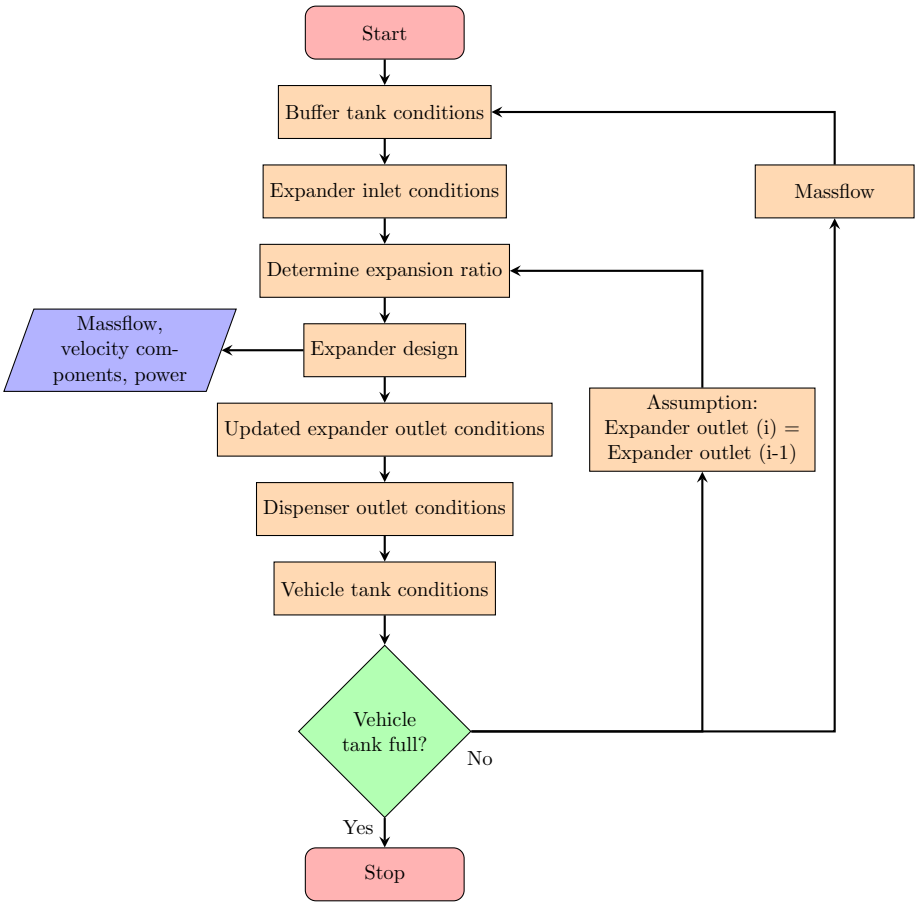


*Figure 4.4: Top level structure of the hydrogen refuelling station system model.*

Next to the order in which calculations are performed, as shown in Figure 4.4, the system model naturally needs to represent the processes that occur in an actual refuelling process. In order to do so, the system has been divided into a number of stations, visualised in Figure 4.5, which represent the points in the system at which certain variables are calculated. The calculations performed between each station represent a process or the functioning of a device between these two stations. As mentioned in Subsection 4.3.1, the expander is assumed to be a single-stage radial inlet turbine which is reflected in the numbering of the various stations.

The system has been divided into 8 stations:

0. The buffer tanks of the refuelling station.
1. The inlet of the expander and of the stator vanes of the expander.
2. The inter-nozzle row, between the stator and rotor of the expander.
3. The exit of the rotor and inlet of the diffuser of the expander.
4. The exit of the diffuser of the expander and inlet of the chiller.
5. The exit of the chiller and inlet of the dispenser.
6. The outlet of the dispenser of the refuelling station.
7. The vehicle tank.

In order to provide a clear description of the performed calculations, each of the following

subsections will represent a major component in a hydrogen refuelling station and detail the governing equations and calculation methods used to model that part.

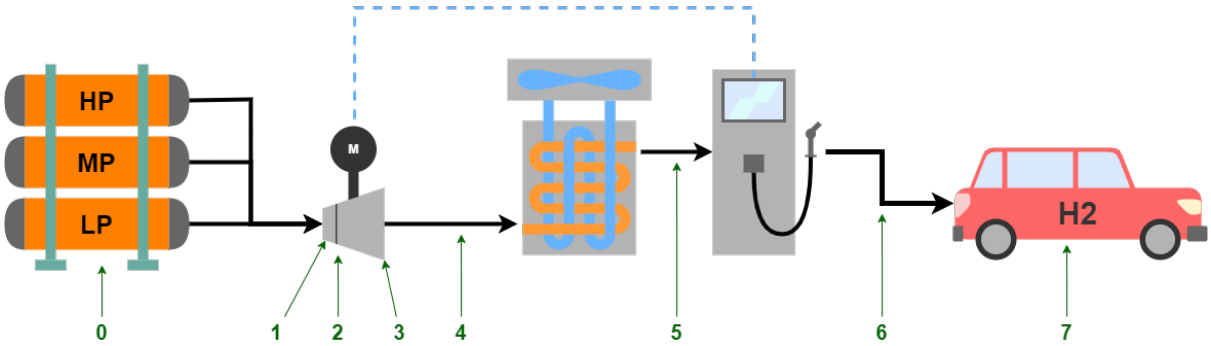


*Figure 4.5: An overview of the station numbering of the system model.*

### 4.3.3 Buffer tanks

The HRS system model's first component is the array of buffer tanks. As mentioned, the system model assumes a multi-buffer system with 3 tanks at various pressure levels. However, at any point during a refuelling cycle, only one of these buffer tanks is in use. The condition under which the system switches from one buffer tank to another is dependent on the expansion ratio. Based on this information, one of the tanks is initialised in the system and its mass and volume from the previous time step are assumed. Next, the mass flow that has been calculated in the previous time step is subtracted from the mass in the tank and the density of the gas in the tank is re-calculated. As mass has flown out of the tank and the gas density has decreased, the gas in the tank has essentially undergone an expansion process, influencing the pressure and temperature of the remaining gas in the tank. In order to determine this change, first a guess of the new temperature is made by setting it equal to the previous temperature in the tank. Next, the FluidProp module is used to calculate the gas pressure of hydrogen at the new density and assumed temperature. Then, the expansion ratio from the previous time step to the current one is used to calculate the temperature change that would occur with it, assuming an isentropic expansion. This is used to recalculate the gas temperature in the tank. Finally, the newly calculated gas temperature is compared to the initial temperature guess and if the ratio is too large, more than 1% difference, the calculation is iterated by setting the new temperature guess equal to the calculated value. This continues until the temperature converges and the mass, density, pressure and temperature in the buffer tank are defined for this time step. This process is visualised in Figure 4.6.

After these values are calculated for the buffer tank itself, the pressure, temperature and density can be parsed to the station at the inlet of the turbine as the system is assumed to be adiabatic and frictionless between components. Together with the mass flow and a pre-defined pipe diameter, the velocity in the pipe can also be calculated, leading to total pressure and temperature values. Finally, CoolProp is used to determine the corresponding static and total enthalpy and the total pressure and temperature at the turbine inlet, as seen in Figure 4.7.

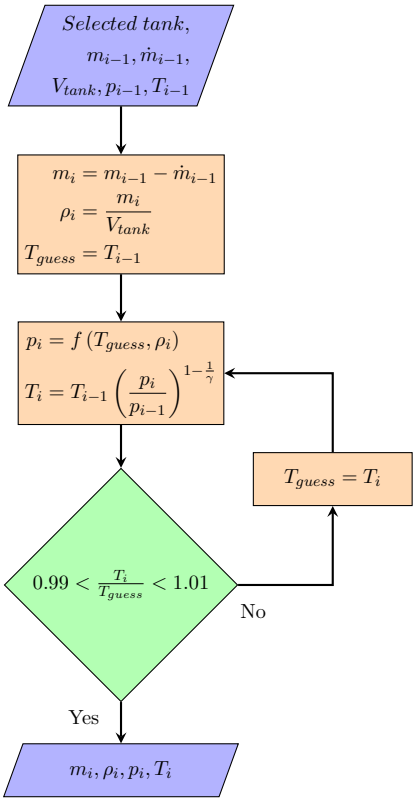


*Figure 4.6: Calculation procedure of the mass, pressure, temperature and density in the buffer tanks of the HRS based on a change of mass in a fixed volume tank.*

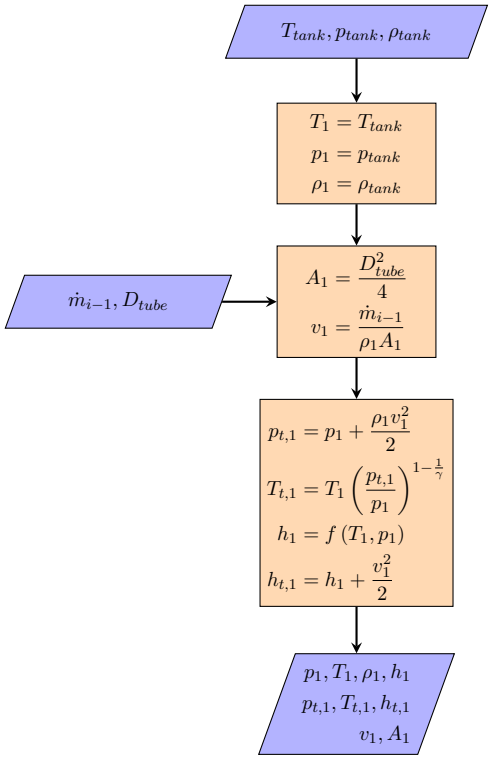


*Figure 4.7: Calculation procedure of the gas conditions at the turbine inlet.*

### 4.3.4 Expander

As explained in the top-level overview of the system model, the calculations are performed from station to station for every time step and then iterated until the refuelling process is complete. Therefore, the calculation of the expansion ratio of the expander can only be calculated with respect to the previous outlet conditions of the expander, as the current ones are not yet known. As can be seen in Figure 4.8, the model indeed uses the pressure at station 4 (The diffuser outlet) as an initial guess to calculate a temperature ratio across the entire expander, assuming an isentropic expansion. The flow velocity and total values can be calculated with the mass calculated in the previous time step and a predefined pipe diameter.

After the total values at station 4, the diffuser outlet, are known, the initial assumption is made that the total pressure remains constant between the diffuser in- and outlet. The total pressure at station 3 can then be used together with the inlet conditions of the turbine to calculate the total temperature at station 3, the rotor outlet. From that the total enthalpy difference across the expander or specific isentropic work $w_{isen}$ can be found. Next, $w_{isen}$ is used with the assumed flow and work coefficients, $\psi$ and $\phi$, to determine the rotor tip speed $u_2$ and all the velocity components and flow angles of the rotor and stator of the turbine as can be seen in Figure 4.9.

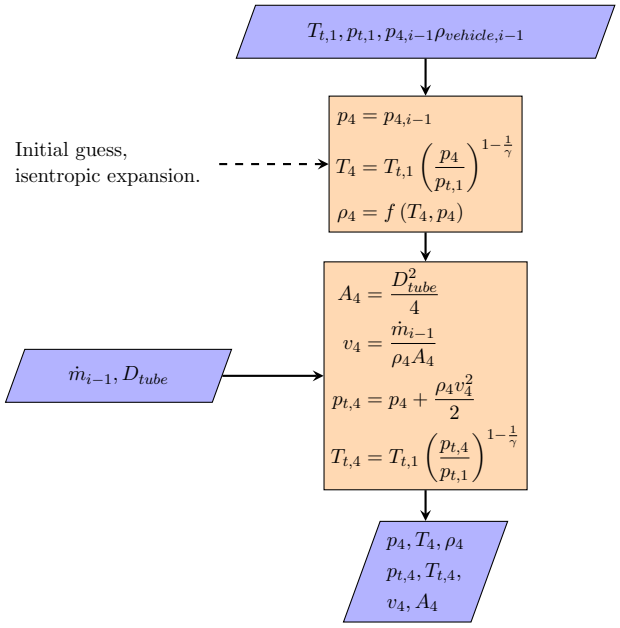


*Figure 4.8: Initial calculation procedure of the gas conditions at the turbine outlet, assuming isentropic efficiency values for the turbine.*

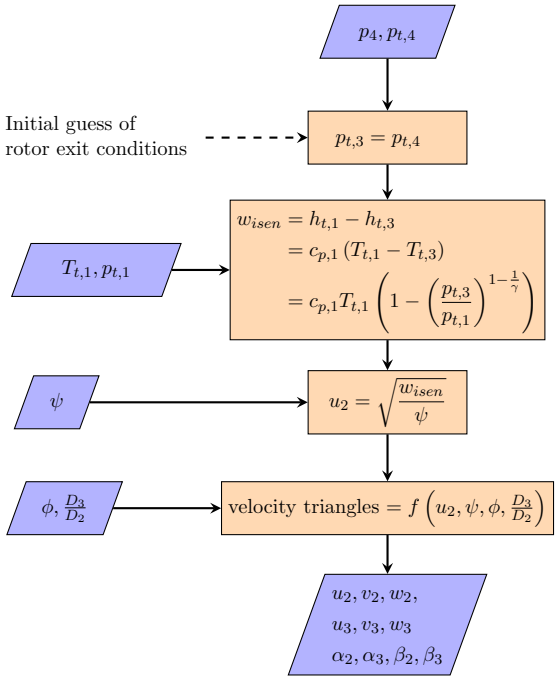


*Figure 4.9: Calculation procedure of the 1D turbine design parameters (velocity components and flow angles) based on the expansion ratio and assumed work and flow coefficients.*

After the velocity components of the turbine are known, the model continues with calculating the conditions at station 2, between the stator and rotor. In order to do so, a first guess is made for the density at this station by assuming the gas density to be equal to that at station 1, the turbine inlet. Next, the pressure at station 2 is calculated from total pressure, assumed density and flow velocity. This can be used in combination with an assumed isentropic stator efficiency to calculate the temperature and an updated density can be calculated from the pressure and temperature. The variables are considered if this updated density matches the assumed density close enough. If not, the newly calculated value for the gas density is used as a new guess and the calculation is iterated until convergence as shown in Figure 4.10.

In order to start the calculation steps of station 3, the rotor outlet, the conservation of rothalpy is considered as shown in figures 4.11 and 4.12. For this step, it is important to note that the total enthalpy $h_t$ is considered to stay constant over the stator.

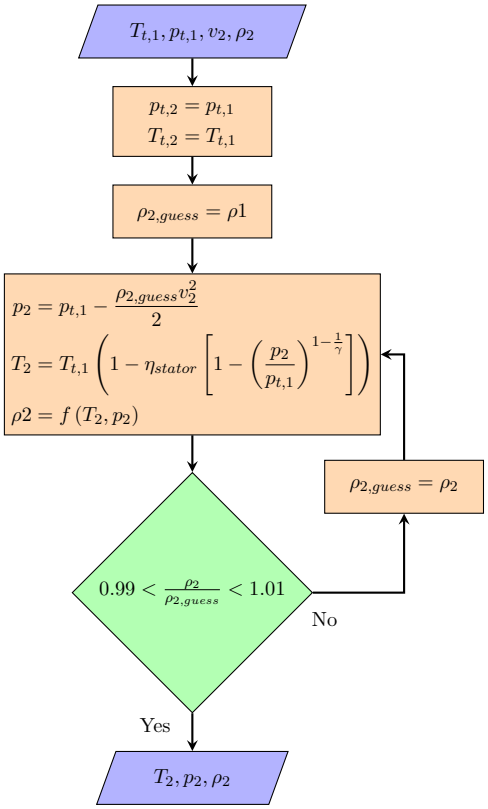


*Figure 4.10: Calculation procedure of the flow properties between the stator and rotor vanes.*

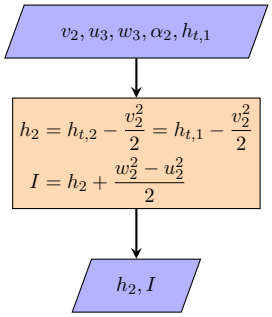


*Figure 4.11: Calculation procedure of the enthalpy and rothalpy of the turbine.*

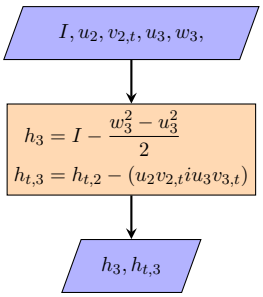


*Figure 4.12: Calculation procedure of the enthalpy and rothalpy of the turbine.*

For the rotor outlet conditions at station 3, a similar procedure can be followed as for station 2. An initial guess for the density at station 3 is made, which, together with the flow velocity and total pressure, are used to calculate the pressure. The temperature follows from the pressure ratio over the rotor and an assumed rotor efficiency. The density is recalculated using FluidProp, leading to an updated total pressure at station 3, which was previously assumed as shown inFigure 5.4. These values are then used in an iteration loop until the density converges, as observed in Figure 4.13.

As shown in Figure 4.14, the total conditions at station 3 can be used to provide updated values of the total conditions at station 4 and the mass flow and pipe diameter can be used to calculate the flow velocity and static conditions.

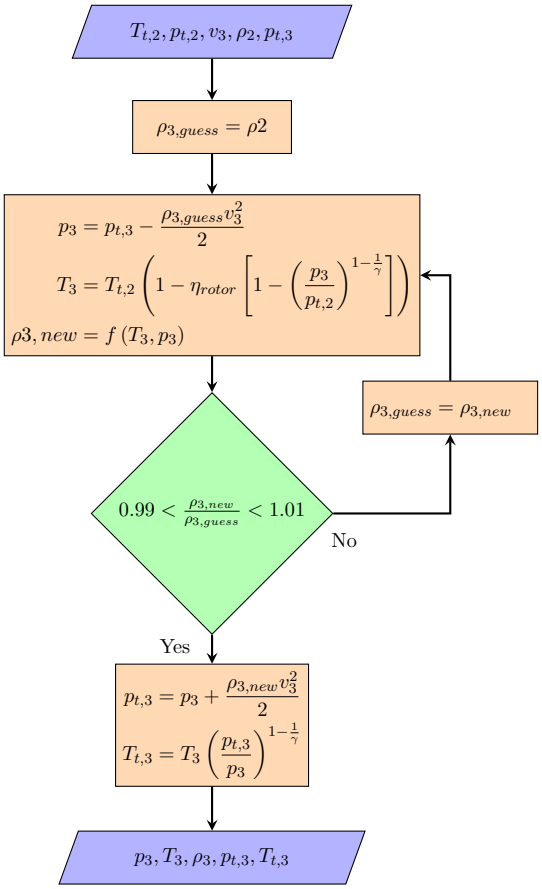


*Figure 4.13: Calculation procedure of the rotor exit conditions.*

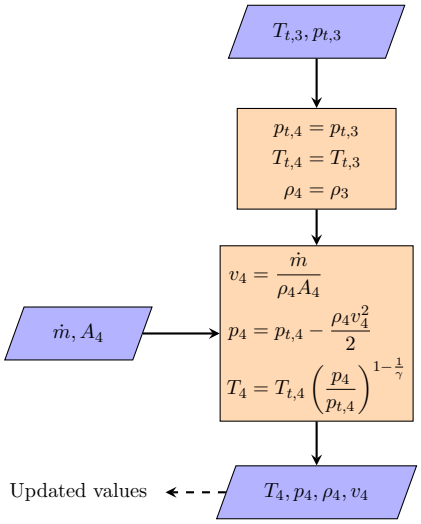


*Figure 4.14: Updated calculation procedure of the turbine exit conditions after the diffuser.*

As the top-level overview explained, the expander also governs the mass flow through the system. In order to operate the system in a way that is as efficient as possible for a turboexpander, a maximum corrected mass flow rate is assumed. When the expansion ratio over either the stator or rotor is higher than the critical expansion ratio of hydrogen, shown in Equation 4.1, the flow is choked, meaning that sonic speed $M = 1$, is reached in the throat of the nozzle area between the blades and that it is physically impossible to achieve a higher flow rate. In this case, the actual mass flow can be calculated from the fixed corrected mass flow and the corresponding throat areas $A^*_{rotor}$ and $A^*_{stator}$ can be calculated. This is shown in the left-hand side of figures 4.15 and 4.16. These throat areas are relevant when the flow is not choked, as seen on the left sides of figures 4.15 and 4.16. In this case, the Mach number can be calculated based on the total-to-static pressure ratio and the mass flow can be found for the fixed throat area and the calculated Mach number. Furthermore, the calculated throat ares will later on be used to define the geometry of the turbine.

$$ER_{crit} = \frac{1}{\left(1 - \frac{\gamma-1}{\gamma+1}\right)^{\frac{\gamma}{\gamma-1}}} \tag{4.1}$$

As both the stator and the rotor could be choked, the model assumes the mass flow of whichever is more limiting.

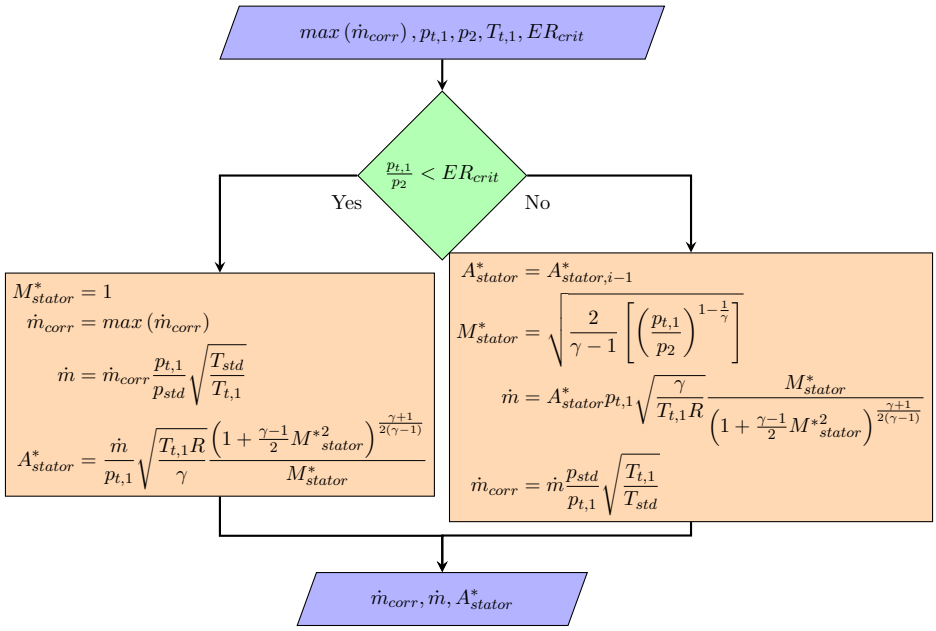


*Figure 4.15: Calculation procedure of the cross-sectional area of the stator nozzle and the mass flow through the system based on critical expansion ratio of hydrogen.*

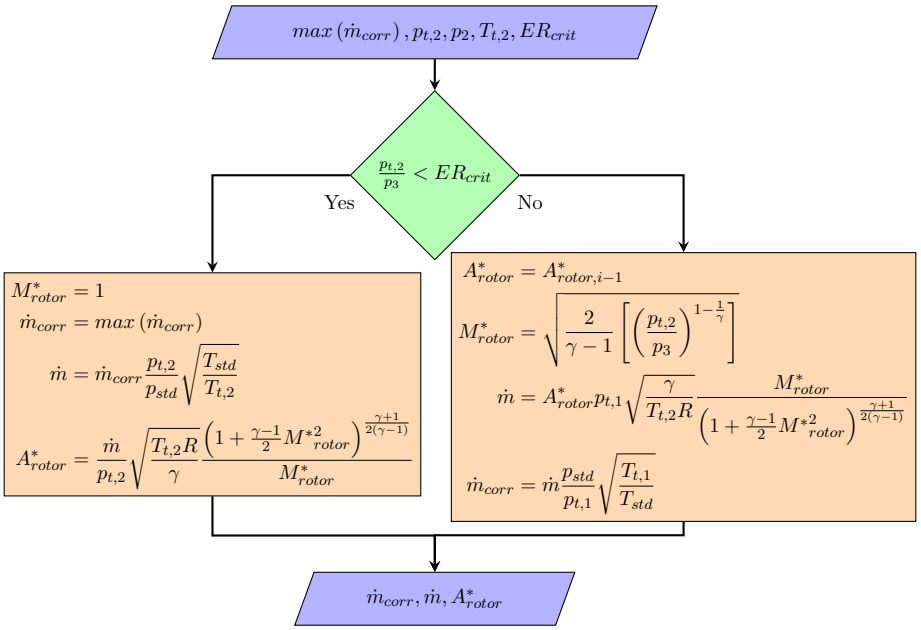


*Figure 4.16: Calculation procedure of the cross-sectional area of the rotor nozzle and the mass flow through the system based on critical expansion ratio of hydrogen.*

### 4.3.5 Chiller and refuelling nozzle

As shown in the top-level overview of the system model, the chiller and refuelling nozzle are considered as one block due to their relatively simple operation given the assumptions made for the model.

Figure 4.17 shows the operation of the chiller in correspondence with SAEJ2601 refuelling protocols. In order to prevent the vehicle tank from overheating, the flow is cooled to typically -33°C or 240.15 K. In the model, this is represented by a simple if-else block. If the flow at station 4, the diffuser outlet, is already below a certain limit, then no additional cooling is required. However, if the temperature in station 4 is higher, it will be cooled to this limit. As the pressure drop in this heat exchanger is significantly higher than pressure losses in normal piping a fixed pressure drop is assumed.

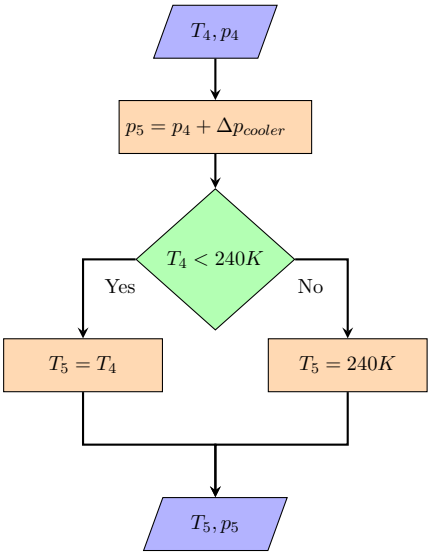


*Figure 4.17: Calculation procedure of pressure and temperature after the pre-cooler based on predefined temperature limits.*

An additional pressure drop is assumed for the dispenser, shown in Figure 4.18. In reality, this would also result in a temperature change but as this would be a fixed system loss it is assumed that this is compensated for in the temperature change in the chiller. This assumption is made for simplicity and to not assume too many system parameters that are not related to the focus of this thesis, the design of an expander for an HRS.

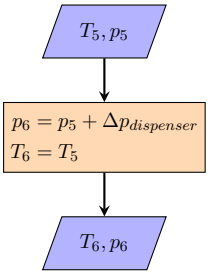


*Figure 4.18: Calculation procedure of the pressure and temperature after the dispenser based on a fixed pressure drop.*

### 4.3.6 Vehicle tank

Finally, the conditions in the vehicle tank are updated. As mass is added to a fixed-volume tank, the tank's density increases, leading to a change in pressure and temperature. However, two distinct mechanisms cause a temperature change in the vehicle tank, which are calculated separately as shown in Figure 4.19. First, a temperature change is introduced by mixing a unit of gas $\dot{m}$ at the outlet temperature of the chiller $T_{6,i}$ from the current time step with the mass that is already present in the tank $m_{7,i-1}$ at its previous temperature $T_{7,i-1}$. The second mechanism that introduces a temperature change is compression in the tank from adding more mass to a fixed volume tank. This is calculated as follows: First, an updated pressure is calculated with FluidProp for the new temperature and density in the tank, leading to a first guess of the compression ratio in the tank from the previous time step to the current one $PR_{7,guess}$. This compression ratio leads to a new temperature $T_{7,i,new}$. However, this temperature change also results in another pressure change. Because of this, a new pressure $p_{7,i,new}$ is calculated which once again leads to a new value for the compression ratio between the previous time step and

the current one. This process is iterated until the time-wise compression ratio converges.

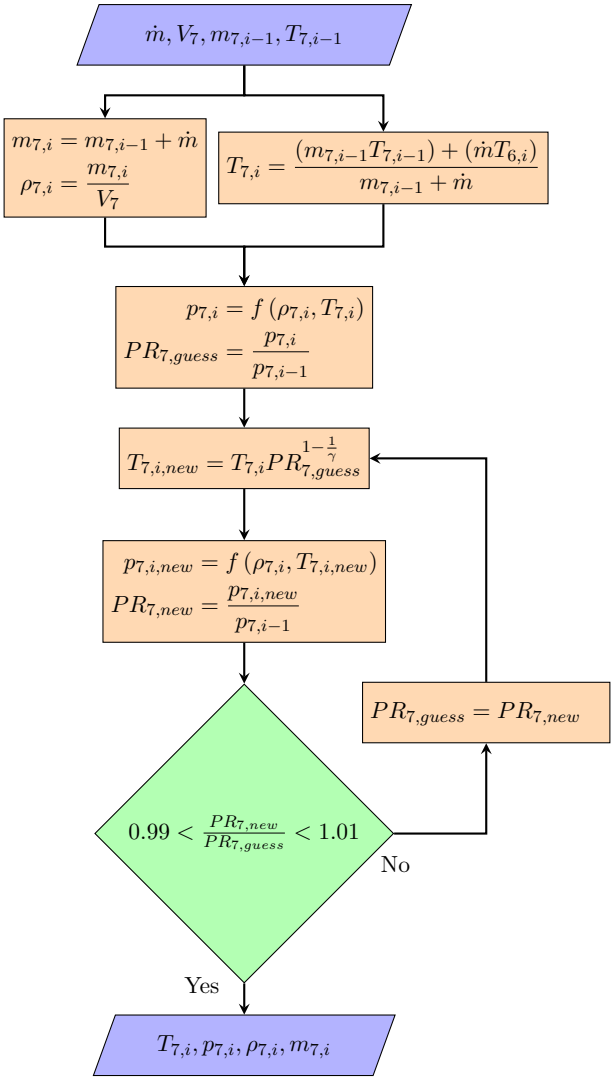


*Figure 4.19: Calculation procedure of pressure, temperature, density and mass in the vehicle tank.*

# 5 Turbine design

Having established a suitable application in which potential energy can be recovered from compressed hydrogen in the previous chapters, this chapter will cover the selection, design and analysis of a suitable expander for this purpose.

Several different types of expanders were briefly considered during the initial literature study. Examples include screw expanders, scroll expanders, reciprocating piston expanders, tesla turbines and turboexpanders [107]. Attempts were made to draw comparisons between these types of expanders based on their typical applications, operating regimes and design procedures but when compared to the initial estimates of the operating conditions in a refuelling station, none proved to be exceptionally more suitable than others. These initial estimates included a mass flow of 30 - 60 g/s at pressures of 700 bar, expansion ratios of up to 18 and a temperature of 288 K. At these conditions, each initial estimate resulted in extremely small design features and high rotational speeds.

Considering the relative mechanical simplicity, well-understood design methods and the fact that both axial and radial turboexpanders can reach relatively high expansion ratios, these types were regarded as the most suitable to continue with. It should be noted that this decision has also been influenced by the industrial and academic relevance of the choice of expander and the design methods that would be applied. The fact that this thesis pursues a degree in Aerospace Engineering and that the industrial topic provider works in the turbo-machinery industry did aid in the decision-making process. Finally, adding the fact that all three authors of previous literature on the subject, Chen [99], Yoshida [104] and Burgess [102, 103], referred to radial inlet turbines, the qualitative decision had been made to continue with the concept of a radial inlet turbine, taking note that this decision would also be reflected upon in the analysis of the eventual results.

Having established the type of expander that will be used, Section 5.1 will treat the adopted sizing method used in the design process, this method is in part based on the materials presented in "Turbomachinery Fundamentals, Selection and Preliminary Design" by Marco Gambini and Michela Velinni [108] and in part by the lecture materials of the AE4206 Turbomachinery course at TU-Delft, given by Dr. M. Pini [109], which provides a unified design approach based on much more extensive literature such as books by Dixon [110], Schobeiri [111], Korpela [112] and Baskharone [113]. After this, Section 5.2 will cover the methods in which the turbine has been modelled and its performance has been estimated in the 1D model and in the 3D validation case.

## 5.1 Turbine sizing

The following section will cover the turbine sizing method, starting with several initial design assumptions in Subsection 5.1.1, an overview of velocity triangles in Subsection 5.1.2 and finally the complete list of calculations used for the geometric design of the turbine in Subsection 5.1.3.

### 5.1.1 Initial design assumptions

The preliminary design phase of a turbomachine, regardless of its type, is often dictated by some first assumptions that aid the designer in creating a starting point that can then be iterated upon.

Some of these, such as the mass flow, expansion ratio or the expected shaft power, are dictated by the system in which the expander needs to operate. In this case, the system model provides an input for both the mass flow and the expansion ratio, whereas the shaft power, or the eventually recovered energy, is to be analyzed. However, in order to start the design procedure, an estimate of the isentropic work is required, which can be obtained through the temperature difference across the expander and assumed isentropic efficiencies for the stator and rotor of the turbine as shown in Figure 4.9.

In the system model, the mass flow is dependent on the corrected mass flow rate $\dot{m}_{corr}$. As shown in Equation 5.1, the corrected mass flow rate represents the mass flow rate independent of pressure and temperature. The corrected mass flow is typically used to standardise the performance maps of a compressor or turbine so that one graph can depict the performance in a wide range of operating conditions [114]. This is especially relevant for the application in an HRS as both the in and outlet conditions change continuously throughout the refuelling process. Because of this, a fixed corrected mass flow rate has been adopted as an input to the system model.

The expansion ratio, $ER_{tt}$, is simply the ratio between the in- and outlet pressures of the expander as shown in Equation 5.2.

$$\dot{m}_{corr} = \dot{m} \frac{\sqrt{\frac{T_t}{T_{std}}}}{\frac{p_t}{p_{std}}} \tag{5.1}$$

$$ER_{tt,turb} = \frac{p_{t,1}}{p_{t,3}} \tag{5.2}$$

The next step in the initial design is to obtain an estimate for the so-called duty coefficients. These are the flow coefficient $\phi$ and the work coefficient $\psi$ which can be used to relate the estimated isentropic work of the expander to the tip speed of the rotor and the velocity components as will be detailed in Subsection 5.1.2. These coefficients are two non-dimensional parameters that can be used to analyse differences between turbines or base designs on others with slight modifications.

If they are used to initialise a design instead of comparing an existing one, initial estimates can be obtained through design charts such as the ones from Baljé [106] or Chen and Baines [115].

In "Turbomachines: A Guide to Design, Selection and Theory" [106], Dr. O.E. Baljé provides a unified comparison method between turbomachines of various sizes and types. An example chart for turboexpanders can be seen in Figure 5.1. These charts relate the achieved efficiency of various types of expanders to two non-dimensional parameters, the specific speed $N_s$ and the specific diameter $D_s$ as shown in Equation 5.1.1 and Equation 5.1.1.

$$N_s = \frac{N\dot{V}^{1/2}}{(w_{isen})^{3/4}} \tag{5.3}$$

$$D_s = \frac{D\,(w_{isen})^{1/4}}{\dot{V}^{1/2}} \tag{5.4}$$

Together, the specific speed and diameter can be related to the duty coefficients $\phi$ and $\psi$ following Equation 5.1.1 and Equation 5.1.1:

$$\Phi = \frac{1}{D_s^3 N_s} \tag{5.5}$$

$$\Psi = \frac{1}{D_2^2 N_s^2} \tag{5.6}$$

However, it should be noted that these charts from Baljé are based on a performance comparison

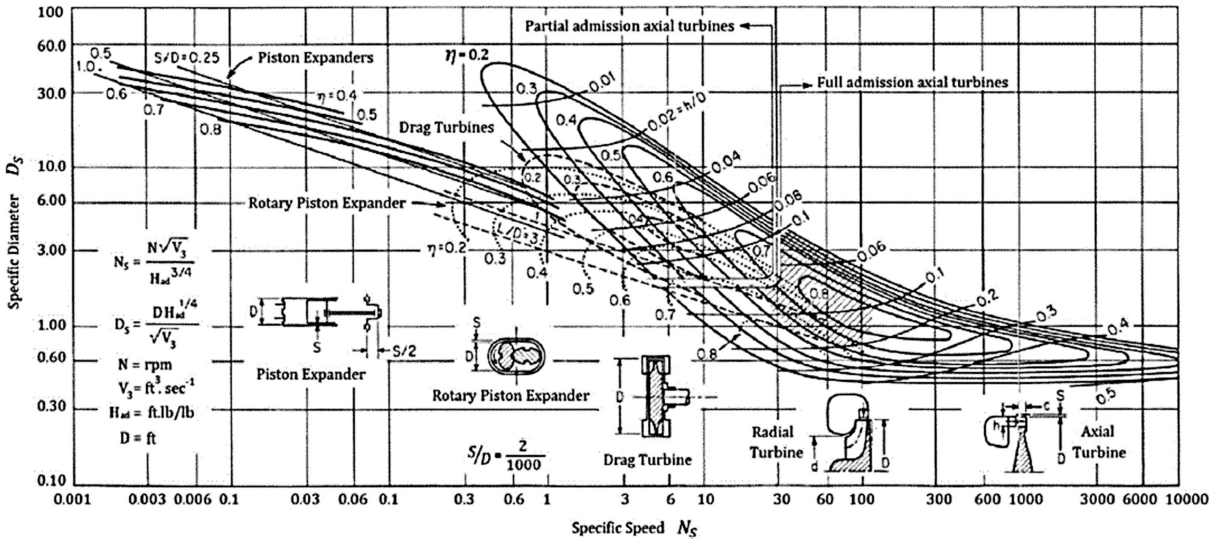


*Figure 5.1: Performances of several expander devices, Baljé 1981 [106].*

study between existing turbomachine designs from before 1981. Considering the extremely high pressures and relatively low temperatures in an HRS combined with the fact that the properties of hydrogen are vastly different than those of the gasses typically used in automotive or industrial turbines, some caution should be taken before adopting initial parameters for this application from the Baljé charts. Instead, a more recent alternative from 1994 can be found in charts developed by H. Chen and N. C. Baines as shown in Figure 5.2 [115].

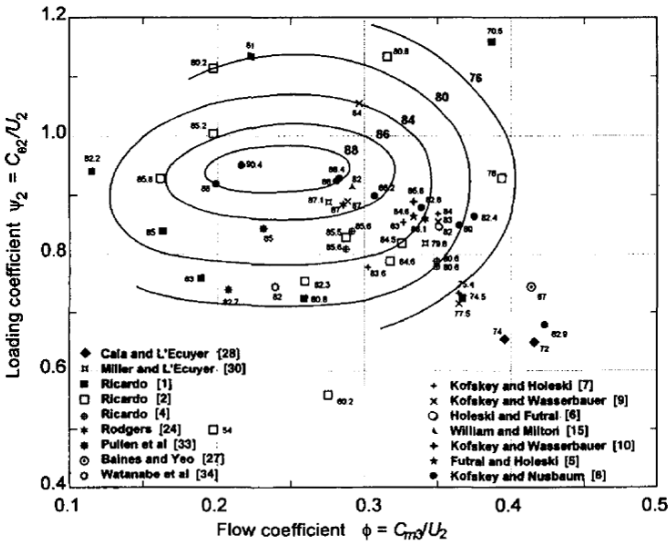


*Figure 5.2: Performances comparison of several radial inlet turbines, Chen and Baines 1994 [115].*

Similar to the Baljé diagram, this chart relates turbine efficiency to its flow and work coefficient based on data from a number of analysed turbines, in the case of Figure 5.2, specifically radial inlet turbines. Although still based on turbine performance data from 1994 for applications vastly different than an HRS, the thesis supervisor Dr. M. Pini suggested using this chart based on the results of his own research on unified design methods and performance predictions of turbo-machinery in novel applications.

As shown in Figure 5.2, the chart suggests an optimal efficiency for a flow coefficient $\Phi = 0.245$ and a work coefficient $\Psi = 0.94$.

### 5.1.2 Velocity triangles

After having estimated or determined the duty coefficients, these can be combined to generate a first estimation of velocity triangles. Velocity triangles are typically used to visualise tangential and meridional components of the absolute and relative velocity vectors as shown in Figure 5.3.

In accordance with the definition of station numbers in Subsection 4.3.2, subscript 2 depicts the station between the stator vanes and the rotor vanes. Similarly, station 3 refers to the exit of the turbine rotor. $u_2$ and $u_3$ refer to the tip speed at the relative stations, $v$ refers to the absolute velocity in a stationary reference frame and $w$ refers to the velocity relative to the rotor. The angles $\alpha$ and $\beta$ refer to the angles between the meridional plane of the turbine of the velocities for $v$ and $w$ respectively. A positive value denotes that the respective velocity is in the direction of the rotation of the turbine.

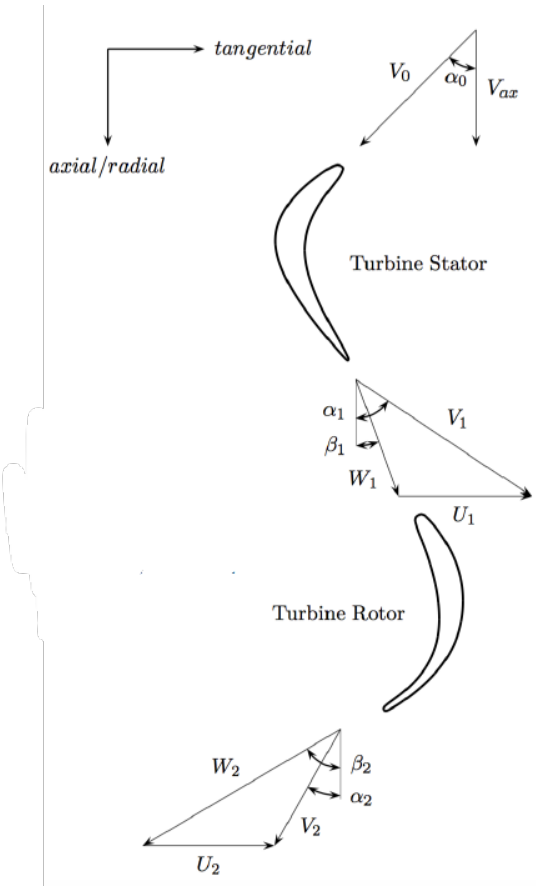


*Figure 5.3: Definition of the flow angles and velocity components in a turboexpander [109].*

In order to initialise the calculations of the velocity components, first, the tip speed needs to be found using Equation 5.7, previously shown in Figure 4.9. Once $u_2$ has been determined, the procedure shown in Figure 5.4 can be used. First, an assumed diameter ratio $\frac{D_2}{D_3}$ is used to determine the tip speed at the rotor exit after which Equation 5.8 and Equation 5.9 can be used to determine the meridional and tangential components of the absolute velocity at station 2, $v_2$. Using some basic trigonometry, these velocity components and the tip speed lead to the relative velocity components at station 2, $w_2$.

$$u_2 = \sqrt{\frac{w_{isen}}{\Psi}} \qquad (5.7) \qquad v_{2m} = u_2\Phi \qquad (5.8) \qquad v_{2t} = u_2\Psi \qquad (5.9)$$

Next, an assumed value of the absolute outflow angle of the rotor needs to be assumed. Typically, a no-swirl exit condition is assumed for an initial design, meaning that $\alpha_3$ equals zero. This is an assumption that can later be iterated upon. Combined with the assumption that the meridional velocity component stays constant through the turbine passage, $v_{2m} = v_{3m}$, this results in all the components of the absolute and relative velocities at station 3, $v_3$ and $w_3$. Finally, these velocity components can be used to calculate the flow angles which will serve as an initial guess for the shape of the turbine blades.

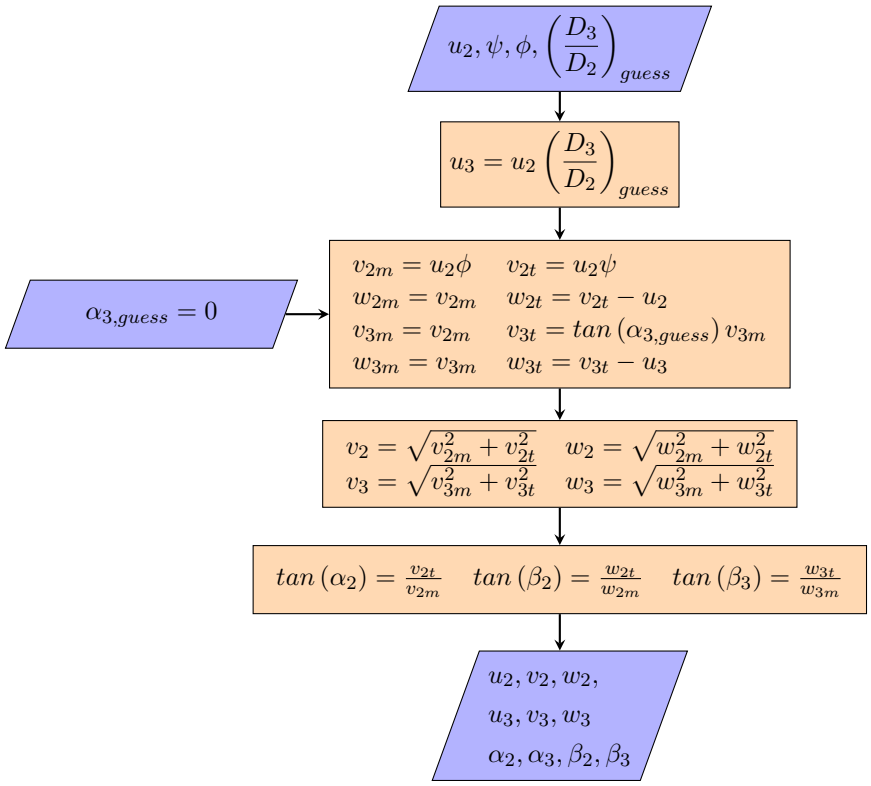


*Figure 5.4: Detailed calculation procedure of the velocity components and flow angles of the stator and rotor of the turbine.*

### 5.1.3 Geometrical design

Once the velocity components and the flow angles are known, these can be used in conjunction with information on the operating condition to define a geometric design of the turbine as shown in Figure 5.5. These calculations are a combination of the design method presented in the AE4206 course on Turbomachinery from Dr. M. Pini [109] and the work by Gambini [108].

First, the rotor tip speed and rpm values can be used to determine the rotor inlet diameter $D_2$. The tip speed is a result of the calculated isentropic work and the assumed work coefficient as shown in Equation 5.7. The rpm is a predetermined parameter used to bound the design space as will be explained in Section 5.2. Next, knowledge of the mass flow, gas density and meridional velocity at station 2 can be used to determine the total inflow area of the rotor $A_2$. Which in turn leads to the blade height at the rotor inlet.

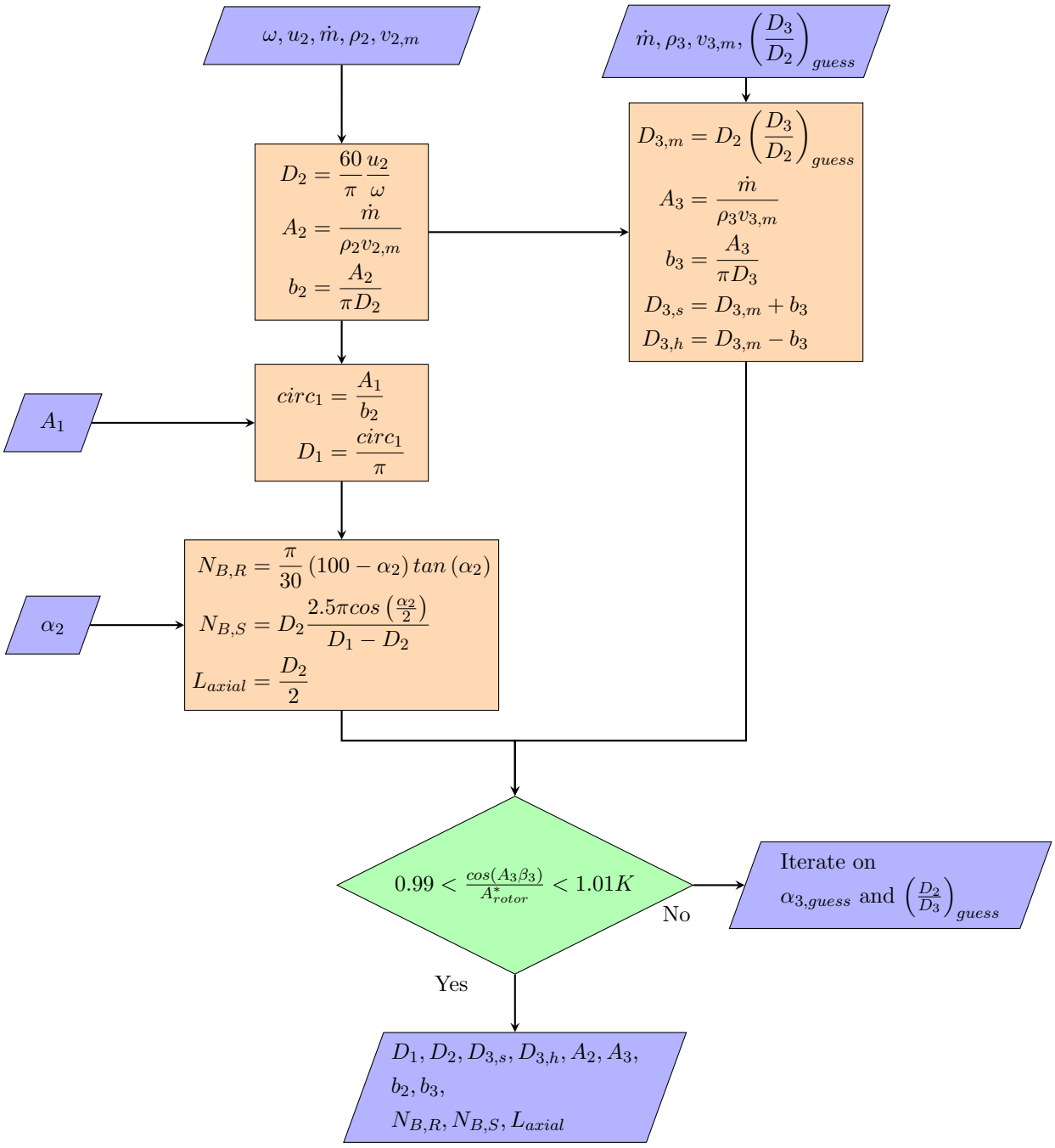


*Figure 5.5: Calculation procedure of the geometrical features of the turbine design.*

For station 3, the rotor outlet, the mean diameter $D_{3,m}$ can be found using a predetermined diameter ratio and the rotor inlet diameter $D_2$. The outflow area and blade height can be found in a similar manner to those at the rotor inlet and finally, the blade height can be used to determine the hub and shroud diameters at the rotor outlet.

For station 1, the stator inlet, a circumference and diameter can be found by assuming that the blade height of the stator vanes remains constant and that the total inflow area is equal to that of the piping between the buffer tanks and the expander inlet.

The number of stator and rotor blades can be calculated using empirical relations. Similarly, the axial length of the turbine would typically defined by an empirical relation $L_{axial} = \frac{D_2}{2}$.

However, as the results will show, the produced geometry is far from "standard" and instead, the axial length has been set to the rounded value of $L_{axial} = \frac{D_2 - D_{3,m}}{2}$.

Furthermore, the geometry provides an outlet area normal to the axial direction. This can be combined with the outflow angle and possibly the blade thickness to find the outflow area normal to the flow direction. However, for the initial guesses of $\alpha_3 = 0$ and $\frac{D_2}{D_3}$, this relative outflow area does not match with the throat that was found in the system model when calculating the mass flow. In order to match the geometric design of the turbine with the mass flow calculations, we can manually iterate on these variables. To try and preserve the "optimal design logic", initial attempts only changed the diameter ratio and kept the absolute outflow angle $\alpha_3$ at 0°. However, this did not result in a feasible design and thus both the diameter ratio and the outflow angle have been iterated, the final values will be presented in the results section.

## 5.2 Turbine model

This section refers to how the turbine design has been modelled. Subsection 5.2.1 will first cover the 1D turbine model integrated into the system model which analyses the performance of various turbine designs across the entire refuelling cycle based on adopted loss models. Next, Subsection 5.2.2 provides an overview of the 3D modelling and simulation of one selected turbine design in Ansys.

### 5.2.1 1D turbine model

As covered in Chapter 4, the system model calculates all the variables in the system and across the expander for every one-second interval of the refuelling cycle. Next, at every one of these time steps, state variables such as the mass flow $\dot{m}$ and expansion ratio $\frac{p_1}{p_3}$ are used in combination with assumed design parameters such as the flow and work coefficients $\Phi$ and $\Psi$ to provide an optimal 1D design for that time step, represented by the velocity triangles and geometric design features covered in Section 5.1. For a refuelling cycle of n time steps, this thus leads to n different turbine designs, each representing a quasi-optimal design for the time step that they have been designed for. In turn, loss models can be used to evaluate the performance of each of these designs over the entire duration of the refuelling cycle, leading to a performance curve for each design which can finally be used to select the most optimal design and its associated design point.

#### 5.2.1.1 Design variables

The term quasi-optimal is used here as not all assumed design parameters reflect an optimal design decision. Indeed, the selected values of the duty coefficients $\Phi$ and $\Psi$ reflect a design for optimal efficiency, but two other variables, the tip speed $u_2$ and the design rpm do not.

As shown in Figure 5.4, the tip speed and rpm are used to determine the rotor diameter $D_2$, which serves as a base for all other geometrical features of the turbine design. Following Equation 5.7, the calculated tip speed is a result of the turbine's specific isentropic work, which varies over time as the expansion ratio varies. The rpm on the other hand is a design parameter that needs to be assumed to close the design problem, typically based on a maximum achievable or desirable rotational speed of the generator or other system components.

Assuming a single maximum rotational speed value, each potential design with its optimal tip

speed would result in a unique rotor diameter. A challenge arises when all of these designs are later analysed over the entire refuelling process instead of only at their respective design points as, when operated at higher tip speeds, these would then lead to higher rotational speeds than the predefined maximum rpm.

In order to work around this, each design is initialised by calculating the rotor diameter based on the maximum allowed rpm and the maximum tip speed which is calculated during the entire refuelling process as shown in Equation 5.10. In practice, this results in a fixed rotor diameter for each turbine design based on the maximum expansion ratio in the refuelling process and the maximum rpm.

It is in this sense that the 1D design can be considered quasi-optimal. For the given bounding parameter of a defined maximum rpm - leading to a certain fixed rotor diameter - each time step results in an optimal efficiency blade design for its respective operating condition. Finally, each of these designs can be evaluated over the entire refuelling cycle using loss models to calculate its losses and efficiency.

$$D_2 = \frac{60}{\pi} U_{2,max} \omega_{max} \tag{5.10}$$

#### 5.2.1.2 Loss models

In order to predict the efficiency of each turbine design beyond the assumed isentropic efficiency, several loss models have been adopted for the 1D analysis of each turbine design across the entire refuelling cycle. The adopted loss models are all sourced from "Turbomachinery Fundamentals, Selection and Preliminary Design" by Gambini [108] which extensively compared loss models from different authors.

The exact choice of the adopted loss models has been performed rather qualitatively. This choice is partially based on the known parameters of the system as there is no use in adopting a loss model for which half of the parameters are unknown. Otherwise, the perceived simplicity of a model or its equations has also been taken into account. After all, an HRS is quite a novel application and as the results will show, the final design is quite unconventional. Hence, relations based on empirical constants might not be as applicable as they would be for more common applications such as gas turbines or turbochargers. Simpler equations based on geometrical features or physical variables of the flow would be more suitable and are therefore preferred.

For the stator, only the passage losses have been considered. For the rotor, the passage losses have been considered, as well as the incidence losses, trailing edge losses, rotor clearance losses, windage losses and dynamic losses.

**Stator passage losses**
As presented in the book from Gambini [108], the use of estimating stator losses is disputable due to their relatively small contribution when compared to rotor losses. However, as the final design will show, the calculated stator inlet diameter $D_1$ is rather large with respect to the rotor inlet diameter $D_2$, resulting in quite a long stator passage. Combined with a rather small blade height $b_2$ this results in a large ratio between the wetted area in the stator and the volume of the passage. Because of this, the choice has been made to adopt a stator passage loss model nonetheless.

The stator loss model, shown in Equation 5.11 has been proposed by several authors (Rodgers

[116], Gosh et al. [117], Deng et al. [118] and Meroni et al. [119]) and is mainly dependent on the geometrical features of the stator vanes such as the blade pitch $S_S$ in Equation 5.12, an estimation of the stator chord length $C_S$ in Equation 5.13, the velocity at the stator exit $v_2$ and the Reynolds number in the passage $Re_2$ in Equation 5.14.

$$\Delta h_{S,passage} = \frac{v_2^2}{2} \frac{0.05}{Re_2^{0.2}} \left[ \frac{3\ tan\left(\alpha_2\right)}{\frac{S_S}{C_S}} + \frac{S_S}{b_2} cos\left(\alpha_2\right) \right] \tag{5.11}$$

$$S_S = \frac{\pi D_1}{N_{B,S}} \tag{5.12}$$

$$C_S = \frac{D_1 - D_2}{2} \frac{1}{cos\left(\frac{\alpha_1}{2}\right)} \tag{5.13}$$

$$Re_2 = \frac{\rho_2 v_2 b_2}{\mu_2} \tag{5.14}$$

**Rotor passage losses**
For the rotor passage losses, many loss models exist, several of which are presented and evaluated in the work by Gambini [108]. However, as almost all of these rely on the estimation of friction coefficients which are beyond the current scope of the design, the choice has been made to adopt the model seen in Equation 5.15 as proposed by Wasserbauer and Glassman [120]. This relation includes the coefficient $K$, which can be assumed to equal 0.3 and is for the rest based on the difference between the incidence angle and a calculated optimal incidence angle and the relative outlet velocity of the rotor.

$$\Delta h_{R,passage} = \frac{K}{2} \left[ w_2^2 cos^2\left(\beta_2 - \beta_{2,opt}\right) + w_3^2 \right] \tag{5.15}$$

$$\beta_{2,opt} = tan^{-1}\left( \frac{-u_2}{v_{2m}} \frac{1.98}{N_{B,R}} \right) \tag{5.16}$$

**Rotor incidence losses**
Similarly, the incidence losses are also estimated through an equation (Equation 5.17) proposed by Wasserbauer and Glassman [120].

$$\Delta h_{R,incidence} = \frac{w_2^2}{2} sin^2\left(\beta_2 - \beta_{2,opt}\right) \tag{5.17}$$

**Rotor trailing edge losses**
The rotor trailing edge losses are based on an equation proposed by Qi et al. [121], which presents a simplified model of a more extensive equation by Glassman [122]. In this model, the trailing edge blade thickness is approximated based on a fraction of the rotor diameter as shown in Equation 5.19.

$$\Delta h_{R,TE} = \frac{w_3^2}{2} \left( \frac{N_{B,R} t_{TE}}{\pi D_3 cos\left(\beta_3\right)} \right)^2 \tag{5.18}$$

$$t_{TE} = 0.01 D_2 \tag{5.19}$$

**Rotor clearance losses**
The rotor clearance losses are approximated by Equation 5.20 as proposed by Baines [123].

This equation assumes some fixed coefficients: $K_a = 0.4$, $K_r = 0.75$ and $K_{a,r} = -0.3$ and the parameters $C_a$ and $C_r$ as defined by Equation 5.21 and Equation 5.22. Furthermore, the axial and radial rotor clearances are represented by $\tau_a$ and $\tau_r$. Gambini [108] recommends the clearance to be between 2% and 5% of the rotor inlet blade height $b_2$ but not lower than 0.3 mm. However, this limit is based on more traditional applications and might be re-assessed for the current application. Instead, Jiang et a. [124] referred to achievable clearances of 50$\mu$m for micro air turbines of similar size to what will pe presented in the results of this study.

$$\Delta h_{R,clearance} = \frac{u_2^3 N_{B,R}}{8\pi}\left(K_a \tau_a C_a + K_r \tau_r C_r + K_{a,r}\sqrt{\tau_a C_a \tau_r C_r}\right) \tag{5.20}$$

$$C_a = \frac{1 - \frac{D_{3,s}}{D_2}}{v_{2m} b_2} \tag{5.21}$$

$$C_r = \frac{2D_{3,s}}{D_2}\frac{L_{axial} - b_2}{v_{2m} D_{3,m} b_3} \tag{5.22}$$

**Windage losses**
The windage losses can be represented by the relation shown in Equation 5.23 and are mainly dependent on the mass flow $\dot{m}$, the average gas density across the rotor $\bar{\rho}$, the tip speed at station 2 $u_2$ and a coefficient $K_f$ which is dependent on the Reynolds number and the clearance of the backface of the rotor disk following equations 5.24, 5.26 and 5.27.

$$\Delta h_{R,windage} = \frac{K_f \bar{\rho} u_2^3 D_2^2}{16\dot{m}} \tag{5.23}$$

$$Re = \frac{\rho_2 u_2 \frac{D_2}{2}}{\mu_2} \tag{5.24}$$

$$\bar{\rho} = \frac{\rho_2 + \rho_3}{2} \tag{5.25}$$

$$K_f = \frac{3.7\left(2\frac{\tau_d}{D_2}\right)^{0.1}}{Rr^{0.5}} \quad if\ Re\ <\ 10^5 \tag{5.26}$$

$$K_f = \frac{0.102\left(2\frac{\tau_d}{D_2}\right)^{0.2}}{Rr^{0.2}} \quad if\ Re\ >\ 10^5 \tag{5.27}$$

**Rotor dynamic losses**
Finally, the dynamic losses are equal to the flow's remaining kinetic energy after the expander's last stage as shown in Equation 5.28. It should be noted that these should only be taken into account when calculating the total to static efficiency.

$$\Delta h_{R,dynamic} = \frac{v_3^2}{2} \tag{5.28}$$

#### 5.2.1.3 Selecting the design point

As described at the start of this section, the initial model assumes a total-to-static rotor and stator efficiency together with some assumed optimal design parameters. When applied to the entire refuelling cycle, these lead to a quasi-optimal design for each evaluated time step in the refuelling cycle. But, the performance of these designs is only known or estimated at the operating conditions of their design point. However, as there can only be a single turbine that needs to operate at all points of the refuelling cycle, the efficiencies should also be calculated in off-design conditions of each of these designs. This is done through the above-mentioned loss models. As these are dependent on both the geometrical features of the turbine design and the

operating conditions of the system, they allow us to evaluate the losses of each potential turbine design for every single time step.

In doing so, the total losses of each design can be evaluated as shown in equations 5.29 through 5.35. The results can be used to determine which turbine design has the highest overall efficiency and at which point the peak efficiency is reached.

And of course, the total-to-static efficiencies that are initially assumed should be matched with these results to properly reflect on the dynamics of the refuelling process. This is done through a manual iteration process.

Finally, the design that leads to the overall highest efficiency will be used to construct a 3D model in Ansys, and its point of highest efficiency shall be used as the operating point.

$$\Delta h_S = \Delta h_{S,passage} \tag{5.29}$$

$$\Delta h_R = \Delta h_{R,passage} + \Delta h_{R,incidence} + \Delta h_{R,TE} + \Delta h_{R,clearance} + \Delta h_{R,windage} \tag{5.30}$$

$$\eta_{ts,expander} = \frac{h_{t,1} - (h_{s,3,isen} + \Delta h_S + \Delta h_R)}{h_{t,1} - h_{s,3,isen}} \tag{5.31}$$

$$\eta_{tt,expander} = \frac{h_{t,1} - (h_{t,3,isen} + \Delta h_S + \Delta h_R)}{h_{t,1} - h_{t,3,isen}} \tag{5.32}$$

$$\eta_{ts,rotor} = \frac{h_{t,2} - (h_{s,3,isen} + \Delta h_R)}{h_{t,2} - h_{s,3,isen}} \tag{5.33}$$

$$\eta_{tt,rotor} = \frac{h_{t,2} - (h_{t,3,isen} + \Delta h_R)}{h_{t,2} - h_{t,3,isen}} \tag{5.34}$$

$$\eta_{ts,stator} = \frac{h_{t,1} - (h_{s,1,isen} + \Delta h_S)}{h_{t,1} - h_{s,2,isen}} \tag{5.35}$$

### 5.2.2 3D turbine simulation

Finally, the most efficient design that is found in the 1D model is used as a basis to build a 3D model. This 3D model will be used to perform 3D simulations at the selected operating point to potentially validate the results of the 1D model. This model can also be used to analyse how the flow behaves throughout the rotor passage, potentially providing suggestions for future design iterations. Only the rotor of the turbine shall be modelled for this analysis.

It should also be noted that developing the 3D simulation has been done in close collaboration with Alexander Lautenschlager, the industrial supervisor from AYED-ENGINEERING GmbH, who provided guidance on implementing the correct boundary conditions, the implementation of the real gas model and the interpretation of the results.

As shown in Figure 5.6, the workflow in Ansys consists of three distinct blocks: BladeGen, TurboGrid and CFX.

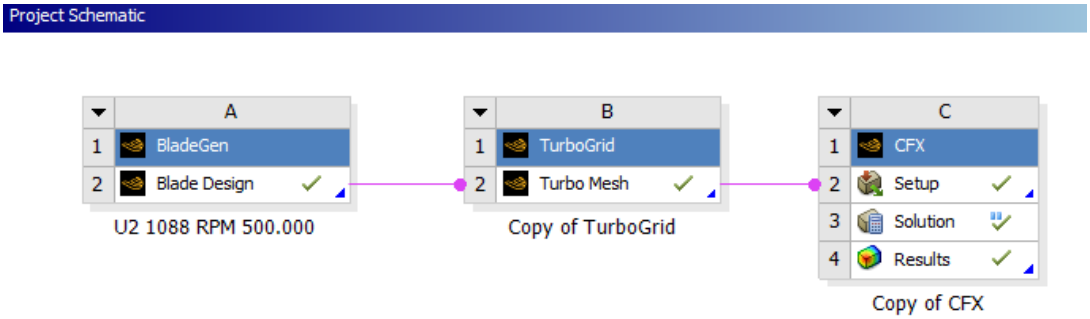


*Figure 5.6: A screen capture of the adopted workflow in Ansys.*

#### 5.2.2.1 BladeGen:

The first block, BladeGen, defines the geometry of the turbine rotor. First, the overall size of the rotor is defined by the rotor in- and outlet diameters $D_2$, $D_{3,h}$ and $D_{3,s}$ as well as the axial length $L_a$, the rotor blade heights $b_2$ and $b_3$ and the blade thickness $t_{TE}$. In the second step, the blade angle can be adjusted according to $\beta_2$ and $\beta_3$. In order to achieve a suitable result, a spline can be manually defined between the rotor in- and outlet to ensure a smooth blade profile. In this case this has been achieved by defining the transition between the rotor in and outlet angle as a smooth spline. In BladeGen, the curvature of this spline is matched to the twist angle - how much the rotor blade wraps around the hub in the tangential direction. This twist angle has a large impact on the relative outflow area of the rotor which can be observed in one of the panes of BladeGen. It has also been assumed that the blade profile remains constant over the height of the blade such that the root and tip profiles are equal.

In order to assist with the in- and outflow domains of the model, in- and outflow volumes have also been defined, which are in practice larger than the gap between the stator and the rotor inlet or the rotor outlet and the diffuser. This does lead to a rotor inlet diameter that is a few millimetres larger than what results form the 1D model. The exact values are provided in the results section.

#### 5.2.2.2 TurboGrid:

The second step is to create a mesh around the defined geometry. This is initialised automatically but adjusted manually to result in a suitable mesh density. Specifically, the area around the blade profile, the hub and the shroud have been altered in an attempt to define a fine enough mesh to capture boundary layer profiles.

#### 5.2.2.3 CFX:

Finally, CFX is used to define the boundary conditions, fluid information and the to-be-analysed variables, which can then be used to run, monitor and analyse a simulation. Each of the relevant settings will be defined in the following paragraphs. First, the boundary conditions in the turbine and pipe domains will be covered, followed by the initial conditions of the simulation

and the definition of the hydrogen gas model that is used in Ansys. After this, some details of the settings used in the solution block will be presented, followed by a short description of the CFX results block.

**Boundary Conditions - Turbine**
The turbine domain around the rotor has been defined as a rotating domain, set to a defined rotational speed matching the design point. It also assumes a 0 Pa reference pressure and a non-buoyant buoyancy model. The heat transfer option is set to "Total Energy" and the Turbulence model to "Shear Stress Transport" also known as an SST model, a specific type of a RANS model (Reynolds Averaged Navier-Stokes).

Within the rotor domain, the boundary type of the inlet is defined as "Inlet". The sides of the domain have been defined as interface boundaries with the "Conservative Interface Flux" option for the mass and momentum, turbulence and heat transfer options. The turbine blade, hub and shroud surfaces have all been defined as "wall" type boundaries with "no-slip wall" as the option for the mass and momentum setting, "Smooth wall" for the turbulence setting and assuming an adiabatic heat transfer option.

The rotor interfaces with the outlet domain through a mixing plane which assumes a constant total pressure across the mixing plane.

**Boundary Conditions - Pipe**
The pipe domain is a stationary domain representing the outlet volume after the rotor. It is set to the following settings: 0 Pa reference pressure, no buoyancy, stationary domain and no mesh deformation. It also uses "Total energy" for its heat transfer option and "Shear Stress Transport" for its turbulence option. It is initialised automatically with a temperature value to avoid warnings about this. The inner and outer walls are modelled the same as the blade, hub and shroud boundaries in the rotor as no-slip walls with smooth surfaces and adiabatic heat transfer settings. The sides of the domain are equally set as interface boundaries with the "Conservative Interface Flux" for all settings. Finally, the outlet boundary is set as "Outlet".

**Initial conditions**
For the inlet of the rotor, the following variables are prescribed:

- The flow regime is set to subsonic as the turbine is not choked at the modelled point.
- The mass and momentum are set by "The Stationary Frame Total Pressure" which is equal to the total pressure of the 1D model.
- The flow direction is defined by cylindrical velocity components that represent the absolute velocity vector of the 1D model. This ensures that the inlet flow is in the same direction as $\alpha_2$.
- The turbulence option has been set to "medium" with an intensity of 5%.
- The heat transfer option has been set to "Stationary Frame Total Temperature" which is equal to the total temperature from the 1D model.

Similarly, the outlet of the pipe domain has the following variables prescribed as its initial conditions:

- The flow regime is also set to subsonic.
- The mass and momentum are set by the "Average Static Pressure" option, which is set equal to the static pressure at the rotor outlet from the 1D model with a 5% pressure profile blend over the whole outlet.

The exact values of each of these variables are described in the results in Chapter 6.

**Hydrogen gas model in Ansys**
Finally, the to-be-modelled fluid is also defined, which leaves the user with the choice to either define a real gas or assume an ideal gas model. As previously discussed in Section 3.2, hydrogen is not an ideal gas under the considered pressures. but modelling a real gas is also a more computationally expensive option. Due to the lack of relevant literature on modelling a high-pressure hydrogen-fuelled turbine in Ansys CFX, the decision has been made to initially attempt both types and to observe the differences. However, from the initial trials it showed that the difference in computing time was negligible and that the results were quite different but also difficult to compare. because of this, the choice had been made to only continue with the real gas model. For the ideal gas model, the standard ideal gas model for hydrogen in Ansys has been used, which assumes $C_p$ to be 14300 $\frac{J}{kgK}$. For the real gas model, the standard Redlich Kwong model has been adopted, and the behaviour of the specific heat capacity has been defined according to the NASA format option. The detailed properties of each option under these settings are shown in Appendix A.

**CFX Solution**
Next, the conditions defined in the CFX Setup are passed on CFX Solution where some solver settings can be adjusted. The solver was set to use 18/20 processors on a Dell XPS 9530 with the following specifications:

| | |
|---|---|
| Device: | Dell XPS 9530 |
| Processor: | 13th Gen Intel(R) Core(TM) i7-13700H 2.40 GHz |
| RAM: | 16.0 GB |
| Integrated graphics: | Intel(R) Iris(R) Xe Graphics |
| Discrete graphics: | NVIDIA GeForce RTX 4050 Laptop GPU |

*Table 5.1: Device specifications*

Once the simulation is initiated from either initial values or previous solution data, the progress of the simulation can then be monitored by observing the values of a set of defined user variables. The convergence of the simulation has been assessed visually.

**CFX Results**
Finally, the last block allows the user to observe the final results of each variable or expression. These can be either numerical results at a specific location which can be compared directly to the results of the 1D simulation or these can be graphical results, mainly in the format of contour plots on defined planes in the passage. The results chapter and appendix will include several of these plots where the variable is shown on the mid-span surface. These graphical results are particularly useful in visualising how the flow behaves around the blade design at the defined operating point.

# 6 Results and discussion

After the selection of hydrogen refuelling stations as a suitable application in which potential energy can be recovered from compressed hydrogen in Chapter 3, Chapter 4 continued with an in-depth description of refuelling stations, their operation, a literature study on recovering potential energy from compressed hydrogen in an HRS and finally the development of a system model of an HRS. After this, Chapter 5 followed with detailing the design procedures of a suitable expander and a description of the 1D and 3D models used to evaluate its performance in both on- and off-design conditions.

All of this is followed by the results presented in this chapter. First, Section 6.1 will provide an overview of all the input parameters used in both the system model and the turbine design. Next, Section 6.2 will provide an overview of the results of the system model. Specifically how all the variables such as pressure, temperature, density and flow speed evolve at different stations throughout the refuelling process. After this, Section 6.3 will cover the results of the 1D turbine analysis for this refuelling cycle by evaluating all the generated turbine designs, detail which design leads to the overall optimal performance and evaluate its performance over the entire cycle - the off-design conditions. This is followed by Section 6.4 in which the results of the 3D analysis of the turbine design at the design point in Ansys are presented. Both the numerical results and the observed flow behaviour in the turbine rotor will be covered, as well as a comparison with the results of the 1D model.

These sections are followed by Section 6.6, which covers a final assessment of the potential impact of integrating this design in an HRS. Including an overview of the recovered energy in the expander and of the saved energy expense by reducing the cooling requirement of the station, eventually leading to an economical assessment.

Next, Section 6.7 provides a critical assessment of the feasibility of this design and explores the impact of changing several initial assumptions on the design and performance of a turboexpander for an HRS through a sensitivity study.

Finally, Section 6.8 provides a comparison between the achieved results of this study and the very recently published interim report of the study by Post et al. at NREL [102, 103, 125].

## 6.1 Summary of the input parameters to the 1D model

Although several system parameters and design variables have already been touched upon in previous chapters, this section will provide a concrete overview of the final assumed parameters used in the system model and the turbine design.

### 6.1.1 HRS system model parameters

For the properties of hydrogen, the model only assumes two properties by default, the individual gas constant $R$ of hydrogen and the specific heat capacity ratio $\gamma$ as shown in Table 6.1. Although the value of the specific heat capacity ratio does vary with pressure and temperature, it has been assumed as a constant in the system model and the turbine design because of how often it is used in pressure and temperature calculations. In order to reduce the error introduced by this assumption, the adopted value has been determined based on the value of $\gamma$ at 290 K averaged across the pressure range that can be found in the HRS which is also shown

in Figure 6.1. Here it can be observed that the assumed averaged value (Dashed green line) falls well within 1% (Indicated by the green area) of the actual value at $T = 290K$ (Solid green line) for the large majority of the operating range. Other parameters, such as the specific heat capacity at constant pressure $C_p$, which is used to estimate the specific work from the turbine, are calculated in the model at specific stations and conditions using the CoolProp library [126].

| Variable | Symbol | Value | Unit |
|---|---|---|---|
| Individual gas constant | $R$ | 4124 | $\frac{J}{kgK}$ |
| Specific heat capacity ratio | $\gamma$ | 1.415 | – |

*Table 6.1: Assumed constant properties of hydrogen as input to the HRS system model.*

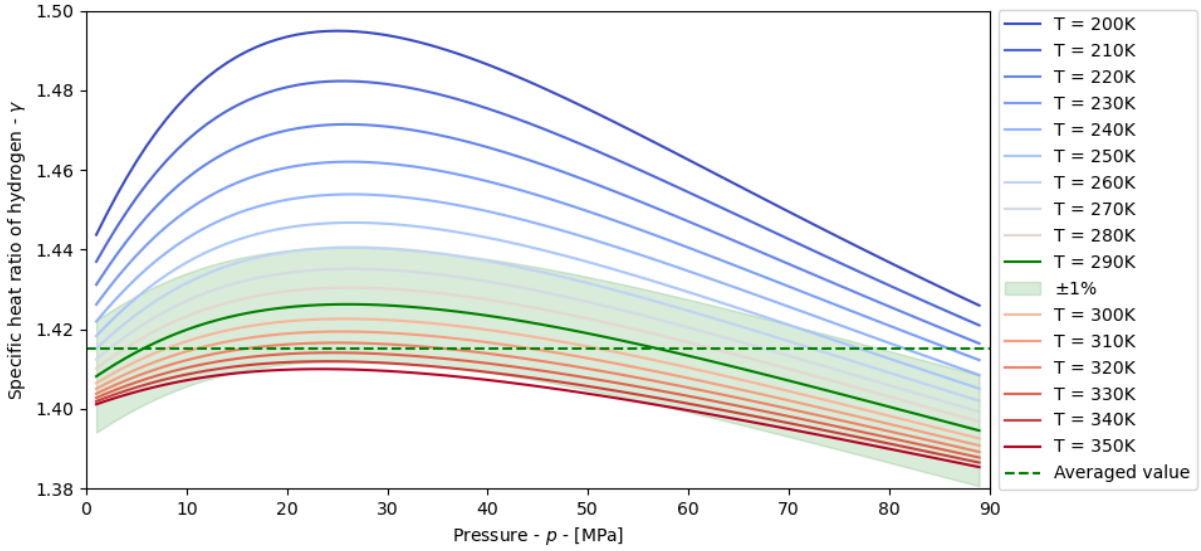


*Figure 6.1: Specific heat ratio of hydrogen over a range of pressures and temperatures, calculated through CoolProp [126].*

Next, several parameters relating to the buffer tanks of the HRS are defined as shown in Table 6.2 these include the initial pressures in and volumes of each of the three buffer tanks. As explained in Subsection 4.3.1, the initial buffer tank pressures were initially based on the results of an optimisation study performed by Xiao et al. [100] but have later been altered to tune the profile of the expansion ratio throughout the refuelling process such that it would be better suited for a turboexpander. The buffer tank volumes have been defined as finite volumes to ensure that the inlet pressure of the expander does in fact change throughout the refuelling process, the exact value has been set at 5 $m^3$. Finally, the tube diameter after the expander has been set following values found in literature [127] and the tube diameter before the expander has been set to match the inlet area of the stator of the expander following empirical design relations as described by Gambini [108].

| Variable | Symbol | Value | Unit |
|---|---|---|---|
| Initial temperature of the buffer tanks | $T_{init}$ | 288.15 | $K$ |
| Low pressure buffer tank - Initial pressure | $p_{LP,init}$ | 25 | $MPa$ |
| Mid pressure buffer tank - Initial pressure | $p_{MP,init}$ | 47 | $MPa$ |
| High pressure buffer tank - Initial pressure | $p_{HP,init}$ | 90 | $MPa$ |
| Low pressure buffer tank - Volume | $V_{LP}$ | 5 | $m^3$ |
| Mid pressure buffer tank - Volume | $V_{MP}$ | 5 | $m^3$ |
| High pressure buffer tank - Volume | $V_{HP}$ | 5 | $m^3$ |
| Tube diameter before expander | $D_{tube,1}$ | 5 | $mm$ |
| Tube diameter after expander | $D_{tube,2}$ | 10 | $mm$ |

*Table 6.2: Initial conditions of the different buffer tanks as input to the HRS system model.*

Several other system parameters are defined in Table 6.3. First, the assumed corrected mass flow rate of the station $\dot{m}_{corr}$, the value of which is tuned to achieve a maximum real mass flow rate of 120 g/s as substantiated by the horizon 2020 research project [128]. Secondly, the assumed isentropic efficiencies of the stator and rotor of the expander are tuned to match the results of the eventual loss model. Also, the compressor efficiency, mass flow and the supply pressure from which hydrogen needs to be compressed are assumed to provide an estimate of the energy consumption of the HRS. Furthermore, a minimum expansion ratio has been defined to ensure that the expander would not stagnate when an equilibrium is reached between a buffer tank and the downstream system pressure. A fixed pre-cooling temperature is set to -33°C, following the SAE J2601 refuelling protocols [94] and fixed pressure drops are assumed over the pre-cooler and the dispenser Finally, pressure drops across the pre-cooler and the dispenser have been defined in line with values found in literature [127].

| Variable | Symbol | Value | Unit |
|---|---|---|---|
| Corrected mass flow rate | $\dot{m}_{corr}$ | 0.000134 | $\frac{kg}{s}$ |
| Total-to-static turbine efficiency | $\eta_{turb,ts}$ | 37.7 | % |
| Total-to-static stator efficiency | $\eta_{stator,ts}$ | 88.7 | % |
| Total-to-static rotor efficiency | $\eta_{rotor,ts}$ | 45.1 | % |
| Compressor efficiency | $\eta_{compressor}$ | 0.8 | % |
| $H_2$ supply pressure | $p_{supply}$ | 20 | $MPa$ |
| Minimum expansion ratio | $ER_{min}$ | 1.2 | – |
| Pre-cooling temperature | $T_{pre-cool}$ | 240.15 | $K$ |
| Pre-cooler pressure drop | $\Delta p_{cooler}$ | 0.1 | $MPa$ |
| Dispenser pressure drop | $\Delta p_{dispenser}$ | 0.1 | $MPa$ |

*Table 6.3: Operational parameters of the HRS system model.*

Finally, the parameters of a to-be-refuelled vehicle are defined according to Table 6.4. These include an initial and target tank pressure as well as a fixed tank volume.

| Variable | Symbol | Value | Unit |
|---|---|---|---|
| Initial vehicle tank temperature | $T_{init}$ | 288.15 | $K$ |
| Initial vehicle tank pressure | $p_{7,init}$ | 5 | $MPa$ |
| Maximum vehicle tank pressure | $p_{7,final}$ | 83 | $MPa$ |
| Vehicle tank volume | $V_7$ | 0.240 | $m^3$ |

*Table 6.4: Initial conditions and target pressure of the vehicle tank.*

### 6.1.2 Turbine design parameters

Apart from the parameters used for the HRS system model, a specific set of design parameters is used for the 1D design of the turbine, their values are shown in Table 6.5. The values of the diameter ratio and the absolute outflow angle of the rotor are already the result of a manual iteration that matches the turbine design with the mass flow calculations of the system model.

| Variable | Symbol | Value | Unit |
|---|---|---|---|
| Flow coefficient | $\phi$ | 0.245 | $-$ |
| Work coefficient | $\psi$ | 0.94 | $-$ |
| Diameter ratio | $\frac{D_2}{D_3}$ | 1.2 | $-$ |
| Absolute inflow angle - Stator | $\alpha_0$ | 0 | $^\circ$ |
| Absolute outflow angle - Rotor | $\alpha_3$ | $-47$ | $^\circ$ |
| Maximum rotational speed | $\omega_{max}$ | $500,000$ | $\frac{1}{min}$ |
| Rotor clearance - Axial | $\tau_a$ | 0.05 | $mm$ |
| Rotor clearance - Radial | $\tau_r$ | 0.05 | $mm$ |
| Rotor clearance - Disk | $\tau_d$ | 0.05 | $mm$ |

*Table 6.5: Parameters used for the design and analysis of the turbine.*

## 6.2 The refuelling process

As described in Chapter 4, the system model aims to model a hydrogen refuelling station comprised of 3 buffer tanks, a radial inlet turbine, a pre-cooler, a dispenser and a to-be-refuelled vehicle tank. All of these components together have been divided over 8 stations which allows us to calculate and analyse the relevant variables at distinct points in the system for every time step, which are defined as 1-second intervals. This section will focus specifically on those results and aim to answer the following question: What does the process of the refuelling cycle look like, and how do the different state variables evolve throughout the process?

First, Figure 6.2 presents a top-level overview of the results of the system model, specifically the pressure, temperature and density in the buffer tanks and the vehicle tank, as well as the final mass in the vehicle tank. In all four subplots, the blue, red and green dashed lines each represent the conditions in one buffer tank, and the solid black line represents the conditions in the vehicle tank. The upper left subplot shows how the pressure in each buffer tank steadily drops from its initial pressure until a minimum expansion ratio to the vehicle pressure is met, after which the next buffer tank is engaged.

Similarly, the upper right subplot shows the temperature change in each of the buffer tanks as its pressure decreases over time, and the black line represents the temperature in the vehicle tank. Here it can be observed that the final tank temperature reaches 328.31K or 55.16°C, well below the maximum limit of 85°C. The lower left subplot displays the density of the gas in each of the buffer tanks and the vehicle tank and finally, the lower right subplot shows the evolution of mass in the vehicle tank.

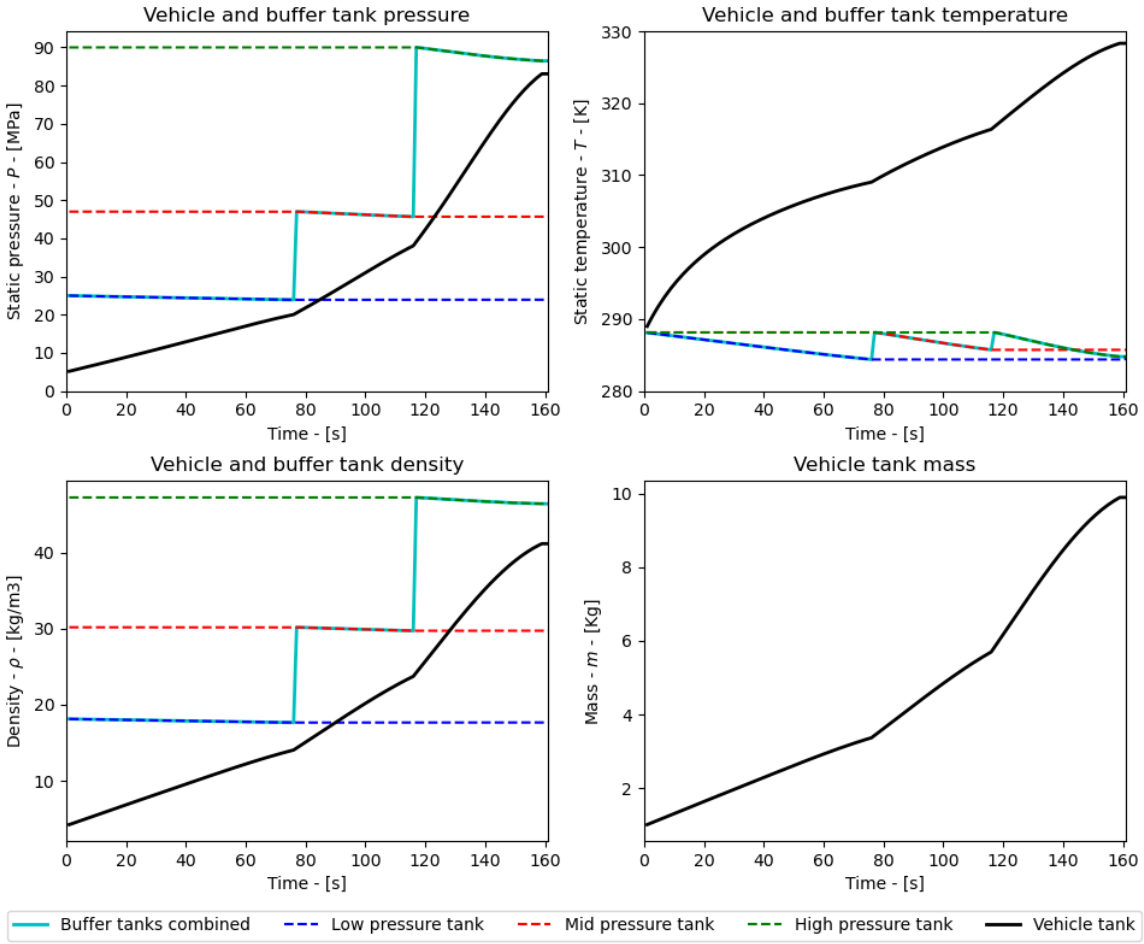


*Figure 6.2: Overview of the pressure, temperature and density in each of the buffer tanks and the vehicle tank during a refuelling process as well as the increase of mass in the vehicle tank.*

Next, Figure 6.3 provides a deeper overview by showing the results of static and total pressure and temperature at each of the different stations. The upper left chart displays the static pressure, and as expected, the static pressure drops significantly across the expander. Specifically between stations 1, 2 and 3, which are the stator inlet, rotor inlet and rotor outlet, respectively. When analysing the numerical results, there is also a slight difference between stations 4, 5 and 6 due to the pressure drop in the heat exchanger and dispenser.

The upper right chart presents the same graph for the total pressure. This shows the total pressure to stay constant across the stator between stations 1 and 2 and across the rest of the system after the rotor, stations 3 until 6.

For the static temperature, it can be observed in the lower left chart that both the stator and the rotor cause a cooling effect throughout the entire cycle. It can also be observed that the temperature at the outlet of the diffuser surpasses the cooling threshold already in the first timestep, requiring the pre-cooler to be active for the whole duration of the refuelling cycle. However, the difference between $T_4$ and $T_5$ starts off small and ramps up over time, allowing for the pre-cooler to come into action as opposed to needing to provide a significant temperature drop instantaneously. Finally, the total temperature is shown in the lower right chart, where it can be observed that, indeed, the total conditions remain constant across the stator vanes and throughout the diffuser.

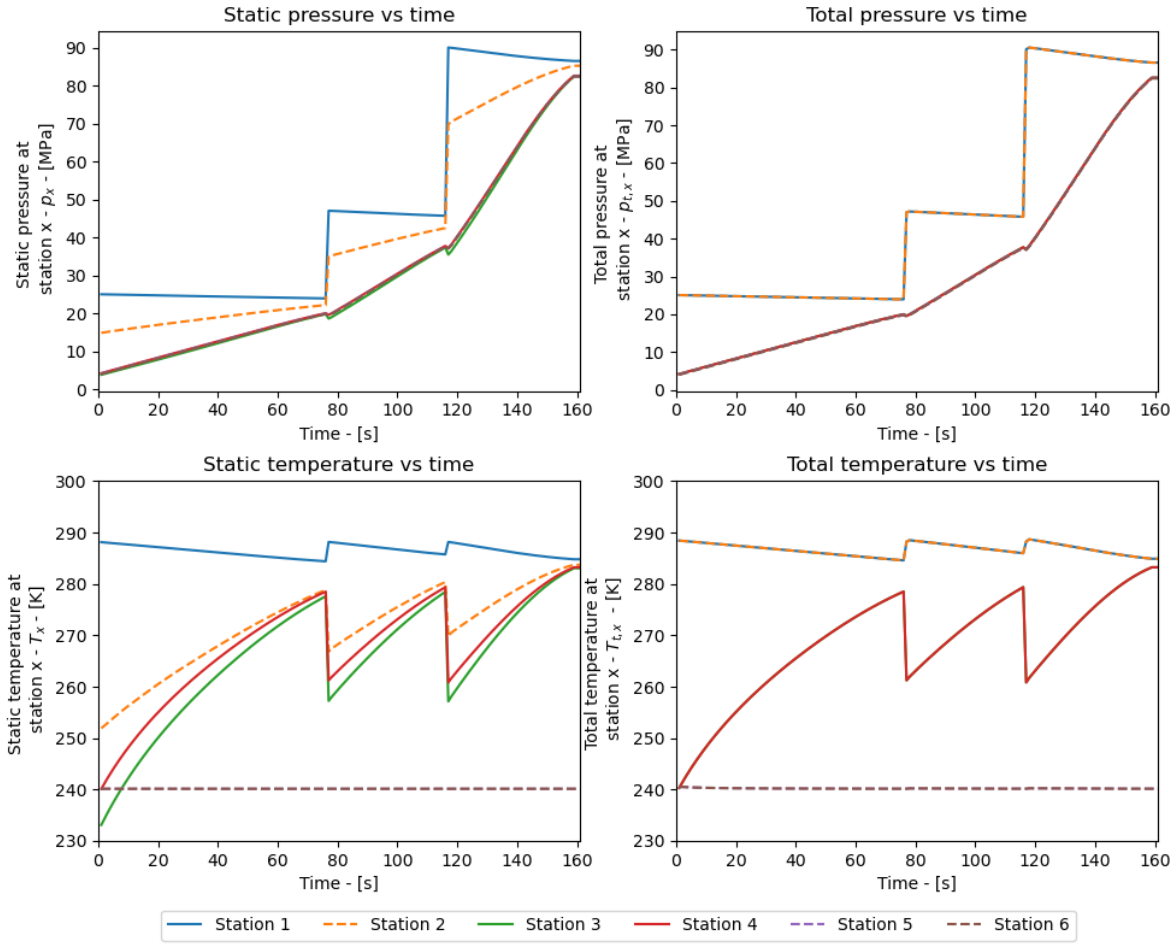


*Figure 6.3: Overview of the static and total pressure and temperature for each of the stations during a refuelling process.*

Although Figure 6.3 is able to portray how the static and total conditions change over time during a refuelling process, the changes from one station to the other are easily lost due to the resolution of the graph. Figure 6.4 aims to provide a solution for this by plotting individual time steps as a single line which changes value across the different stations. For clarity, only every $5^{th}$ time step is plotted. Specifically, When looking at the final time steps in the left subplot (light green), the variation across stations can be observed. The pressure remains constant between the buffer tank and the inlet of the expander, then it drops as the flow passes through the stator vanes (1-2) and then more significantly when passing through the rotor (2-3). Next, the static pressure can be seen to increase slightly across the diffuser (3-4), after which there is a very small pressure loss across the pre-cooler and dispenser (4-5-6). Finally, the pressure rises once more due to thermal effects in the vehicle tank. The right chart shows the same for the total pressure between stations 1 and 6.

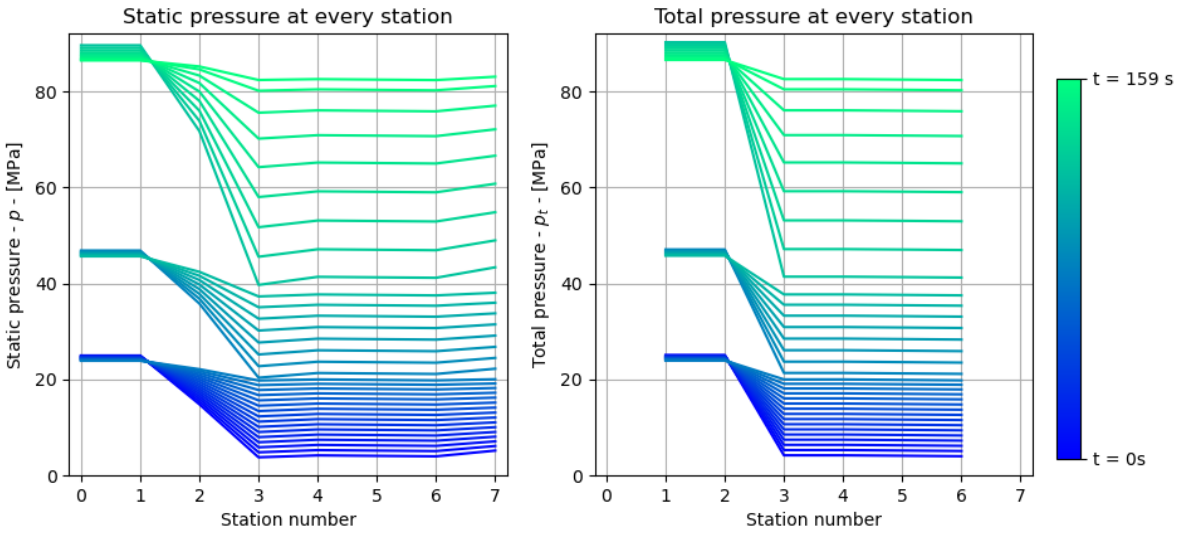


*Figure 6.4: Variation of static and total pressure between stations for every $5^{th}$ timestep.*

Next, Figure 6.5 shows how the expansion ratio across different stations evolves over time. From left to right, there is the static-to-static expansion ratio, the total total-to-static expansion ratio and the total total-to-total expansion ratio.

Plotted as a dashed black line, the critical expansion ratio of hydrogen can also be seen. As can be observed in the middle chart, the total-to-static expansion ratio across the stator is never higher than the critical expansion ratio, but it is across the rotor. From this, it can be deduced that the rotor will experience a choked flow at several points throughout the refuelling process but that the stator will never be choked.

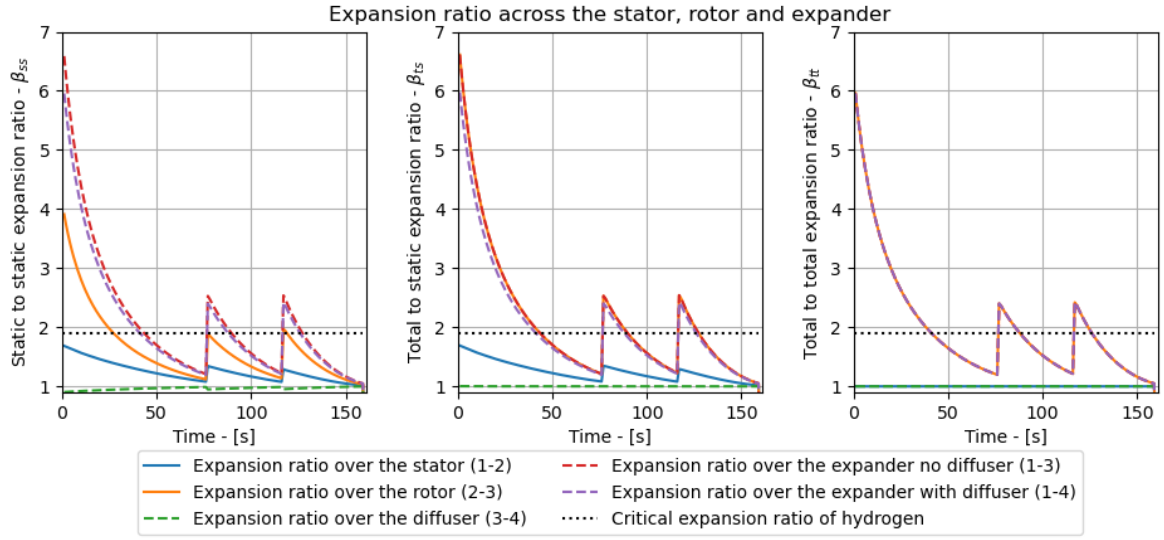


*Figure 6.5: Time-wise evolution of the expansion ratios between different stations in the system. Static-to-static on the left, total-to-static in the middle and total-to-total on the right.*

This is further represented in Figure 6.6, which shows the corrected mass flow rate (left) and the real mass flow rate (right) throughout the refuelling cycle.

As described in Subsection 4.3.4, when the expansion ratio across the nozzle is higher than the critical expansion ratio of the gas, the nozzle is considered to be choked, which means that the mass flow through the nozzle can physically not increase further. In the model, this is represented by assuming a corrected mass flow rate which translates to a real mass flow rate for a given pressure and temperature. As the mass flow rate is known to be constant when the turbine is choked, it is assumed as a fixed corrected mass flow rate which is re-evaluated accordingly when the turbine is not choked. this is visible on the left chart in Figure 6.6. The right chart on the other hand displays the actual mass flow rate. The three distinct steps in the chart relate to each of the three phases of the refuelling cycle based on which buffer tank is in use. Furthermore, the mass flow can be seen to vary slightly even when the flow is choked as the pressures in the system also change.

As mentioned in Subsection 6.1.1, the value of the corrected mass flow rate has been set iteratively to match the maximum value of the real mass flow rate to the limit of 120g/s.

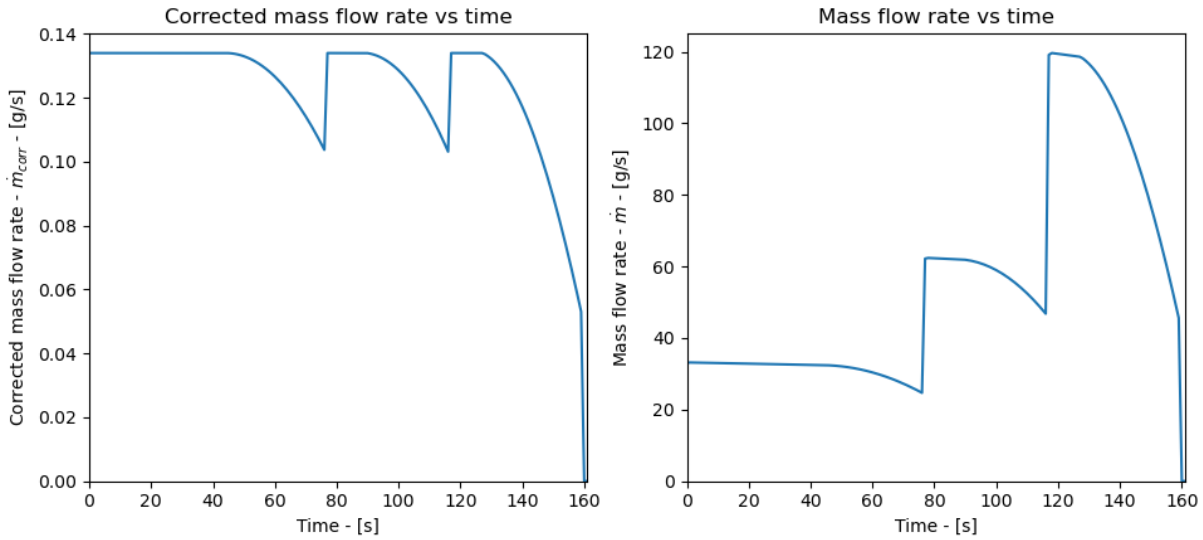


*Figure 6.6: Corrected and real mass flow rate over time.*

As previously explained in both Subsection 4.3.1 and Subsection 6.1.1 and as shown in Figure 6.6, a fixed corrected mass flow rate has been assumed. Furthermore, the pressure levels of the station's buffer tanks have been set manually in an attempt to provide an "as optimal as possible" operating profile for the turboexpander. This can be visually seen in Figure 6.5, where the profile of the expansion ratio (after the first 30 seconds) is repeated almost exactly three times for the different phases.

Combined, these two assumptions result in the fact that the data points on the left chart in Figure 6.7, overlap almost completely for the majority of the refuelling process.

This shows that the performance of the turbine can be expected to be quite consistent across the entire refuelling cycle, despite vastly varying in- and outlet conditions. Excepted from this are the start and end of the refuelling cycle as the expansion ratios can simply not be matched without compromise elsewhere.

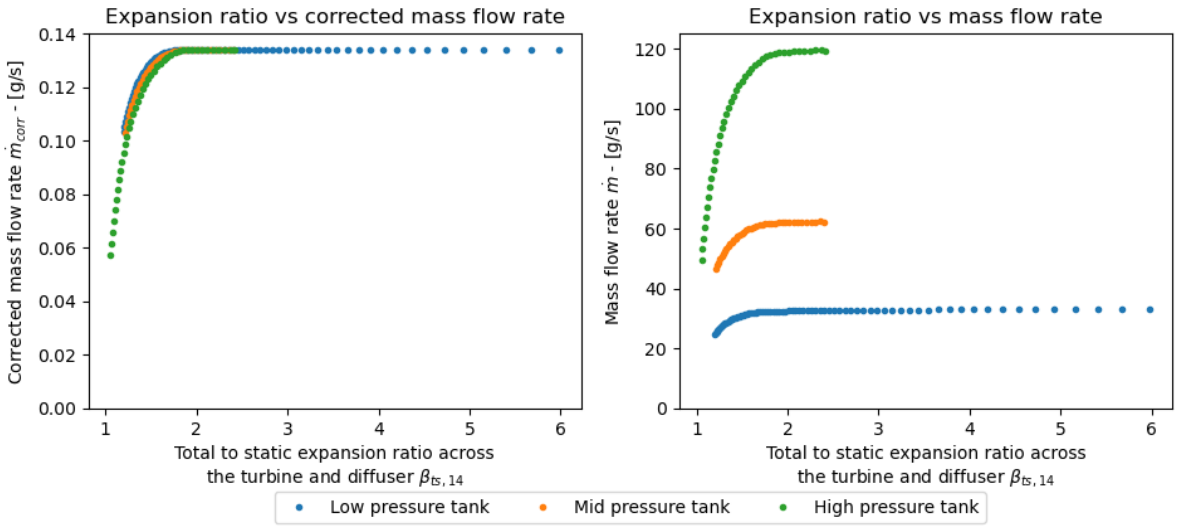


*Figure 6.7: Corrected and real mass flow rate vs total-to-static turbine expansion ratio - between stations 1 and 3.*

## 6.3 1D turbine analysis

Now that the results of the refuelling process itself have been presented in Section 6.2, this section will continue with detailing the results of the turbine design procedures, the selection of the optimal design point and the analysis of the performance of that turbine design.

As described previously, the system model initially assumes fixed turbine efficiencies $\eta_{stator}$ and $\eta_{rotor}$ to estimate how the flow properties change across the expander. Next to these efficiencies, it also uses an optimal assumption of the flow and work coefficients, $\Phi$ and $\Psi$, which it uses to determine a quasi-optimal turbine design for the conditions at every time step. However, we do not want an individual turbine for every second of the refuelling process; We would want a single turbine design that operates throughout the entire refuelling cycle, and that delivers the best overall performance.

To establish this, Subsection 6.3.1 will first present how the loss models have been used to determine which design iteration is the most optimal when applied across the entire refuelling cycle. After which Subsection 6.3.2 will detail the results of the design iteration connected to the selected design point and Subsection 6.3.3 will cover the performance of that design throughout the refuelling cycle.

### 6.3.1 Selection of the design point

As detailed in Section 5.1, the calculations used for an initial turbine design are dependent on certain state variables at the in and outlet of the turboexpander. However, as a refuelling process is inherently a dynamic process, these in and outlet conditions vary continuously, affecting the efficiency of the turbine as it would mostly be operating at sub-optimal operating points - the off-design conditions. But still, a specific point along the refuelling process has to be selected to serve as a design point for the turbine.

Initially, attempts were made to manually define this point based on which conditions were thought to lead to the highest achieved efficiency but it was soon realised that optimal perfor-

mance at the design point would not necessarily correlate to an optimal efficiency over an entire refuelling cycle. Because of this, the current method has been adopted, which, as explained in Subsection 5.2.1, generates a distinct turbine design for each time step in the refuelling process. After the process itself is simulated and a number of turbine designs have been generated, the loss models defined in Subsection 5.2.1 are applied to each of these possible designs. As the loss models are dependent on both geometric features of the turbine design and on the operating conditions in the system, they can be used to predict the losses for every possible turbine design for every time step in the process. Finally, these results can be used to calculate the efficiencies achieved by each design, which can be evaluated to determine the most optimal design. The results of these are shown in the following figures.

Figure 6.8 shows the range of efficiencies of each turbine design when evaluated across the entire refuelling process. In this figure, every set of blue, green and red dots represents the minimum, average and maximum efficiency of the design iteration of its respective time step.

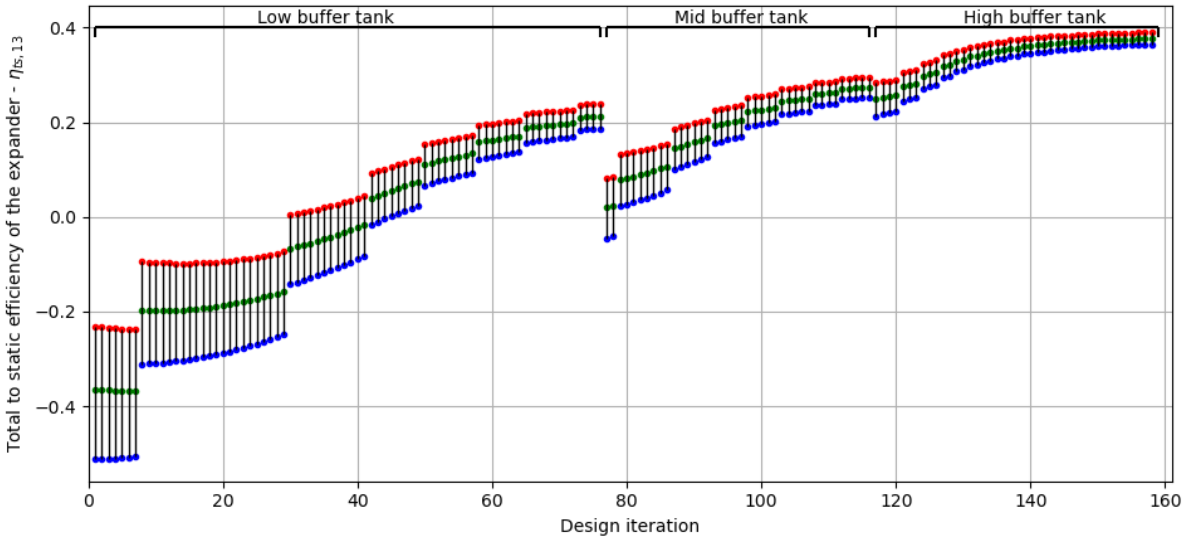


*Figure 6.8: Minimum (blue), average (green) and maximum (red) efficiencies of each turbine design when evaluated over a whole refuelling cycle according to the loss models.*

As each line represents the overall performance of a turbine when designed for the conditions at that time step, there is a lot of information within the trends in this graph.

It is clear that the design centred around the final time step has the best overall performance. This point will thus be selected as the design point and the results of its performance and design specifications will be covered extensively in Subsection 6.3.2. However, there are several observations to be made to the trends shown in Figure 6.8, which will be covered in the remaining part of this subsection.

The following paragraphs will attempt to dissect the individual trends and effects that can be seen.

- First, three distinct "phases" can be seen, each referring to a phase in the refuelling cycle where a certain buffer tank is active, this is also indicated by the annotations in the plot. As can be seen, the designs related to each of these phases, increase in efficiency, a trend that can also be seen in Figure 6.6. From this, it can be deduced that designing for a higher mass flow has a positive effect on the overall efficiency of the expander.

- Secondly, a lot of step-wise jumps can be observed. Upon analysing the numerical results it can be found that these relate to a change in the number of rotor blades. As these are rounded to the nearest integer, they introduce a discrete change every time a design results in more or less rotor blades.
- Thirdly, overlooking these stepwise changes and looking within one "phase" of the plot, another s-shaped curve can be seen in the slope between these points. Although present in all three parts this is especially apparent in the first part relating to the low buffer tank. Here the slope between the designs can be seen to increase until the $\pm 40^{th}$ iteration. After this, the slope between the designs decreases again. Upon comparing this to Figure 6.5 and Figure 6.6, it can be seen that the inflection point of the slope occurs almost exactly at the point where the rotor transitions from being choked to not being choked. Added to this, we know that within each part, the expansion ratio decreases and that the mass flow is practically constant when the rotor is choked but decreases rapidly when the rotor is not choked.

  From the first section, where the flow is choked, the expansion ratio decreases, the mass flow is constant and the efficiency tends to increase, it can be deduced that in general, designing for a lower expansion ratio leads to a more efficient design.

  In the second section, where the flow is no longer choked, the effect of the lower mass flow is superimposed on the previous effect. Here the expansion ratio still decreases, but so does the mass flow and the slope of the efficiency increase can be seen to reduce. From this, we can deduce that designing for a lower mass flow decreases the overall efficiency, which aligns with the previous deductions.
- Fourth, it can be observed that the designs relating to the first 45 time steps result at least partially in negative efficiency values at some point along their operation - keeping in mind that each vertical line represents a refuelling cycle with the blue and red dots representing the minima and maxima. In practical terms, this means that the calculated losses - according to the adopted loss models - result in a higher enthalpy change than what the turbine would be able to perform isentropically. Of course, this does not make sense in physical terms and presents a point of concern if the adopted loss models and the factors and assumptions that they are based on are in fact suitable to this application. this will be reflected upon later in the conclusion.

In summary, this graph indicates that, following the loss models implemented, the highest efficiencies can be achieved for a design centred around a (relatively) lower expansion ratio and higher mass flow.

As explained, each set of blue, green and red dots in Figure 6.8 represents the efficiency range of one specific design iteration according to the system variables at that time step. Next, Figure 6.9 presents a closer look the losses of some selected design points. Each subplot presents the result of one design point, the blue and red dots again indicate the minimum and maximum efficiency of that design and the different colours represent the contribution of different loss mechanisms.

To present a result that is as informative as possible, the selected points are the design points relating to the first, middle, and last time step of each of the three phases that relate to the different buffer tanks, excluding the results that lead to negative values.

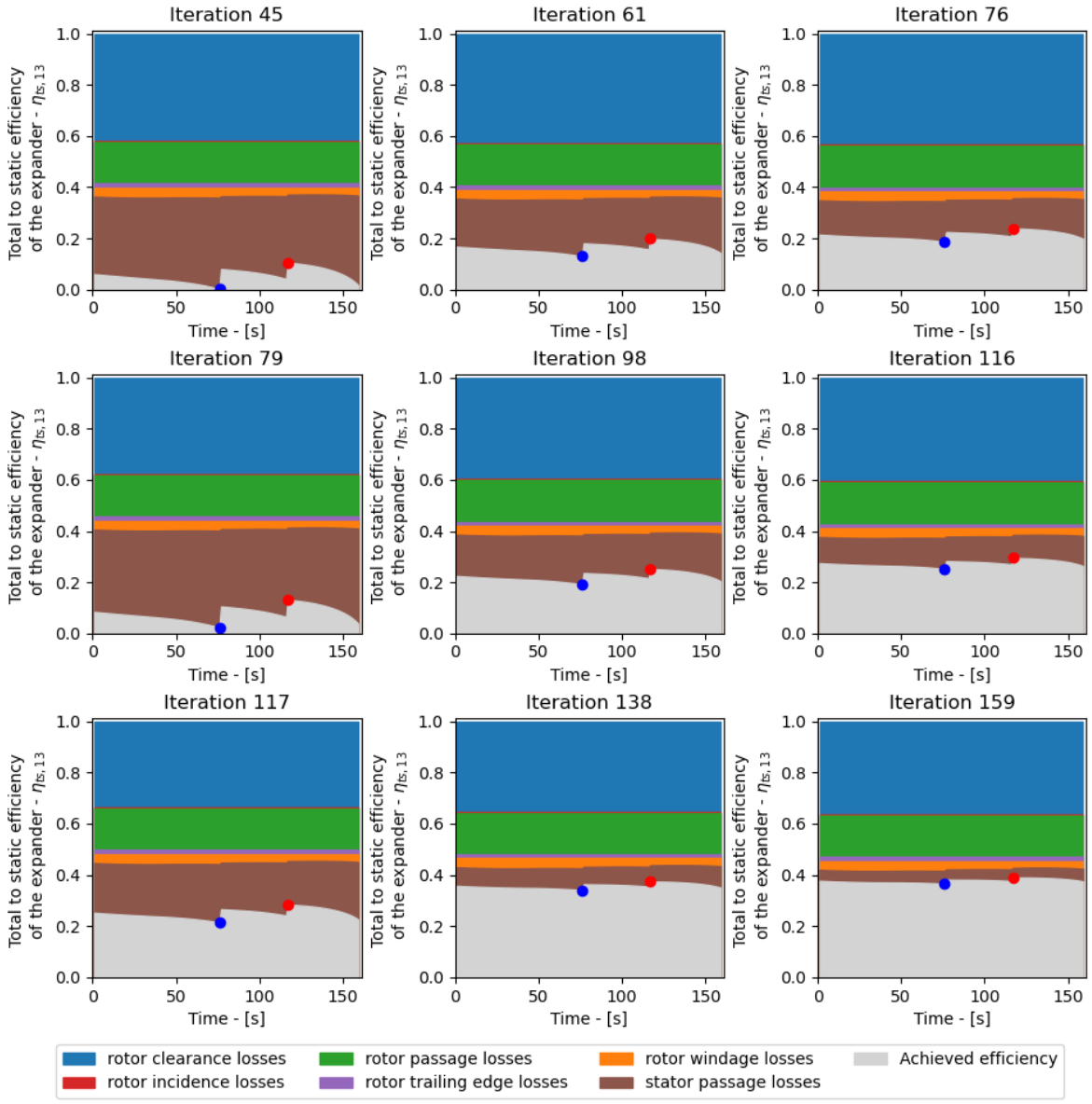


*Figure 6.9: An overview of the contribution of each loss model to the overall losses of select turbine design iterations over time. Each design's minimum (blue) and maximum (red) efficiency points are indicated.*

There are again several interesting observations to be made from analysing the losses within these plots.

First and foremost, it can be observed that the largest contributors to the losses are the rotor clearance losses, the rotor passage losses and the stator passage losses. Each of which are heavily affected by the physical dimensions and shape of the turbine, these will thus also be reflected upon in a later section after the geometry of the turbine has been presented.

Second, it can be observed that the only losses whose relative contribution changes over time (within one subplot) are the windage losses and the stator passage losses, all the other mechanisms appear to scale with the overal enthalpy change across the turbine.

Beyond that, several other observations can be made on how the losses change between the

different designs - represented by the different subplots. Remember that within each phase of the refuelling cycle; the trend was that both the expansion ratio and the mass flow decreased. However, between the different phases, the trend was that the mass flow increases. In Figure 6.9, the design points relating to each phase are next to each other on a horizontal row of subplots and the three different rows of subplots relate to the designs in each of the three phases.

Overall, four distinctions can be made.

- First, there are the loss models that do not seem to vary in magnitude over time (within one subplot) or between different design points (different subplots). This does not mean that they are always constant for every possible turbine design but simply that they do not vary with the changes that this model and design method brings. An example can be found in the rotor incidence losses which are heavily dependent on the flow angles. As these are the same for all the design iterations, these losses indeed do not vary. But a design that assumes a different flow and work coefficient would for example, result in different incidence losses. Two other loss mechanisms that appear unaffected in this model are the rotor passage losses and the rotor trailing edge losses.
- Second, there are the losses that vary over time but not between different design points. The windage losses are an example of this. Within the assumptions made in this work , the windage clearance is for example assumed to be constant and thus the losses only vary with flow properties. However, a vastly different design with different windage clearances would logically result in a different result.
- Third, there are the losses that are constant over time and thus scale with the specific work of the expander but that vary between design points, for example, the rotor clearance losses. The logical explanation for this is that the rotor clearances are assumed as a fixed constant for all designs. Thus, as the design changes or scales, the ratio between the clearances between the blade and the shroud and the actual blade height changes and so does the relative effect of the clearance gap.
- Lastly, the stator passage losses appear to vary vastly both over time and between different design points. Overall, the trend of its shape within one subplot is very reminiscent of the shape of the mass flow curve shown in Figure 6.6, with the losses increasing as the mass flow decreases. However, this is not entirely consistent when observing the trends between the different design points and it can thus be concluded that the mass flow is not the main variable on which the stator passage losses are dependent but that there must be a coupling to some other variables as well.

### 6.3.2 1D turbine design results

As presented in Subsection 6.3.1, the evaluation of the loss models resulted in a single design point (t=159) which would lead to the best overall performance. This subsection will cover the final details of the turbine design resulting from that design point and its general performance throughout the refuelling process.

First, the results of the flow angles at the design point can be found in Table 6.6. These are a direct result of the assumed flow and work coefficients $\Phi$ and $\Psi$ and the calculated rotor tip speed $u_2$. Please note that the values at the rotor outlet (Station 3) are considered at the mid-point of the blade height.

| Variable | Symbol | Value | Unit |
|---|---|---|---|
| Absolute inflow angle of the stator | $\alpha_1$ | 0 | ° |
| Absolute inflow angle of the rotor | $\alpha_2$ | 75.39 | ° |
| Relative inflow angle of the rotor | $\beta_2$ | -13.76 | ° |
| Absolute outflow angle of the rotor | $\alpha_3$ | 0 | ° |
| Relative outflow angle of the rotor | $\beta_3$ | -77.40 | ° |

*Table 6.6: Overview of the flow angles and velocity components of the turbine at the design point.*

Next, the other geometrical features of the turbine design such as the relevant diameters, blade heights, flow areas and the number of blades can be found in Table 6.7.

| Variable | Symbol | Value | Unit |
|---|---|---|---|
| Stator inlet diameter | $D_1$ | 60.33 | mm |
| Rotor inlet diameter | $D_2$ | 49.44 | mm |
| Rotor outlet diameter - hub | $D_{3,h}$ | 41.08 | mm |
| Rotor outlet diameter - shroud | $D_{3,s}$ | 41.33 | mm |
| Rotor inlet blade height | $b_2$ | 0.104 | mm |
| Rotor outlet blade height | $b_3$ | 0.127 | mm |
| Stator inlet area | $A_1$ | 19.63 | $mm^2$ |
| Rotor inlet area | $A_2$ | 16.09 | $mm^2$ |
| Rotor outlet area | $A_3$ | 16.41 | $mm^2$ |
| Diffuser outlet area | $A_4$ | 78.54 | $mm^2$ |
| Number of stator blades | $N_{B,S}$ | 28 | - |
| Number of rotor blades | $N_{B,R}$ | 10 | - |

*Table 6.7: Overview of the final dimensions of the turbine design.*

Together they lead to the geometry shown in Figure 6.10

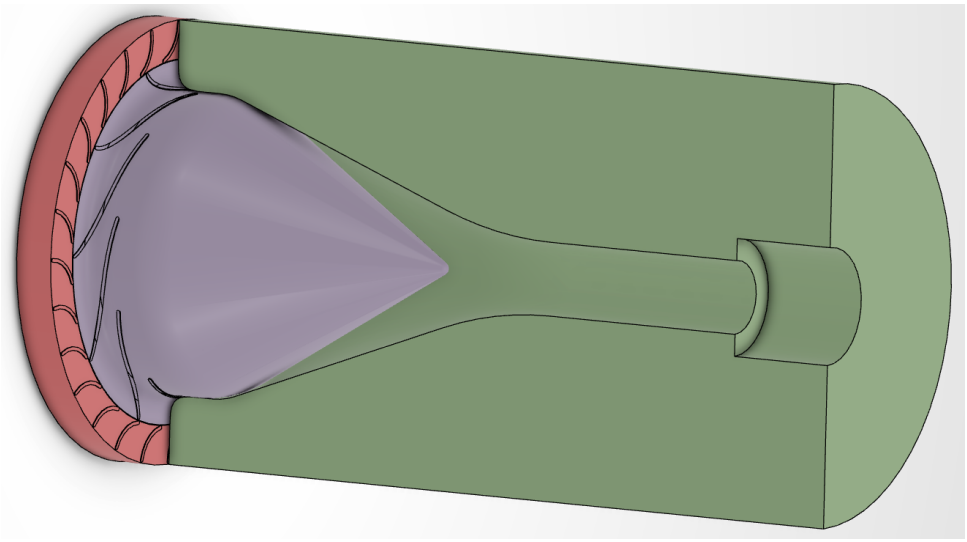

*Figure 6.10: A 3D CAD model of the turbine design. Featuring a stator (red), the rotor (purple) and a shroud (green) with an integrated diffuser diverging at 10°to the specified outlet pipe diameter*

### 6.3.3 1D turbine performance results

As shown before in Figure 6.8 and Figure 6.9, the total-to-static efficiency of this turbine design ranges between 36.50% and 38.98%. Figure 6.11 presents a closer look at the absolute values of these losses with respect to the achieved specific work over the expander. The left chart shows the absolute values of the specific enthalpy changes and the right chart presents the values normalised to the specific isentropic work over the expander.

From these charts, it is clear that the overall losses indeed reduce throughout the refuelling process. When comparing these results in the left chart to the expansion ratio as shown in Figure 6.5, it becomes clear that the total values of the losses indeed scale with the expansion ratio, but so does the overall isentropic work of the expander. So the percentage of losses to the isentropic work remains relatively constant throughout the refuelling process. This is to be expected as the system model assumes the rotor speed to be varied in order to maintain the same work and flow coefficient throughout the entire cycle.

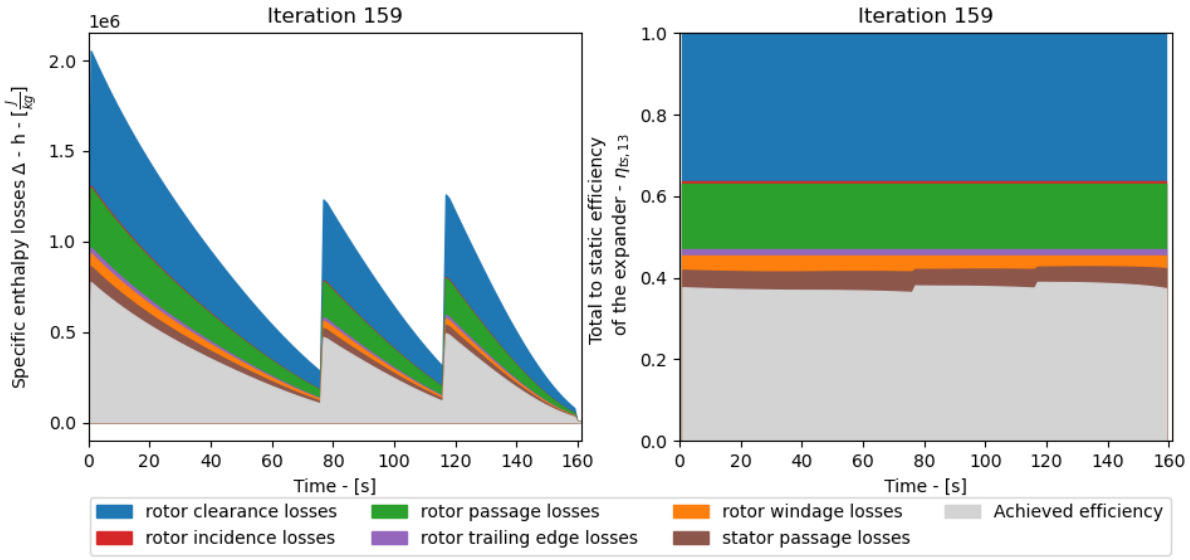


*Figure 6.11: Total values of each of the losses of the selected design (left). Detailed overview of the contribution of each loss model to the overall losses of the selected design (right).*

Finally, the enthalpy change over the rotor can be combined with the mass flow to result in the instantaneous shaft power of the rotor. When integrated over time, this results in the cumulative sum of recovered energy as presented in Figure 6.12. Both charts present the results of a perfect expander with no losses in blue and the real expander with the losses accounted for in orange.

As can be observed, the peak shaft power of the rotor would be 50.45 kW and assuming no further conversion losses, the overall recovered energy of the turbine would be 0.65 kWh or 2.345 MJ.

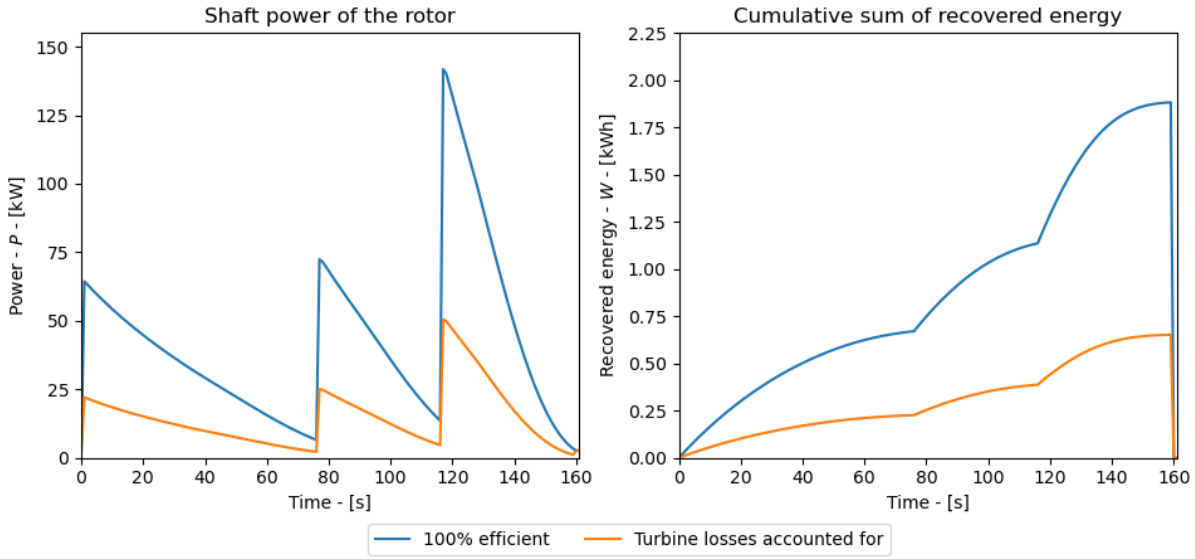


*Figure 6.12: Turbine shaft power (Left) and cumulative sum of recovered energy of the turbine (Right).*

### 6.3.4 Feasibility of the 1D results

As described in Subsection 6.3.2 and Subsection 6.3.3, the 1D model finds a turbine design that features an inlet blade height of 0.104 mm and is supposed to operate at a peak rotor speed of 500,000 rpm, handle a mass flow of up to 0.12 $\frac{kg}{s}$ and delivers up to 50 kW of shaft power.

When comparing these values to the design features and operating conditions of more traditional turbo-machines, these might appear to be rather extreme but one should also remember that the inlet pressure and density at the design point are 865 bar and 46.4 $\frac{kg}{m^3}$. Both of these can already serve as an indication that the regime in which this turbine would operate is vastly different than that of any other turbomachine.

This is also exemplified by the difference between the mass flow rate $\dot{m}$ and the corrected mass flow rate $\dot{m}_{corr}$. The peak mass flow rate of 120 g/s is comparable to what can be found in turbochargers for cars, but the corrected mass flow rate of 0.000134 $\frac{kg}{s}$ is orders of magnitude smaller.

Furthermore, it also makes sense that such a relatively small amount of gas, which is compressed to such high pressures and densities, only takes up a very small volume. After all, for the application in hydrogen pressure vessels, that is why it is compressed in the first place.

However, next to understanding the magnitude of high pressures and densities in this system and how they result in the presented size of the turbine blades, one should also consider whether the flow through such a narrow passage is even remotely feasible or if the entire passage height would be taken up by the boundary layer. One predictive manner through which we can analyse this is the Reynolds number $Re$ which presents the ratio between the inertial forces and the viscous forces in the flow as presented in Equation 6.1. For this application, the characteristic length of the channel is replaced with the blade height $b$ and the relative velocity $w$ is used instead of the absolute velocity $v$.

$$Re = \frac{\rho v L}{\mu} = \frac{\rho w b}{\mu} \tag{6.1}$$

As can be observed in Figure 6.13, the Reynolds number of the flow varies between 23,438 and 103,300 at the rotor inlet and between 93,790 and 424,170 at the rotor outlet. At first sight, these values of the Reynolds number could be considered relatively high for the small size of the turbine, but one should remember that the medium is pure hydrogen as opposed to an air-fuel mix in most other turbomachinery applications and has very different properties. This becomes clearwhen analysing the values of the kinematic viscosity of hydrogen. When comparing this value to that of air in the same conditions or in other typical turbomachinery applications, we find the following:

- It is 2 - 4.5 times lower than that of air at similar pressures and temperatures.
- 1 - 8 times lower than that of air at the conditions found in at the high pressure turbine in an airplane engine (p=15 bar, T=1,500 K).
- 10 - 88 times lower than that of air in a typical automotive turbocharger (p=1.2 bar, T=400 K).

Thus indeed, the same turbine operating in the same system with air as a medium would exhibit a 2 - 4.5 times lower Reynolds number. The other comparisons serve a purely illustrative purpose to show how much this value of the kinematic viscosity differs from what one might be used to in other systems, as usually, the velocity, density, and size are driving factors behind an analysis of the Reynolds number and the kinematic viscosity is a standard value for that application.

From the magnitude of the values shown in Figure 6.13 it can also be deduced that the boundary layer will be turbulent throughout the entire passage.

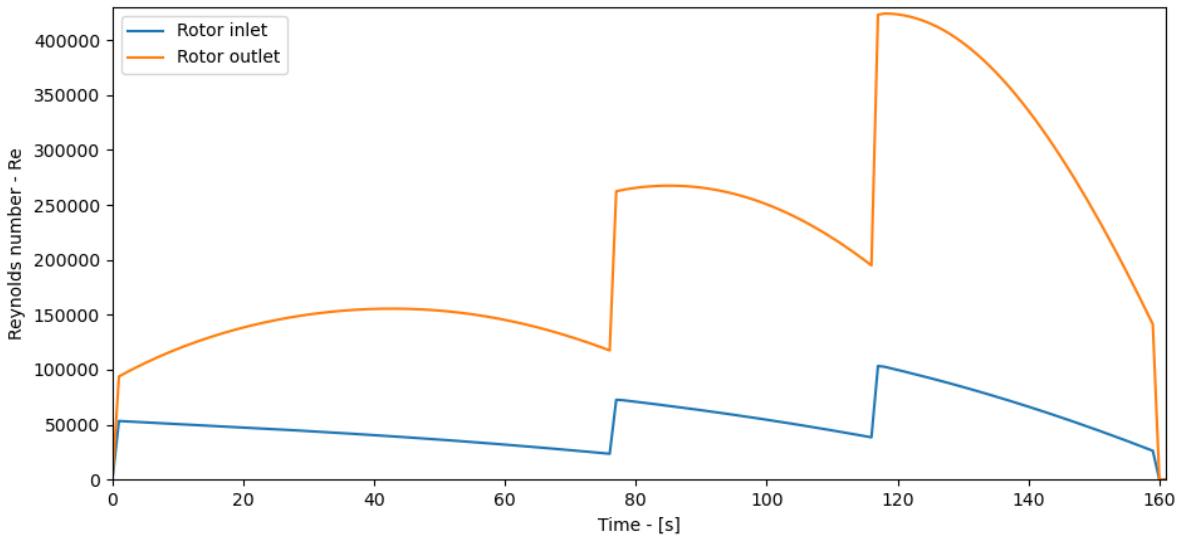


*Figure 6.13: Reynolds number for the selected design at the stations 2 (rotor inlet) and 3 (rotor outlet).*

## 6.4 3D turbine analysis

After the results of the 1D model had been obtained, these were used to perform a 3D analysis at the design point in Ansys as described in Subsection 5.2.2. First, an overview of the input parameters of the 3D model is presented in Subsection 6.4.1, after which the set-up of the model is described in Subsection 6.4.2 and the convergence of the simulation cases is presented

in Subsection 6.4.3. The results are split between Subsection 6.4.4 and Subsection 6.4.5, which respectively cover the numerical results and graphical results and the discussion thereof. Finally, a comparison to the 1D model will be presented in Subsection 6.4.6.

### 6.4.1 Selection of the operating point

In the past section, the term "Design point" has been used to refer to the time step for which the design iteration leads to the best overall performance when analysed over an entire refuelling cycle. And the previous performance results are all the result of a refuelling cycle with that specific design. However, as this section will describe the results of a 3D analysis, a single time step has to be chosen from which the flow conditions will be used as input to the 3D model; to avoid any confusion between these two points, this shall be called "The operating point" from here on.

The reason for simulating a different operating point in the 3D model is that even though the design point leads to the overall best performance, it is not equal to the actual point of maximum efficiency as is indicated by the red dot in Figure 6.9. The point of maximum efficiency lies at time step 117. Because of this, it was deemed that selecting this point as the operating point to be simulated in the 3D model would provide more valuable results. The exact conditions at this time step are summarised in the figures and tables below.

Aside from the geometric design parameters that have previously been presented in Table 6.6 and Table 6.7, the flow conditions at this operating point can be seen in Table 6.8 and the velocity triangles are visualised in Figure 6.14.

| Variable | Symbol | Value | Unit |
|---|---|---|---|
| Static pressure at the stator inlet | $p_1$ | 90.00 | $MPa$ |
| Total pressure at the stator inlet | $p_{t,1}$ | 90.09 | $MPa$ |
| Static temperature at the stator inlet | $T_1$ | 288.15 | $K$ |
| Total temperature at the stator inlet | $T_{t,1}$ | 288.24 | $K$ |
| Density at the stator inlet | $\rho_1$ | 47.30 | $\frac{kg}{m^3}$ |
| Absolute velocity at the stator inlet | $v_1$ | 50.38 | $\frac{m}{s}$ |
| | | | |
| Static pressure at the rotor inlet | $p_2$ | 69.77 | $MPa$ |
| Total pressure at the rotor inlet | $p_{t,2}$ | 90.09 | $MPa$ |
| Static temperature at the rotor inlet | $T_2$ | 269.78 | $K$ |
| Total temperature at the rotor inlet | $T_{t,2}$ | 288.24 | $K$ |
| Density at the rotor inlet | $\rho_2$ | 41.96 | $\frac{kg}{m^3}$ |
| Absolute velocity at the rotor inlet | $v_2$ | 984.37 | $\frac{m}{s}$ |
| Relative velocity at the rotor inlet | $w_2$ | 256.61 | $\frac{m}{s}$ |
| Tip speed at the rotor inlet | $u_2$ | 1013.35 | $\frac{m}{s}$ |
| | | | |
| Static pressure at the rotor outlet | $p_3$ | 35.46 | $MPa$ |
| Total pressure at the rotor outlet | $p_{t,3}$ | 37.22 | $MPa$ |
| Static temperature at the rotor outlet | $T_3$ | 257.14 | $K$ |
| Total temperature at the rotor outlet | $T_{t,3}$ | 260.84 | $K$ |
| Density at the rotor outlet | $\rho_3$ | 26.66 | $\frac{kg}{m^3}$ |
| Absolute velocity at the rotor outlet | $v_3$ | 364.03 | $\frac{m}{s}$ |
| Relative velocity at the rotor outlet | $w_3$ | 1138.10 | $\frac{m}{s}$ |
| Mid-span speed at the rotor outlet | $u_3$ | 844.45 | $\frac{m}{s}$ |

*Table 6.8: Overview of the flow conditions of the turbine at the operating point.*

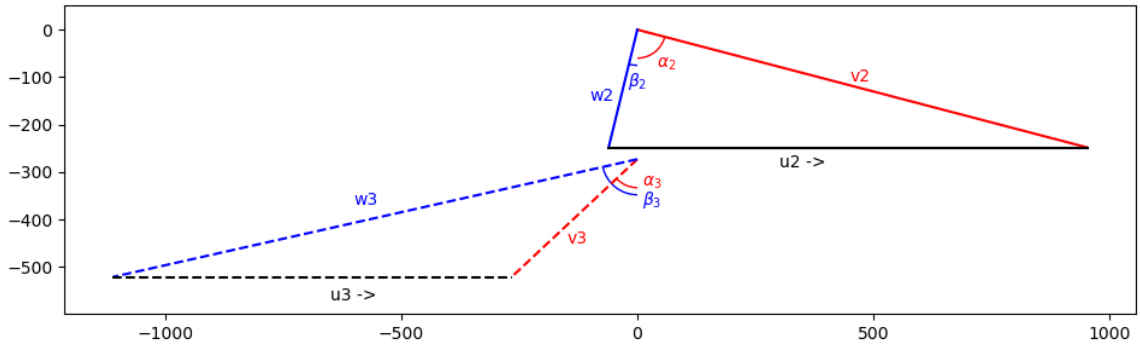


*Figure 6.14: Velocity diagram of the selected turbine at the operating point.*

### 6.4.2 Ansys set-up

As described in Subsection 5.2.2, the Ansys workbench model exists out of three blocks: BladeGen, TurboGrid and CFX. First, the geometrical features of the turbine, presented in Table 6.6 and Table 6.7, are used to create a 3D model of the turbine in BladeGen. With the exception that the diameter of the inflow area of the rotor has been enlarged to 52 mm after several warnings in CFX. This has been done to prevent excessive back-flow through the inlet domain in the CFD model, which would affect the boundary conditions. The diameter of the blade portion of the rotor has not been changed. After that, TurboGrid automatically generates a

mesh for this geometry in which several parameters can be adjusted to provide a sufficient grid density. The exact settings can be found in detail in Appendix A. Finally, the simulation case is defined in CFX-Pre. In order to mimic the operating point, several parameters, as shown in Table 6.9, are defined at the in- and outlet domains of the rotor.

Apart from these operating parameters, the model also requires fluid information. The real gas model includes a more elaborate definition which can be found attached in Appendix A. It should also be noted that, in light of the 1D results, there is one other significant difference between the CFD model and the 1D model. The 1D model assumes a certain clearance between the blade and the shroud of the turbine, which, as presented in Figure 6.11 makes up quite a large part of the overall predicted losses. The 3D model, however, assumes no shroud clearance and instead assumes a wall as the shroud.

| Variable | Symbol | Value | Unit |
|---|---|---|---|
| Inlet total pressure | $p_3$ | 90.10 | MPa |
| Axial component of the inlet flow direction | – | 0 | - |
| Radial component of the inlet flow direction | – | -0.252238 | - |
| Theta component of the inlet flow direction | – | 0.96766 | - |
| Inlet total temperature | $T_2$ | 288.24 | K |
| Outlet static pressure | $p_3$ | 35.46 | MPa |
| Rotor speed | $\omega_{rotor}$ | 391424 | $\frac{rev}{min}$ |

*Table 6.9: Overview of the input parameters to CFX-Pre to model the operating point of the turbine.*

### 6.4.3 Convergence of the results

In order to monitor the convergence, several variables, such as the static and total pressures, temperatures and enthalpies, as well as mass flow and velocity, were monitored at both the in- and outlet of the domain. The convergence results of total pressure, temperature and mass flow can be seen in Figure 6.15 and Figure 6.16.

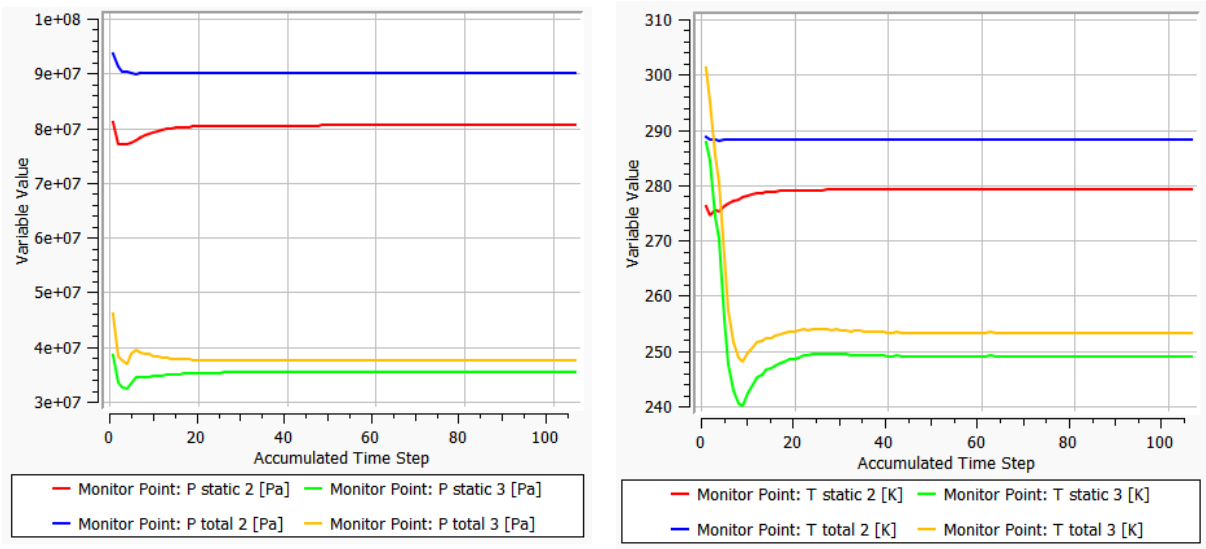


*Figure 6.15: Convergence of static and total pressure (left) and temperatures (Right) at the rotor inlet and outlet.*

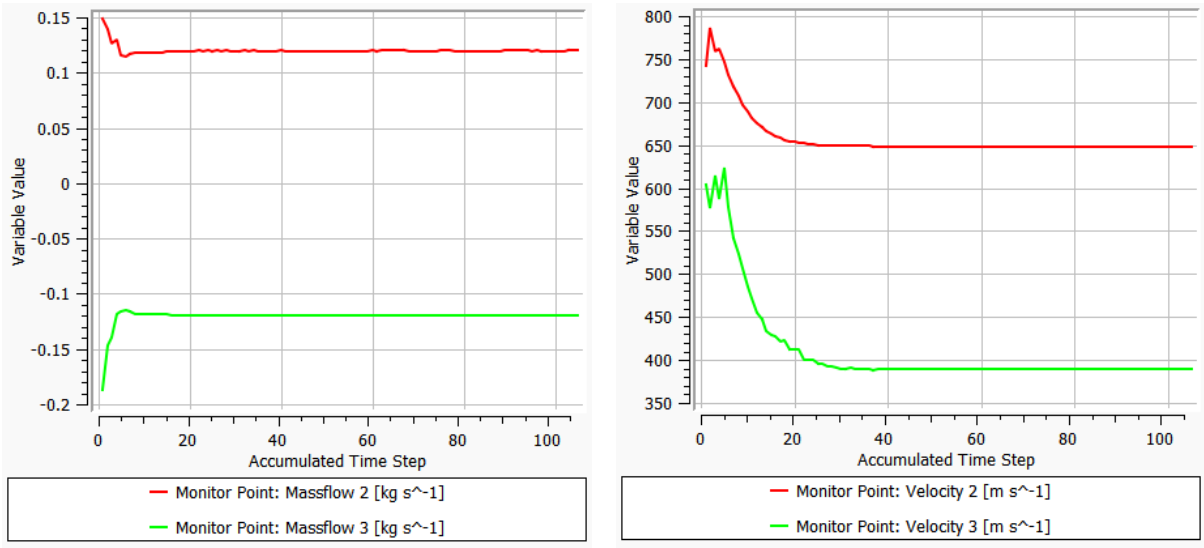


*Figure 6.16: Convergence of the mass flow (Left) and the velocities (Right) at the rotor inlet and outlet.*

### 6.4.4 Numerical results

The numerical results of the variables at the in and outlets of this simulation is presented in Table 6.10. Based on these numerical results, the specific work of the rotor can be calculated using Equation 6.2 and Equation 6.3 and the resulting shaft power can be found with Equation 6.4, leading to the derived results shown in Table 6.11.

$$\Delta h_{tt} = h_{t,2} - h_{t,3} \tag{6.2}$$

$$\Delta h_{ts} = h_{t,2} - h_{s,3} \tag{6.3}$$

$$P = \Delta h_{tt} \cdot \dot{m}_2 \tag{6.4}$$

It should be noted that Ansys provides different definitions of total variables depending on which reference frame is used. A variable that is listed as "Total" in Ansys is derived from the rothalpy value within Ansys. "Total in Stationary Frame" refers to the total variable based on the absolute velocity $v$, and "Total in Relative Frame" refers to the total variable based on the relative velocity $w$. As the 1D model calculates total values with respect to the absolute velocity, only the values in the stationary frame are currently relevant and shown in Table 6.10 and Table 6.12, these are also indicated with the subscript "Stn".

| Variable | | Symbol | 3D simulation | Unit |
|---|---|---|---|---|
| Inlet | Static pressure | $p_2$ | 78.79 | $MPa$ |
| | Total pressure (Stn) | $p_{t,2,Stn}$ | 90.69 | $MPa$ |
| | Static temperature | $T_2$ | 278.55 | $K$ |
| | Total temperature (Stn) | $T_{t,2,Stn}$ | 290.3 | $K$ |
| | Density | $\rho_2$ | 43.97 | $\frac{kg}{m^3}$ |
| | Velocity (Stn) | $v_{2,Stn}$ | 723.123 | $\frac{m}{s}$ |
| | Mass flow | $\dot{m}_2$ | 119.385 | $\frac{g}{s}$ |
| | Static specific enthalpy | $h_2$ | 3.9834 | $\frac{MJ}{kg}$ |
| | Total specific enthalpy (Stn) | $h_{t,2,Stn}$ | 4.25151 | $\frac{MJ}{kg}$ |
| Outlet | Static pressure | $p_3$ | 35.49 | $MPa$ |
| | Total pressure (Stn) | $p_{t,3,Stn}$ | 38.5 | $MPa$ |
| | Static temperature | $T_3$ | 245.97 | $K$ |
| | Total temperature (Stn) | $T_{t,3,Stn}$ | 251.76 | $K$ |
| | Density | $\rho_3$ | 27.87 | $\frac{kg}{m^3}$ |
| | Velocity (Stn) | $v_{3,Stn}$ | 439.47 | $\frac{MJ}{kg}$ |
| | Mass flow | $\dot{m}_3$ | 119.85 | $\frac{g}{s}$ |
| | Static specific enthalpy | $h_3$ | 3.18008 | $\frac{MJ}{kg}$ |
| | Total specific enthalpy (Stn) | $h_{t,3,Stn}$ | 3.28394 | $\frac{MJ}{kg}$ |

*Table 6.10: Overview of the numerical results of the 3D simulation.*

| Variable | Symbol | Real gas case | Unit |
|---|---|---|---|
| Specific work tt | $\Delta h_{tt}$ | 967570 | $\frac{J}{kg}$ |
| Specific work ts | $\Delta h_{ts}$ | 1071430 | $\frac{J}{kg}$ |
| Power | $P$ | 115.5 | $kW$ |

*Table 6.11: Derived results of the 3D simulation.*

### 6.4.5 Graphical results

Next to these numerical results, the flow behaviour can also be analysed visually. Each of the following figures below presents a certain flow property around a single blade element. Only the most relevant plots are shown in this section of the report, but a more extensive list of contour plots - for more variables and in multiple reference frames - is provided in Appendix B where the images are also presented in a larger format. For clarity, the direction of rotation is positive (counter-clockwise) around the Z-axis.

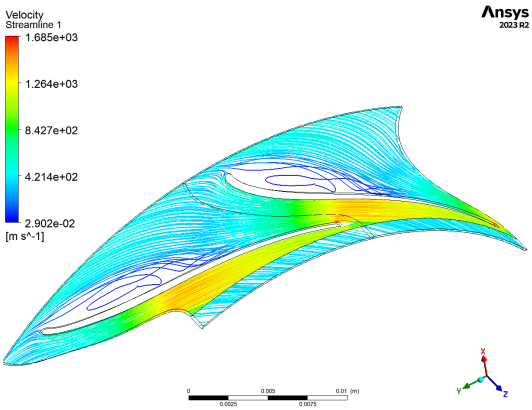


*Figure 6.17: Velocity streamlines relative to the rotor.*

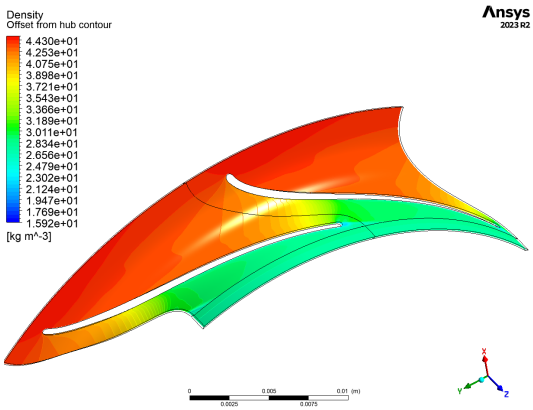


*Figure 6.18: Density.*

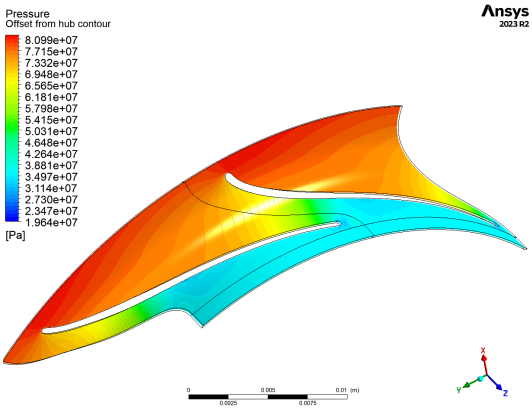


*Figure 6.19: Static pressure.*

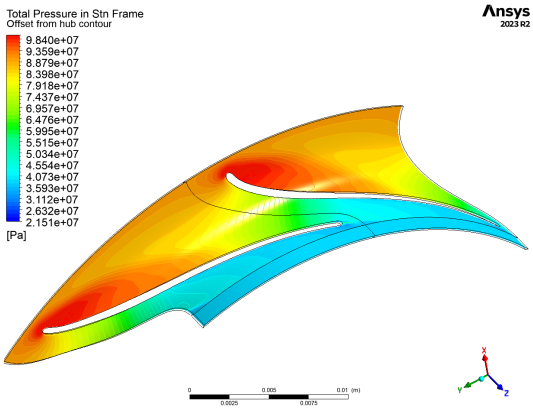


*Figure 6.20: Total pressure in the stationary frame.*

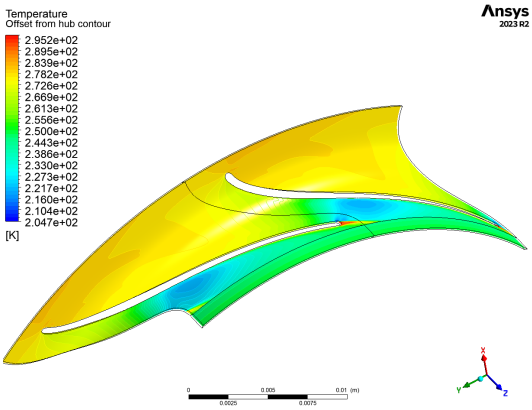


*Figure 6.21: Static temperature.*

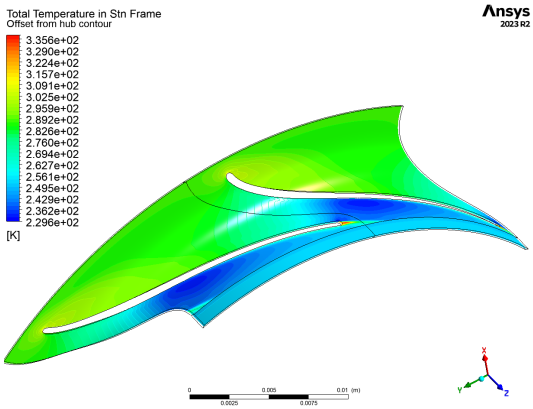


*Figure 6.22: Total temperature in the stationary frame.*

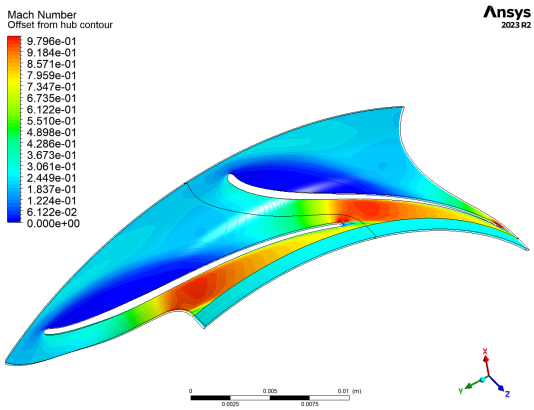


*Figure 6.23: Mach number.*

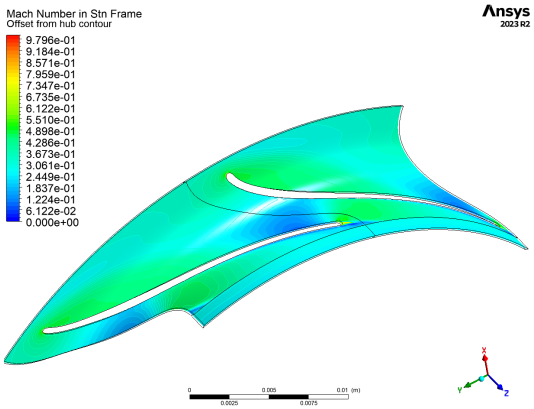


*Figure 6.24: Mach number in the stationary frame.*

Several observations can also be made with respect to these contour plots:

First, it is clear from the streamlines shown in Figure 6.17 that the flow separates near the leading edge on the pressure side rotor blade. This is also clearly visible in the plots of the Mach number and total pressure. This could potentially be resolved in a further design iteration by applying a slip correction by either adjusting the inlet angle of the rotor blade or by adjusting the absolute flow angle at which the flow enters the rotor domain. In practice, this would be achieved by changing the stator blades' outlet angle.

Secondly, a shockwave can be seen in the throat near the trailing edge of the blade. This is very prominently visible in Figure 6.23 but naturally also present in several other plots as a sudden change in velocity, pressure, temperature or density. This is as expected as the 1D model indicates that the flow is choked at the selected operating point.

### 6.4.6 Comparison to the 1D performance prediction.

Finally, this subsection aims to deliver a comparison between the results of the 1D and 3D models, respectively. As the 1D model has been built around the use of CoolProp to determine several state variables on the basis of a real gas model, it only makes sense to compare these results to a real gas simulation. Table 6.12, Table 6.13 present the numerical results of the main variables from the 3D model and provide a comparison relative to the results of the 1D model at the operating point. In this case, the change between the 3D model and the 1D model is presented according to Equation 6.5.

$$\%\ change = \frac{3D - 1D}{1D} \cdot 100 \tag{6.5}$$

Table 6.14 presents a comparison of the efficiencies of the 3D and 1D models. However, as the 3D simulation does not produce a value of the isentropic work but only the actual enthalpy values at the in- and outlet of the rotor, these are both calculated with respect to the specific isentropic work of the 1D model following Equation 6.6

$$\eta_{isen} = \frac{\Delta h}{\Delta h_{isen}} \cdot 100 \tag{6.6}$$

| Variable | | Symbol | 3D model | 1D model | Unit | % change |
|---|---|---|---|---|---|---|
| Inlet | Static pressure | $p_2$ | 80.49 | 69.77 | $MPa$ | 15.36 |
| | Total pressure (Stn) | $p_{t,2,Stn}$ | 90.05 | 90.09 | $MPa$ | -0.04 |
| | Static temperature | $T_2$ | 279.2 | 269.78 | $K$ | 3.49 |
| | Total temperature (Stn) | $T_{t,2,Stn}$ | 288.3 | 288.24 | $K$ | 0.02 |
| | Density | $\rho_2$ | 44.48 | 41.95 | $\frac{kg}{m^3}$ | 6.03 |
| | Velocity (Stn) | $v_{2,Stn}$ | 647.76 | 984.36 | $\frac{m}{s}$ | -34.19 |
| | Mass flow | $\dot{m}_2$ | 119.85 | 119.1 | $\frac{g}{s}$ | 0.63 |
| | Static specific enthalpy | $h_2$ | 4.00682 | 3.948098 | $\frac{MJ}{kg}$ | 1.49 |
| | Total specific enthalpy (Stn) | $h_{t,2,Stn}$ | 4.2173 | 4.432587 | $\frac{MJ}{kg}$ | -4.86 |
| Outlet | Static pressure | $p_3$ | 35.45 | 35.45 | $MPa$ | 0.00 |
| | Total pressure (Stn) | $p_{t,3,Stn}$ | 37.58 | 37.22 | $MPa$ | 0.97 |
| | Static temperature | $T_3$ | 249.05 | 257.14 | $K$ | -3.15 |
| | Total temperature (Stn) | $T_{t,3,Stn}$ | 253.31 | 260.83 | $K$ | -2.88 |
| | Density | $\rho_3$ | 27.55 | 26.66 | $\frac{kg}{m^3}$ | 3.34 |
| | Velocity (Stn) | $v_{3,Stn}$ | 389.25 | 364.03 | $\frac{MJ}{kg}$ | 6.93 |
| | Mass flow | $\dot{m}_3$ | 119.85 | 119.1 | $\frac{g}{s}$ | 0.63 |
| | Static specific enthalpy | $h_3$ | 3.22357 | 3.895723 | $\frac{MJ}{kg}$ | -17.25 |
| | Total specific enthalpy (Stn) | $h_{t,3,Stn}$ | 3.29956 | 3.961983 | $\frac{MJ}{kg}$ | -16.72 |

*Table 6.12: Overview of the numerical results of the 3D CFD simulation and a comparison to the results of the 1D model at the operating point.*

| Variable | Symbol | 3D model | 1D model | Unit | % change |
|---|---|---|---|---|---|
| Specific work tt | $\Delta h_{tt}$ | 917740 | 470604 | $\frac{J}{kg}$ | 95.01 |
| Specific work ts | $\Delta h_{ts}$ | 993730 | 536864 | $\frac{J}{kg}$ | 85.10 |
| Power | $P$ | 109.99 | 56.05 | $kW$ | 96.24 |

*Table 6.13: Overview of the derived results of the 3D CFD simulation and a comparison to the results of the 1D model at the operating point.*

Starting with the pre-defined variables, the total inlet pressure $p_{t,2,stn}$, total inlet temperature $T_{t,2,stn}$ and the outlet static temperature $T_3$, it can be seen that these are indeed completely aligned. Similarly, the mass flow is almost exactly spot-on, which makes sense as the wrap angle of the rotor blades has been tuned iteratively to match the throat area and thus restrict the mass flow.

As for the other flow variables, however, larger differences can be observed. At the inlet, it can be seen that the static pressure and density are overestimated and that the velocity is severely underestimated with respect to the 1D model. At the outlet, the total pressure seems to match more closely but both the static and total temperature are underestimated, the velocity and density, on the other hand, are overestimated. Again, with respect to the results of the 1D model.

These differences are also present in the enthalpy values and carry through to the calculation of the specific work and the power in Table 6.13. Here it can be seen that the 3D model predicts a power output that is almost double to what the 1D model finds.

These differences can also be observed in Table 6.14 where the efficiency of the 3D model is practically twice as high as that of the 1D model.

| Variable | Symbol | 3D model | 1D model | Unit |
|---|---|---|---|---|
| Specific isentropic work 1D tt | $\Delta h_{tt,isen}$ | - | 1190081 | $\frac{J}{kg}$ |
| Specific isentropic work 1D ts | $\Delta h_{ts,isen}$ | - | 1256341 | $\frac{J}{kg}$ |
| Isentropic efficiency tt | $\eta_{isen,tt}$ | 77.12 | 39.54 | % |
| Isentropic efficiency ts | $\eta_{isen,ts}$ | 79.10 | 42.73 | % |

*Table 6.14: Comparative efficiency results of the 3D CFD simulation and the 1D model with reference to the isentropic work of the 1D model at the operating point.*

With that knowledge, it is no surprise that the 3D model finds a higher velocity at the inlet and a lower velocity and lower temperatures at the outlet of the rotor. It predicts that for the given geometry and operating point, a lot more work can be extracted from the flow than what the 1D model finds thus a larger velocity and temperature difference exists between the in- and outlet of the rotor.

Thus, instead of focussing on the differences between the flow properties of both models, it might be more interesting to explore where this efficiency difference stems from which will be covered in Section 6.5.

## 6.5 Differences between the 1D and 3D model

As described in Subsection 6.4.6, there is a large difference in the performance predicted by the two models. This section will aim to reason where these differences come from based on known differences between the two models in Subsection 6.5.1 and Subsection 6.5.2 and finally Subsection 6.5.3 presents several other aspects which might be of influence but have not been investigated in detail.

### 6.5.1 Clearance losses

A first large difference between the two models are the losses that are taken into account. As described in Subsubection 5.2.1.2, one of the loss models that are taken into account in the 1D model are the clearance losses. As already shown in Subsection 6.3.3, these make up a significant part of the losses for the given design. In the 3D model however, these are not present as the boundary conditions create a shroud exactly at the blade height that rotates along with the domain.

Figure 6.25 presents the total to static efficiency of the rotor - between stations 2 and 3 - for the 1D model with and without the clearance losses taken into account. As can be observed, removing the clearance losses increases the rotor efficiency by ±35%. Of course this is still a simplification as a shrouded turbine would likely result in higher frictional losses which would need to be covered under the rotor passage losses but it does show how this correction drives the results a lot closer to each other.

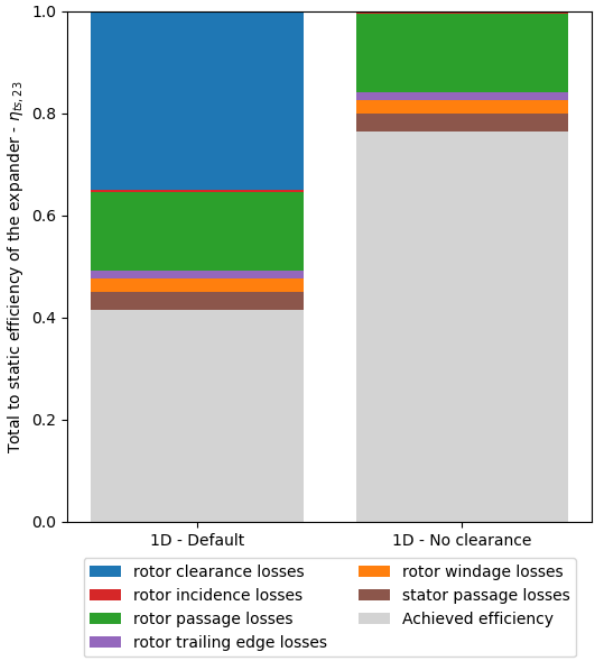


*Figure 6.25: The losses and total to static rotor efficiency of the 1D model with and without the clearance losses.*

This is also shown in Table 6.15 where the results of the specific work, the isentropic specific work and the isentropic efficiency results are shown for the 3D validation case, the 1D model results with clearance losses taken into account and the 1D model results without the clearance losses.

A suggestion for future work or improvements would thus be to model a rotor with a stationary shroud and an actual clearance between the rotor blades and the shroud which would present a closer approximation of a real design.

| Variable | Symbol | 3D model | 1D model: standard | 1D model: no clearance losses | Unit |
|---|---|---|---|---|---|
| Specific work tt | $\Delta h_{tt}$ | 917740 | 470604 | 927716 | $\frac{J}{kg}$ |
| Specific isentropic work 1D tt | $\Delta h_{tt,isen}$ | - | 1190081 | 1190081 | $\frac{J}{kg}$ |
| isentropic efficiency tt | $\eta_{isen,tt}$ | 77.12 | 39.54 | 77.95 | – |
| Specific work ts | $\Delta h_{ts}$ | 993730 | 536864 | 993976 | $\frac{J}{kg}$ |
| Specific isentropic work 1D ts | $\Delta h_{ts,isen}$ | - | 1256341 | 1246341 | $\frac{J}{kg}$ |
| isentropic efficiency ts | $\eta_{isen,ts}$ | 79.10 | 42.73 | 79.11 | – |

*Table 6.15: Comparison of the specific work and isentropic efficiency results of the turbine with and without clearance losses.*

### 6.5.2 Inlet domain specification

As introduced in Subsection 6.4.2, a second difference between the models is the fact that the diameter of the inlet domain of the 3D model has been increased from 49.44 mm to 52 mm. This does not affect the shape of the turbine itself as the blades follow the original geometry but it does change the location at which the inlet conditions are specified. For example, the specified inlet conditions are the total pressure in the stationary frame $p_{t2,stn}$ and the components of the absolute inflow angle $\alpha_3$.

As can be seen in Figure 6.26, both of these specified inlet conditions vary quite a bit between the inlet domain, where they are specified in the 3D model, and the actual rotor inlet diameter indicated in black. If the inlet conditions would be specified at the actual design diameter of the rotor this would surely have an effect on the results of the 3D simulation. However, the flow behaviour that can be seen around the leading edge on the right plot is a real effect that is also not taken into account in the 1D model. Thus if this were to be applied, it is difficult to say in which ways the results would be affected. An alternative solution could be to iteratively change the inlet conditions and monitor them at the design inlet diameter until they match the specifications of the 1D model.

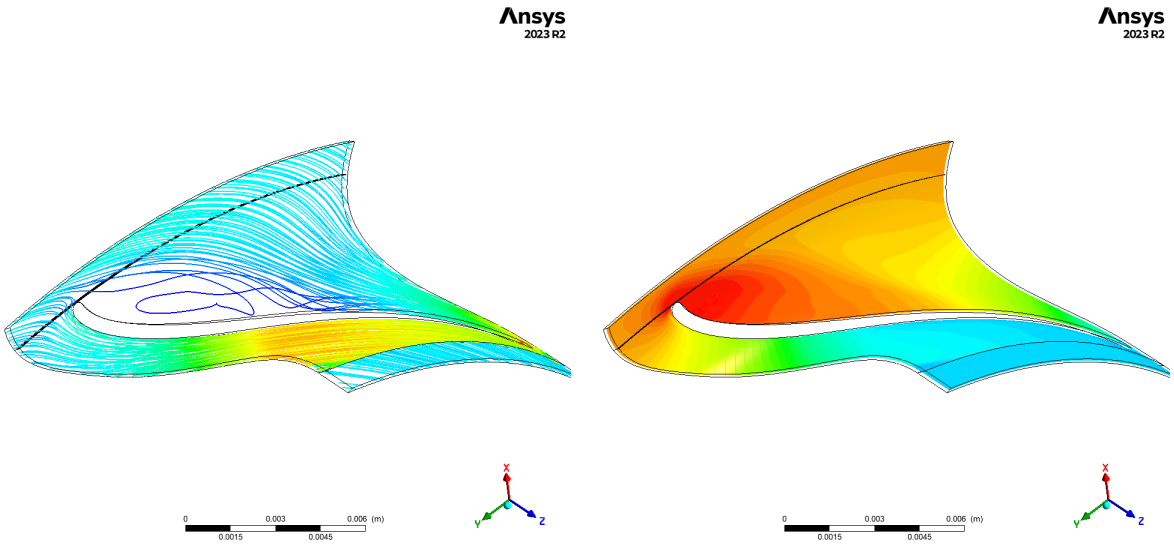


*Figure 6.26: The velocity streamlines (left) and the Total pressure in the stationary reference frame (right). With the inlet domain of the 3D model as the edge of the observed domain and the actual rotor inlet diameter as specified in the 1D model indicated in black.*

### 6.5.3 Other possible discrepancies

Lastly, there are several other aspects which have an influence on the results and could possibly be explored in any future work but fall out of the scope of this thesis. However, for the sake of completeness, they should still be mentioned.

A first aspect are the adopted loss models in the 1D model. These are adopted from the work of Gambini et al. [108] and should generally provide a very decent approximation of the losses in turbomachinery designs. However, they are also developed for more typical turbomachinery applications, which usually range from the size of turbochargers in automotive applications to the turbines found in industrial powerplants. This is in stark contrast with the current proposed design, where the design features such as the blade height and the flow areas are orders of magnitude smaller than any other commonly existing design. A very concrete example would be the estimation of the passage losses. Due to the very small blade height ($\pm 0.1$ mm), the aspect ratio of the passage is a lot higher than in other typical designs. This results in the ratio of the wetted surface area in the passage to the overall flow area to be very high which would logically increase the friction losses a lot. There are parameters in these loss models that take these dimensions and ratios into account, but there are also other constants or ratios included which might have empirically defined but are not particularly suited for this specific design. However, correcting or testing this hypothesised inaccuracy is deemed to be far outside of the scope of this work.

Secondly, there is the accuracy of the 3D model and the CFD simulation which could be questioned. Although a real gas model and very widely used system components have been used in Ansys, this application is again, not the most typical or standard design. The mesh for example has been refined to what was deemed to be an acceptable level but upon every design iteration, there was a constant struggle to create an error-free mesh. The default setting kept generating negative volumes. These have eventually been able to be resolved but at the cost of increasing the element size. Specifically in the direction of the blade height. This definitely limits the accuracy of the boundary layer. However, as the 3D model is not the focus of this thesis itself and just a validation case, this was considered to be good enough as a full study into the most accurate modelling of the boundary layer and turbulence effects of a hydrogen-fuelled turbine in Ansys could be an entire thesis subject on its own.

## 6.6 Overall impact of integrating a turboexpander in an HRS

This section will aim to assess the overall impact of integrating the proposed turboexpander in a hydrogen refuelling station based on the results of the 1D model. First, Subsection 6.6.1 will address the changes it introduces to the refuelling process itself and the overall operation of a refuelling station. Next, Subsection 6.6.2 will reiterate the energy recovery that stems directly from the turboexpander itself, and Subsection 6.6.3 will quantify the secondary energy savings that are realised in the pre-cooling system of the station. Finally, Subsection 6.6.4 will provide an assessment of the resulting cost savings.

### 6.6.1 Effect on HRS operation

Before comparing the results of the refuelling process to that of other existing refuelling stations or models thereof, a few important differences should be reiterated.

- To start, the capacity of the buffer tanks has been set rather arbitrarily because of the

lack of a substantiated standard. The current volume of $5m^3$ allows for sufficient capacity to allow for a few back-to-back refuelling cycles without the need to re-compress hydrogen whilst being small enough to notice the variable inlet pressure to the turbine.

- Second, the maximum allowable mass flow (120 g/s) is significantly higher than what is currently used in existing refuelling stations for automotive applications (maximum 60 g/s). This is substantiated by a research project under the Horizon 2020 Work program of the European Commission [128], which states the existence of this flow limit in Medium- and Heavy-Duty refuelling protocols and proposes to further investigate the applicability of it for broader applications. It is further reasoned that the main reason for this limit - excessive temperature rise upon fast expansion through an isenthalpic valve - is not present as work is being extracted from the gas.
- Thirdly, as the increased mass flow through the system resulted in a very fast filling procedure for a "standard hydrogen vehicle" with a tank capacity of 5 kg, the assumed vehicle capacity has been increased to 10 kg. In reality, this capacity would be found in light goods vehicles such as box trucks or vans as opposed to passenger cars, for example. The main practical reason for this change, however, was to retain a sufficiently high resolution in the results of the system model. As it is built around 1-second time steps, a much shorter refuelling cycle would have led to a lack of detail.

Taking these differences into consideration, the following figures show the differences in mass flow, vehicle tank pressure and vehicle tank temperature over time between a typical refuelling cycle and the one modelled in this thesis. Figure 6.27 shows the literature reference on the left, and Figure 6.28 shows the obtained results from the 1D model on the right.

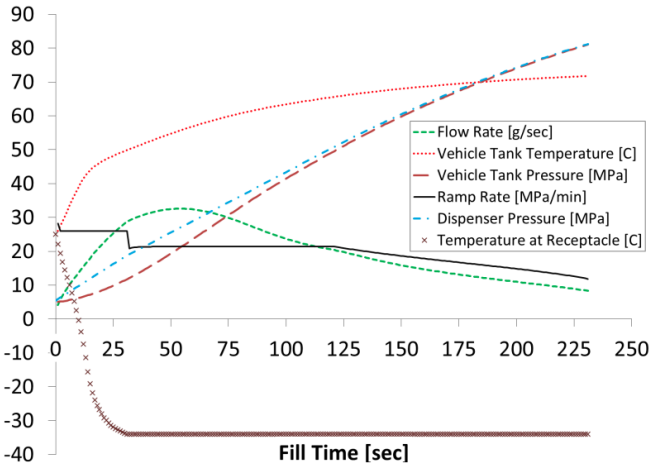


*Figure 6.27: Typical HRS system model results from a reference study by Reddi et al. [129]*

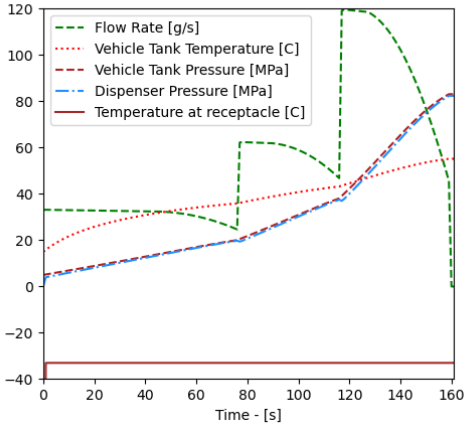


*Figure 6.28: System model results of an HRS with a turboexpander.*

### 6.6.2 Energy recovery from compressed hydrogen

As previously shown in Section 6.3, Figure 6.12 presented the results of the shaft power of the turbine and the total recovered energy based on the turbine losses. However, what has not yet been taken into account are the losses associated with converting this shaft power to electrical energy. In order to estimate this, a fixed generator efficiency and a fixed motor controller efficiency will be assumed. However, for this, the rotational speed at which the generator should operate should be considered.

As explained in Subsection 4.3.4 and shown in Equation 5.7, the tip speed of the rotor is a result of a presumed work coefficient $\Phi$ and the isentropic work of the expander $\Delta h_{tt,isen}$ at a certain time step, which, as shown in Section 6.3, varies over time. Thus, for a given diameter, this tip speed results in a varying rotational speed of the rotor as shown in Figure 6.29.

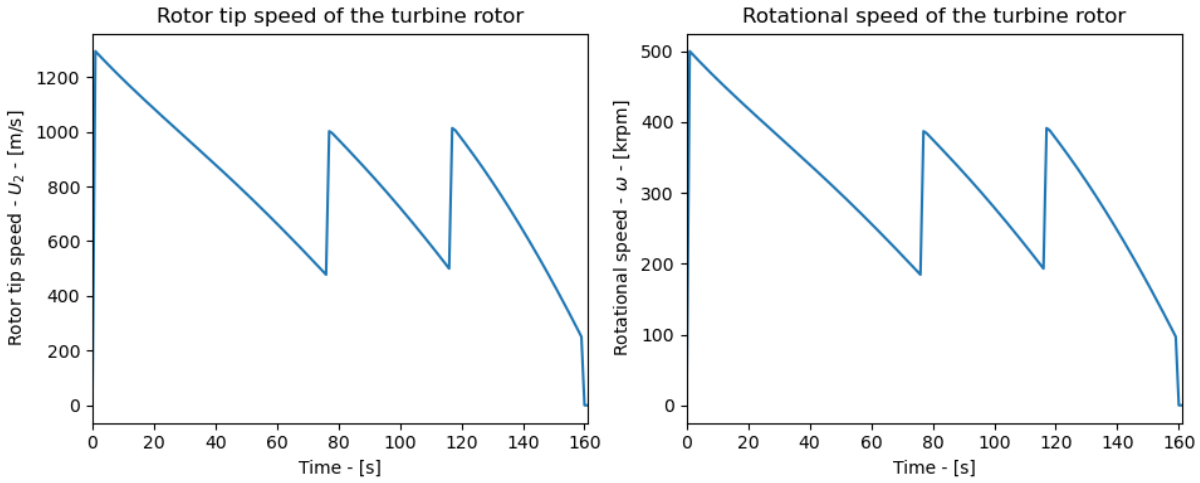


*Figure 6.29: Tip speed $u_2$ (Left) and rotational speed $\omega$ (Right) of the turbine rotor.*

As can be seen in Figure 6.29, the previously defined maximum rotor speed of 500,000 rpm is only required when trying to operate the rotor at the proposed work coefficient and only at the very start of a refuelling cycle. Hence, it would be unreasonable to base the expectations of the generator's performance on this value alone.

Upon researching generators or motors for high-speed applications, most references came back to one of two applications, either micro gas turbines or spindles for micromachining (e.g. electronic circuits). In academic literature, the most relevant publication around this topic appears to be the work by Zwyssig et al. (2009) [130], which presented a comprehensive overview of other work on the topic of "Megaspeed Drive Systems" and the actually achieved results opposed to just the design specifications. For example, it lists 200 W electric PCB drills that operate at 230,000 rpm, electric dentist drills with internal gear systems that achieve up to 200,000 rpm and microturbine designs from Epstein et al. [131] designed to operate at 1.2 million rpm. However, it also addresses the low power output of these designs and concludes that for up to 100,000 rpm, plenty commercially available motors and generators are available. For speeds between 100,000 rpm and 250,000 rpm, specialist industrial drives are available and above 500,000 rpm, there are only research projects ongoing. However, as this paper is already 15 years old, some of the mentioned industrial companies were also looked into and the following four references were also considered:

- e+a (Electromashinen und Antriebe) has several commercially available electromotors which are able to achieve speeds of up to 300,000 rpm [132].
- e+a also refers to achieved speeds of up to 500,000 rpm, delivering 1.3 kW in several other pages and brochures [133, 134, 135].
- Calnetix technologies does have a mention of electric motors and generators that can achieve speeds of up to 450,000 rpm [136]. Unfortunately, no further information is provided.
- ate-system does refer to induction motors that can achieve up to 300,000 rpm and synchronous DC motors and micro-drives that can achieve up to 1,000,000 rpm [137].

- Celeroton currently offers several high-speed motors. One of which is rated up to 500,000 rpm and a power of 100W, another one to 280,000 rpm and 1,000 W and a last one up to 250,000 rpm and 2,500 W [138].

Based on these findings, the technological development between 2009 [130] and 2024 [136, 137, 138] and the assumption that the technology of electric motors translates to electric generators, it is considered that a high-speed generator capable of operating at speeds around 350,000 rpm with reasonable efficiencies is realistic in the foreseeable future. It is also assumed that these systems can be scaled up to cover the power generated by the turbine design. Unfortunately, however, none of the sources relating to these available motors or generators list the efficiency of these products, but electric motors are known to reach efficiencies of 90 - 95% at their design point.

As an alternative to an assumed ultra-high-speed generator rated for such a high power, one could also consider the combination of a slower spinning generator with a gearbox. In this case, the generator itself could be assumed to achieve much higher efficiencies, but additional losses would need to be accounted for in the gearbox.

Given the extremely high rotating speeds, it is assumed that both a generator or a gearbox would operate near the limits of their operating envelopes and would thus likely not perform at an optimal efficiency furthermore, the efficiency would likely vary throughout a refuelling cycle as both the rotational speed and the shaft power vary over time. Thus, without more specific constraints, it is unreasonable to assume a fixed efficiency. Instead, an efficiency range between 50% and 90% has been assumed. These boundaries are set on the assumption that an efficiency higher than 90% is unlikely given the extreme operating point. Although efficiencies lower than 50% would technically be possible, these would be highly unfavourable and, in the author's opinion, better alternatives should be looked for if this lower limit cannot be achieved.

Adding this range of losses, Figure 6.30 presents the final electric power and recovered energy of the system, including a generator. This ultimately leads to a total amount of recovered electric energy ranging between **0.586 kWh** and **0.325 kWh** a peak electrical power output between **45.4 kW** and **25.23 kW**.

This can be compared to the work done by Chen et al.[31], who found a peak power of 30.44kW and a total amount of recovered energy from the expander of $\pm$ 0.8 kWh. At first sight, these results appear vastly different as the predicted recovered energy is half of what Chen et al. found but the peak power is a lot closer. However, considering that the peak power is achieved at the peak mass flow and that the peak mass flow assumed in this thesis is double to that of what Chen et al. assumed, we can scale our results. If we were to assume the same peak mass flow as Chen et al., both the peak shaft power and the recovered energy would be half of what Chen et al predicted. A difference nonetheless but a consistent difference. However, similar to the comparison of the 3D model results, we can look at the estimated efficiency. Indeed, Chen et al. assumed an efficiency of 60% which is quite a bit higher than what has been found using the loss models. If a similar efficiency would have been assumed, the results would actually align quite well. However, another difference between the two studies should be highlighted as Chen et al. assumed a single cascade system in which all the hydrogen is expanded from the high-pressure buffer tank to the vehicle instead of the three buffer tanks assumed in this thesis. This logically leads to different results when estimating the total amount of energy that can be recovered or which is needed by the station itself.

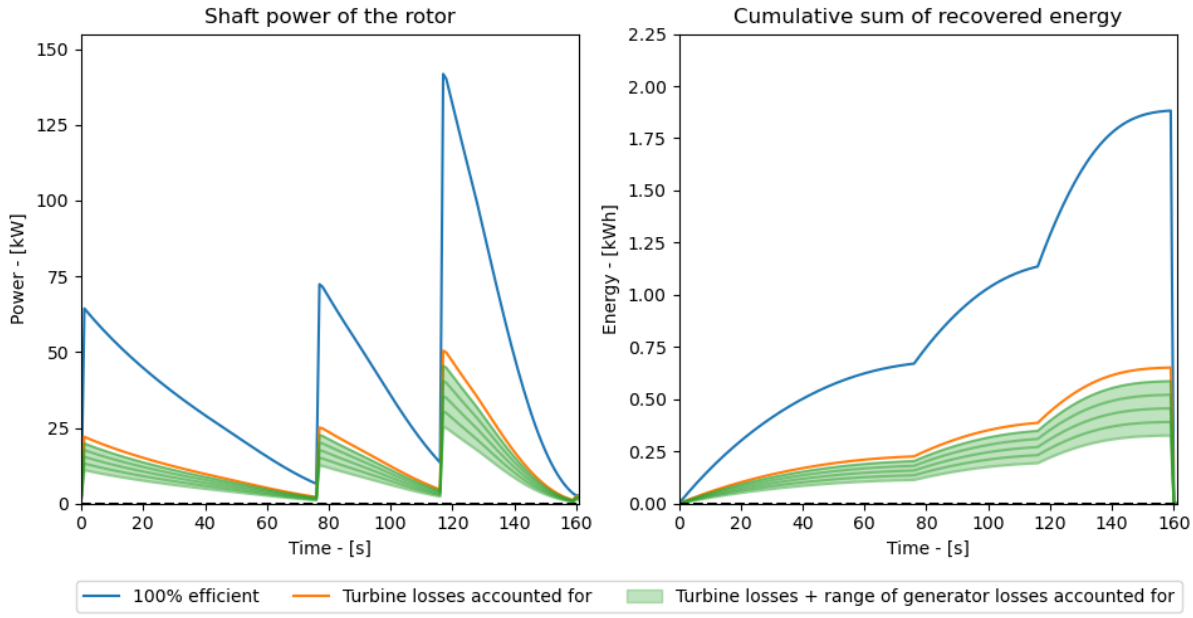


*Figure 6.30: Power (Left) and cumulative sum of recovered energy (Right) for a 100% efficient design (Orange), the turbine with turbine losses accounted for (Blue) and the turbine with a 70% efficient generator (Green).*

### 6.6.3 Energy saving from expansion cooling

As already explained in various sections of this thesis, expanding hydrogen through a turboexpander generally leads to a cooling effect as opposed to the more common practice of expanding it through an isenthalpic valve which, due to the negative Joule-Thomson coefficient of hydrogen, would lead to additional heating. Similar to the traditional system, the newly proposed one with a turboexpander still requires a heat exchanger to pre-cool the gas before it enters the vehicle tank. But as the inlet temperature to the pre-cooler is already lower, so should its energy consumption be. This subsection aims to identify how much energy can be saved with respect to a traditional system, as the study by Chen et al. [31] predicted that this could be equally large to the recovered energy from the expander itself.

For the current system model, the energy consumption of the pre-cooler can be calculated using the same equations as used in the reference study:

$$W_{cool} = \frac{Q_{cool}}{COP} \tag{6.7}$$

With the $COP$ (Coefficient of Performance) and the cooling demand $Q_{cool}$ defined as follows:

$$COP = 1.6 \cdot e^{-0.018 \cdot T_{amb}} \tag{6.8}$$

$$\begin{aligned} Q_{cool} &= \dot{m} \cdot (h_{cool,in} - h_{cool,out}) \\ &= \dot{m} \cdot (h_4 - h_5) \end{aligned} \tag{6.9}$$

When applied to the current system model, this results in the cooling demand and pre-cooler power requirement shown in Figure 6.31. As can be observed, the peak power requirement of the pre-cooler would be **44.70 kW** and its total energy consumption is equal to **0.87 kWh** per refuelling cycle.

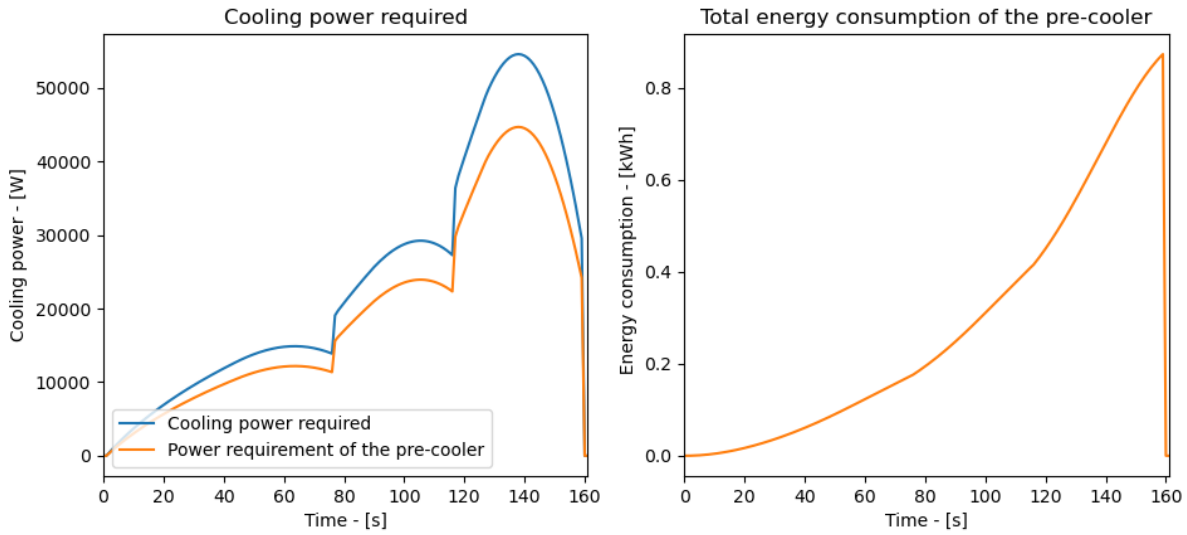


*Figure 6.31: Cooling power required and the power requirement of the pre-cooler over time (Left) and the total energy consumption of the pre-cooler during a single refuelling cycle (Right).*

The energy saved with respect to a traditional system is slightly more difficult to estimate as no traditional expander valve has been modelled for this thesis. Comparison to other research data is possible, but it should be kept in mind that the pressure levels of the buffer tanks and the profile of the mass flow during a refuelling cycle are very different. Instead, it has been chosen to adopt an average outlet temperature of a would-be expansion valve and calculate the required cooling energy for that in the current system. From Elgowainy et al. [139], we can adopt an average expander outlet temperature $T_4$ of 40°C.

Assuming this value and calculating the energy and power requirements of a pre-cooler for the mass flow in this study, we find a total pre-cooler energy consumption of 2.18 kWh and a peak power requirement of 105.76 kW. Resulting in a direct energy saving of **1.31 kWh** per refuelling cycle.

### 6.6.4 Economical assessment of applying a turbo-expander in an HRS

As shown in Subsection 6.6.2 and Subsection 6.6.3, implementing a turboexpander as a recovery device can lead to 0.456 kWh of recovered energy (Assuming 70% generator efficiency - in the middle of the proposed range) and 1.31 kWh of saved energy per refuelling cycle of 10 kg. Equating to an average of 0.1766 $\frac{kWh}{kg}$ of hydrogen. This can be compared to the results from Chen et al.[31], who found an energy saving of 1.647 kWh per 7 kg or 0.234 $\frac{kWh}{kg}$ of hydrogen refuelled.

Using the average industrial electricity price in Europe in 2023, €0.1347/kWh [140], this results in a cost reduction of €0.02378 per kg of hydrogen.

Applying this to a utilisation rate of 500 - 1000 kg/day [141, 142, 143] leads to anywhere between €11.89 and €23.78 saved per day in operational costs or €4,339.85 to €8,679.9 per year per refuelling station.

At first sight, these numbers might appear almost irrelevantly low considering the scale of a refuelling station on an annual basis, but it should be kept in mind that this is a purely operational cost saving and should not be compared to the cost of the fuel itself. When comparing the sum

of saved and recovered energy to the operational energy expenditure of an HRS, the comparison becomes more tangible. Bauer et al. [144], for example, found a total energy consumption of 2.43 $\frac{kWh}{kg}$ for a traditional refuelling station with 3 buffer tanks. Compared to that, the current results of 0.1766 $\frac{kWh}{kg}$ indicate a 7.36% reduction in the operational energy consumption of an HRS.

In addition to this, two other aspects can potentially lead to significant cost savings and are mentioned in the available literature. However, both of these rely on very broad assumptions that go beyond the scope and focus of this thesis and will, therefore only be described superficially.

- First, Elgowainy et al. [139] refers to significant additional energy costs relating to the pre-cooling system of a traditional HRS, specifically when it is underutilised. This is because large pre-coolers typically require a large block of thermal mass that needs to be kept cool continuously in order to be able to provide a sufficiently fast cooling response when a refuelling process takes place and in order to be able to handle multiple back-to-back refuelling cycles without requiring a break. When an HRS is underutilised, and this pre-cooler sits idle, it leads to significantly higher cooling costs per kg of hydrogen refuelled. Although this is also true when a turboexpander system is applied, the total cooling demand of the pre-cooler would be reduced, and by extension, so would the requirement of these fixed cooling costs.
- Secondly, previous work on the integration of a turboexpander in an HRS has also theorised values for the difference in infrastructural cost and development costs between a system with and without a turboexpander. For example, Chen et al. referred to an infrastructure cost saving of ±€210,000 [31] and Yoshida et al. concludes with ±50% savings on the machine cost, 14% savings on the construction of the station, 64% savings on maintenance and 13% savings on operational costs.

## 6.7 Sensitivity study of parameters

Observing the results thus far, in particular, the assumed rotational speed and the calculated rotor inlet blade height, it is clear that the proposed design would be difficult to produce and operate in practice. Because of this, a limited sensitivity study has been performed in which several assumptions and design parameters have been varied to observe their effect on the design and its performance. Specifically, their impact on the rotor inlet blade height and the calculated efficiency has been monitored to observe which changes would result in either a more feasible geometric design or a higher energy recovery.

The parameters that have been varied are:

- The mass flow through the system.
- The maximum allowable rotational speed of the rotor.
- The flow coefficient.
- The work coefficient.

Please note that the presumed isentropic rotor, stator and overall expander efficiencies, which are used as an input to the system model, are not altered. Thus every design variation shown below could be tweaked further by matching the assumed isentropic efficiency with the actual performance after analyzing the losses if they were to be analyzed individually. This is especially

visible in the plots where the flow and work coefficients are varied. If these are increased beyond the range shown in the relevant plots, they would result in NaN or Inf values. This can always be traced back to a calculation in which CoolProp is used to determine the value of a certain variable for the given input. A solution to this will be explored in the recommendations section of this report.

### 6.7.1 Variation of mass flow

As previously described in Subsection 6.1.1, the system model assumes a corrected mass flow rate which corresponds to a maximum mass flow rate of 120 g/s, which is already twice as large as currently used protocols for traditional vehicles. The reasoning for this was that a maximum mass flow rate of 60 g/s would have led to an even smaller and less plausible design but that mass flow rates of up to 120 g/s have been suggested as an upper limit for heavy-duty refuelling protocols - typically meant for heavy-duty vehicles such as trucks, busses and heavy machinery as opposed to passenger cars for example. However, when considering aerospace or naval applications, one could imagine the need for even higher mass flows.

With this reasoning, the assumed corrected mass flow rate has been varied and scaled between a range of 0.5 and 10 times the original value, correlating to maximum mass flow rates of approximately 60 g/s and 1,200 g/s. In order for the model to operate accordingly, the same scaling factor has been applied to the capacity of the buffer and vehicle tanks as well as the cross-sectional area of the pipes in the system model.

The results are visualised in Figure 6.32. The left subplot shows the results of the calculated rotor inlet blade height in millimeters, and the right plot shows the calculated total to static efficiency of the expander based on the loss calculations. In both charts, the data point relating to the original variable values is indicated through highlighted datapoint and the black dashed lines.

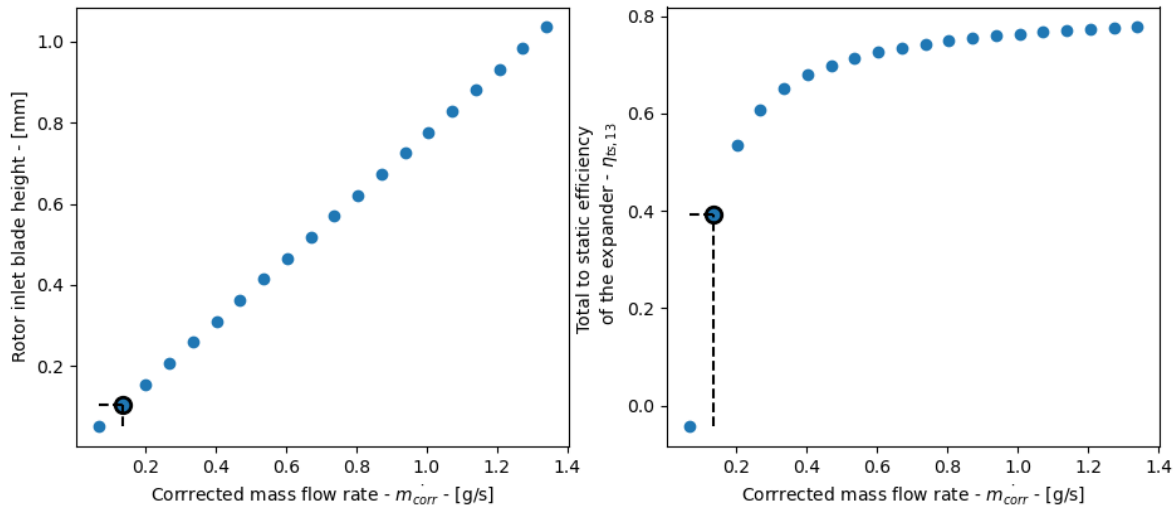


*Figure 6.32: Rotor inlet blade height (Left) and Efficiency (Right) for a variation of the corrected mass flow rate as an input to the system model.*

As can be observed, the rotor inlet blade height does indeed increase linearly for a varying mass flow rate through the system - keeping in mind that apart from the tank capacity and pipe diameters, everything else remains constant. This is as expected as the rotor diameter is a direct result of the assumed maximum rotational speed and of the isentropic work, which in

turn is a result of the expansion ratio, neither of which is affected by a scaling of the system. It makes sense that, for the same pressures and temperatures, a higher mass flow rate results in a larger inflow area to the rotor, which for a constant rotor inlet diameter would indeed lead to a taller blade height.

When looking at the efficiency results on the right, it can be observed that an upscaling of the system also leads to improved efficiency. As shown in Figure 6.33, this can mainly be attributed to the clearance losses. As the rotor blade height increases but the tip clearance remains the same, the relative portion of the flow that is affected by the interaction between the blade tips and the shroud becomes smaller, leading to less relative spill-over and reduced losses. The same mechanism seems to apply to the rotor windage losses which show a similar trend. The stator passage losses can also be seen to reduce significantly, which can be expected as the height of the stator passage increases with the blade height of the rotor. The incidence and trailing edge losses also appear to be reduced for higher mass flows, but this has a less significant impact on overall performance. In fact, the only loss mechanism that remains more or less constant are the rotor passage losses. These results are also in line with what has previously been observed in analysing the efficiency and related losses for different design points in Subsection 6.3.1.

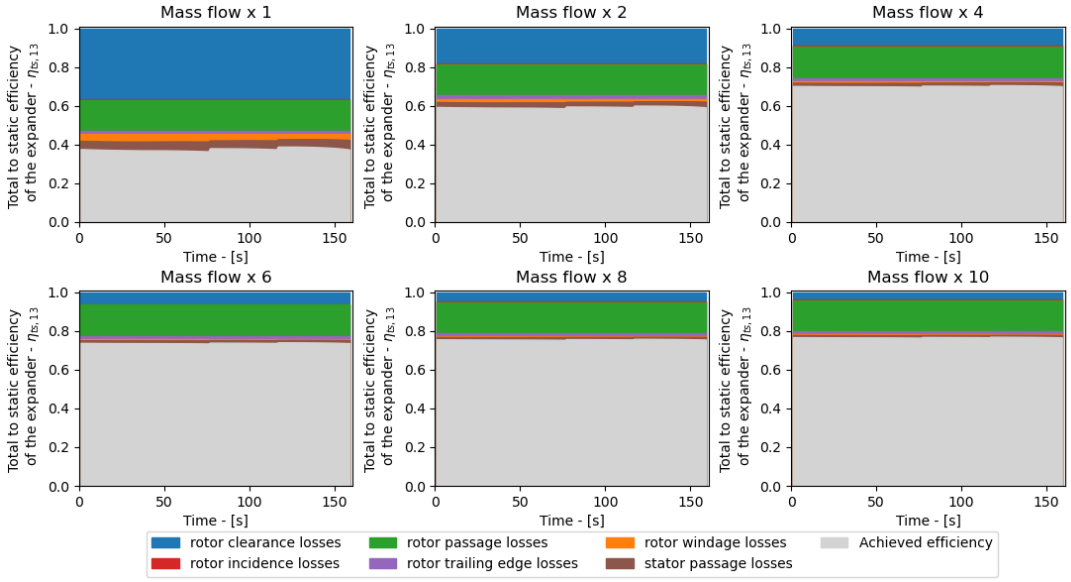


*Figure 6.33: Overview of the contribution of each loss model to the overall efficiency of the turbine for varying mass flow rates through the system.*

### 6.7.2 Variation of maximum rotor speed

In a similar fashion, the design assumption that the maximum allowable rotational speed of the expander is 500,000 rpm has also been varied. As explained before, this value had initially been set as a trade-off between what is technically achievable, what has been assumed in previous studies and what leads to a not-completely-impossible rotor inlet blade height.

The rotor speed has again been varied by applying a factor to the original value, which ranged from 0.6 to 1.5. The results can be observed in Figure 6.34 where again, the left chart indicates the influence on the rotor inlet blade height and the right chart shows the efficiency results. The original data point is again highlighted through the dashed lines.

At first sight, one can observe that the results appear similar to those shown in Figure 6.32 but in

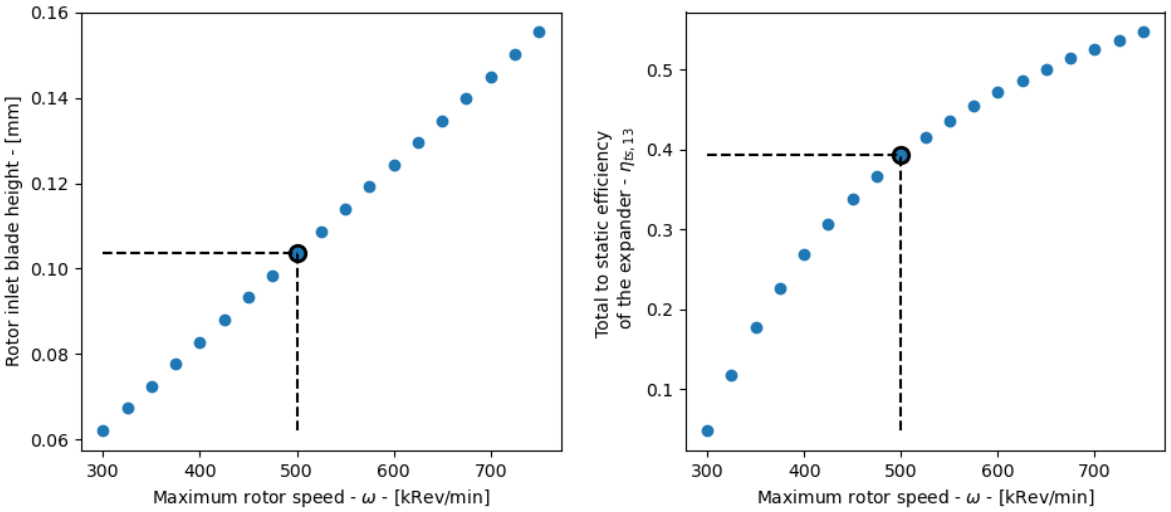


*Figure 6.34: Rotor inlet blade height (Left) and Efficiency (Right) for a variation of the maximum rotor speed as an input to the system model.*

this case the reasoning works in the other direction. As all other variables remain constant, every point shown in Figure 6.34 relates to the same rotor tip speed, $u_2$. Following Equation 5.10, one can see how a reducing rotor speed results in an increasing rotor diameter. As again all other input parameters remain constant, this increased rotor inlet diameter leads to a reduced rotor inlet blade height. Following the same reasoning as presented in Subsection 6.7.1 this logically results in higher losses and lower overall efficiency.

This again highlights the trade-off that should be made between selecting an achievable rotor speed and rotor blade height that is both manufacturable and sufficiently tall to minimize losses.

It is interesting to realise that an increase in the mass flow rate - and by extension an increase in the overall system size - and a reduction of the rotor speed result reflect on the performance through the same mechanisms but with opposing effects. This means that the downsides of a lower rotor speed could possibly be mitigated by, for example, increasing the mass flow through the system.

### 6.7.3 Variation of the flow and work coefficients

The last values that have been varied are the flow and work coefficient. As presented in Section 6.1, the values that were used for either of these parameters have been defined according to a performance comparison chart of different radial inlet turbines shown in Figure 5.2 [115]. However, these initial estimates are merely a prediction based on the performance of traditional gas turbines which operate on (hot) air mixtures as opposed to high-pressure hydrogen in the current application. Therefore, it makes sense to analyse how much the performance changes if we move away from this initial assumption and which effects this has on the turbine design and performance.

First, the effects of varying the flow and work coefficient independently will be shown, after which a combination of the two will be presented, leading to a similar chart as shown in Figure 5.2.

To start, the flow coefficient was varied by applying a factor to the original value, which ranged between 0.45 and 1.7. The results of this can be seen in Figure 6.35. As is visible from the

right chart, the initial value is indeed quite close to what is found to be the optimum efficiency point. However, the left chart appears to indicate that a lower flow coefficient would be more favourable if the aim is to increase the blade height of the turbine. This can be coupled back to the calculations shown in Figure 5.4 and Figure 5.5. If everything else remains constant, a lower flow coefficient would yield a lower meridional flow speed $v_{2,m}$ which, for the same mass flow and rotor diameter, would result in a larger inflow area of the rotor $A_2$ and a larger blade height $b_2$

It can also be observed that the datapoints on the right chart do not follow a smooth shape but instead, several "steps" can be observed, these are highlighted by the colours of the individual data points. Each of these steps correlates to a change in the number of rotor or stator blades, the results of which are rounded to the nearest integer and eventually lead to a discrete change in efficiency between design variations. In order to visualise this, the colour of the individual data points relates to the number of rotor blades in that design variation. Please note that the colour coding is consistent between all the graphs presented in this entire section.

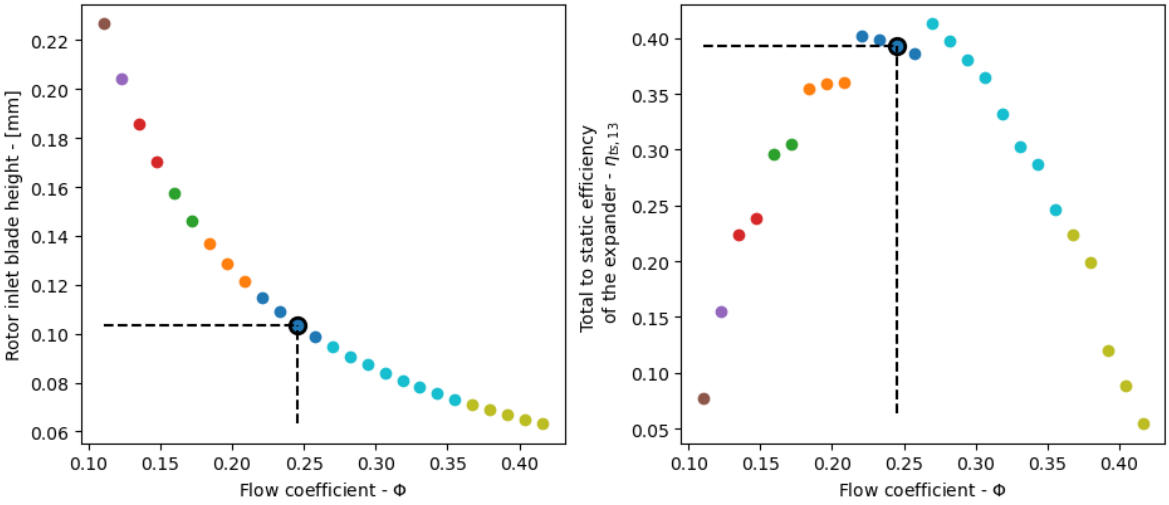


*Figure 6.35: Rotor inlet blade height (Left) and Efficiency (Right) for a variation of the flow coefficient as an input to the system model.*

Next, Figure 6.36 displays a similar variation of the work coefficient. The range of the factor applied to the initial guess was limited between 0.75 and 1.8 to avoid results that led to negative efficiency values or NaN or Inf values.

In this case, it can be observed that an increase of the work coefficient would result in both a higher efficiency and a larger rotor inlet blade height which falls in line with what could be expected after observing the results relating to varying the mass flow and rotor speed. If all the other conditions remain equal, a larger work coefficient will, for the same expansion ratio or for the same specific isentropic work, lead to a lower tip speed. Combined with the same rotor speed, this leads to a smaller rotor diameter, which for the same flow properties, leads to an increased blade height and a less shallow passage between the hub and the shroud of the rotor.

Similar to the variation of the flow coefficient, these results also show how the model predicts a different amount of rotor blades.

As both the flow and work coefficient are two parameters that have a large influence on the design and performance of the turbine, irrespective of its application, an attempt has been made to analyse the results when both are combined. The results of this can be seen in Figure 6.37

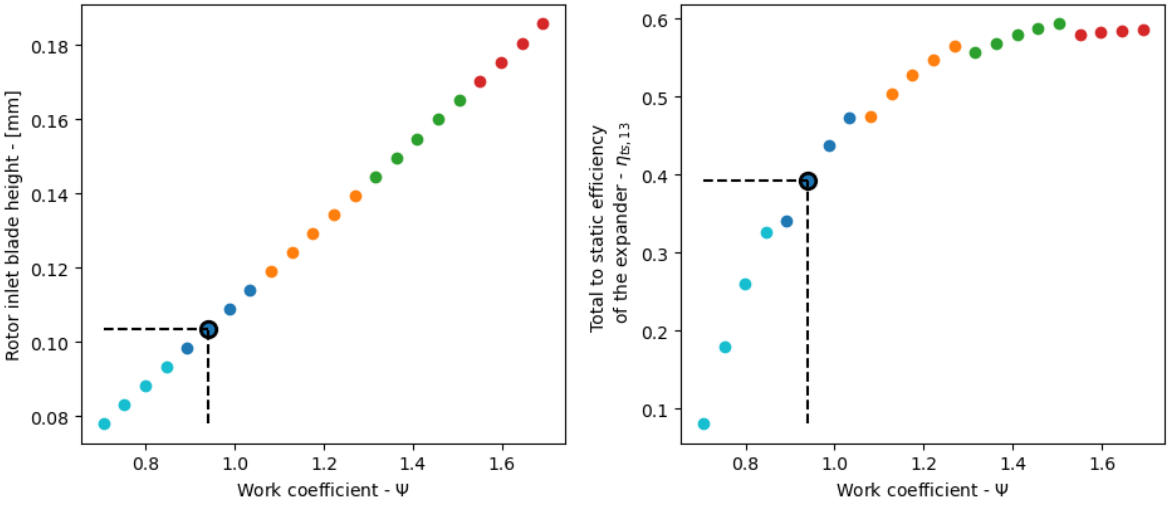


*Figure 6.36: Rotor inlet blade height (Left) and Efficiency (Right) for a variation of the work coefficient as an input to the system model.*

where the value of the flow coefficient is shown on the x-axis and the value of the work coefficient on the y-axis. The result of either the rotor blade height or the efficiency are indicated by the colour map in their respective charts, and again, the colour of the individual data points is indicative of a different number of rotor blades.

Considering that both the flow and work coefficients were changed, a larger range of variations could also be tested; In this case, the flow coefficient is varied between 0.3 and 2.4 times its original value, and the work coefficient between 0.3 and 1.9, both in intervals of 0.1. But, as can be observed from the empty areas (without data points) of the graphs, for certain combinations, the model still fails to compute. This can usually be traced back to points where CoolProp fails to predict the density in station 2, between the stator outlet and the rotor inlet, which leads to a series of divisions by zero and corresponding "NaN" or "Inf" values.

The origin of this problem lies in the fact that some inputs to the model have been manually iterated to match the results, such as the assumed efficiency value and the efficiency results after the loss calculations. Similarly, the design point has been defined by hand after observing the results shown in Figure 6.8. As this sensitivity study is performed completely automatically in a separate script, it was not possible to iterate on these as well. The lack of results at certain points simply shows that the discrepancy between these initial values and the outcomes of each variation becomes too large, leading to numerical results that are physically not possible and thus errors. That being said, these discrepancies also apply to the points at which values are found. In general, in this sensitivity study, the further away a datapoint point is from the initial value, the larger its potential error could be.

Although Figure 6.37 is just a combination of the two previous figures, it helps in identifying a possibly improved design point that would not only increase the efficiency of the turbine but also improve the feasibility of the design by resulting in a design that features less impossible machining tolerances. Indeed, a flow coefficient that is 10 - 20% larger and a work coefficient that is 70% larger would, by first approximation, result in a design that is ±20% more efficient and features a rotor inlet blade height that is 0.04 - 0.05 mm larger. "By first approximation" because, as described in Subsection 6.1.1, several variables have been determined iteratively for the original flow and work coefficients and are assumed constant in these variations. Examples are:

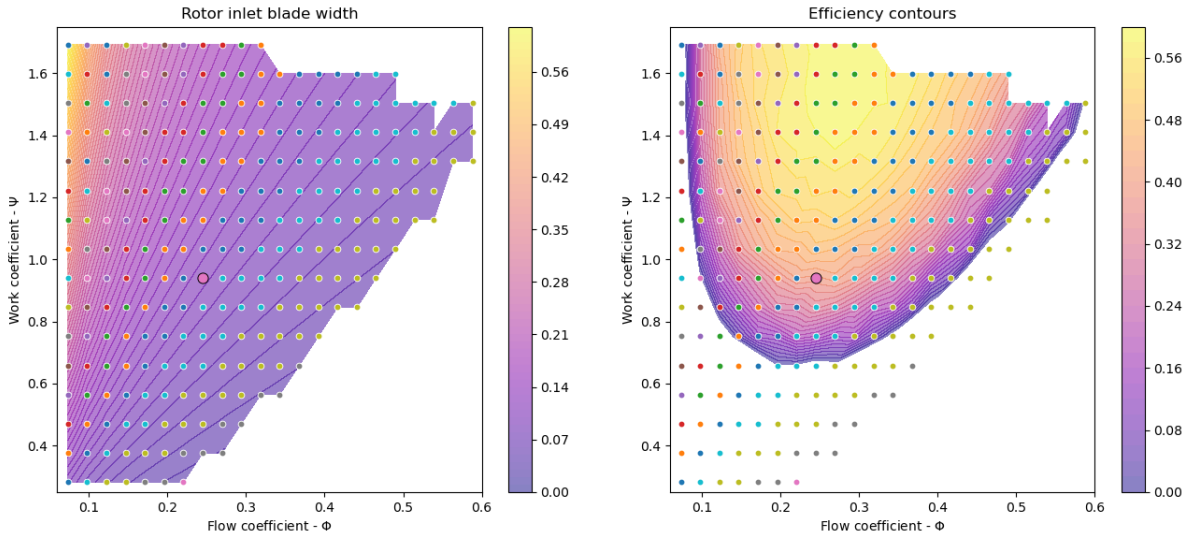


*Figure 6.37: Rotor inlet blade height in 0.01 mm intervals (Left) and Efficiency in 2% intervals (Right) for a variation of both the flow and work coefficient as inputs to the system model.*

- The isentropic efficiency that is assumed in the system model.
- The combination of the relative outflow angle of the rotor and the diameter ratio to match the relative outflow area with the throat area.
- The design point, which might not be as optimal of a choice for all variations.

Finally, the efficiency contours can be overlayed on the graph constructed by Chen and Baines [115] to compare the results of this study to the source of the original estimations as shown inFigure 6.38. It is the authors' opinion that due to the vastly different gas properties of hydrogen and (hot) air and different applications, the total values of the efficiency contours should not be compared directly. Instead, it is more relevant to compare the overall shape of the efficiency contours and their position with respect to the flow and work coefficient axis.

Overall it can be observed that the contour lines seem to form part of a similar ellipse shape that is offset with a factor of $\pm 10 - 20\%$ on the axis of the flow coefficient and $\pm 60 - 80\%$ on the axis of the work coefficient. A more optimal design point would thus seem to be centred around a flow coefficient of 0.27 - 0.294 and a work coefficient of 1.5 - 1.7.

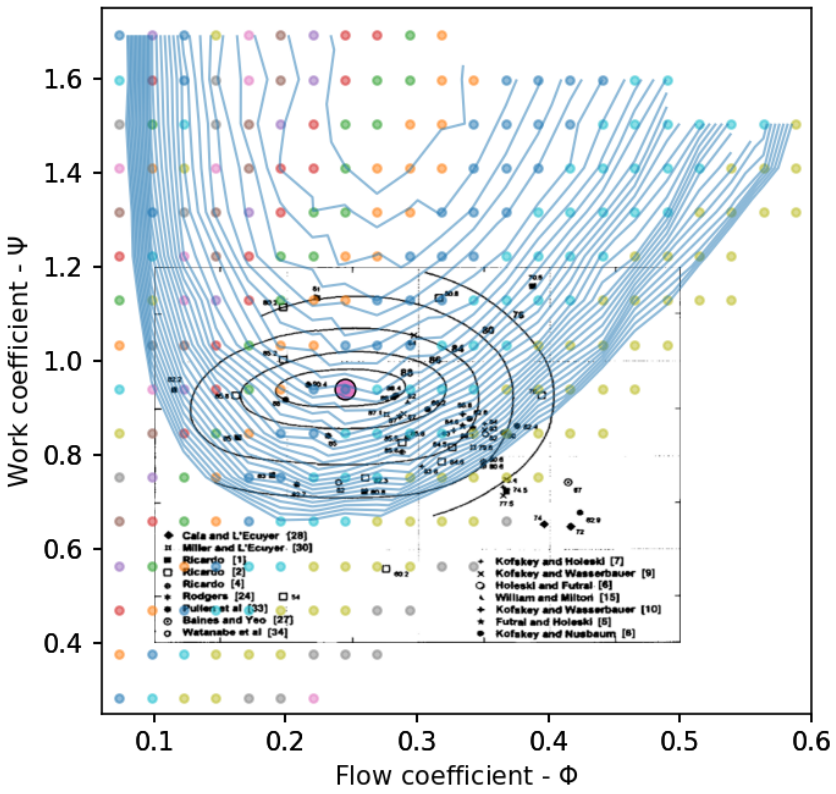


*Figure 6.38: Comparison between the current results and the performance charts from Chen and Baines (1994) [115].*

## 6.8 Comparison of results to the most recent literature

As previously presented in Section 4.2, one of the very few publicly available references on the topic of recovering potential energy from compressed hydrogen - in a hydrogen refuelling station - is the study performed by Burgess et al. [102, 103] at NREL. Throughout most of the duration of this thesis work, the only information publicly available on this project were the two referenced presentations, which detail a project description and some very preliminary results. These also mentioned a request for funding and a potential project timeline but no further information or updated publications had been found.

That was until late December 2023, when an attempt was made to contact the original authors to inquire about the continuation of the project and/or any results. This was answered by Matthew Post, who previously worked on this project and very kindly provided a link to a very recently published report (Post et al., December 2023 [125]) that listed some preliminary outcomes of the project before it had indeed come to an end due to a lack of funding. The full details can be found in the report itself, which is titled: "Turboexpander for Direct Cooling in Hydrogen Vehicle Fueling Infrastructure" and is publicly available online.

As the publication is so recent and several very different assumptions and design decisions have been made in the process, this new information could not be integrated into this thesis. Instead, this section will provide an overview of its results and a comparison to this thesis work.

To start, this work by Post et al. made use of a third-party code called MassTran, which was provided by a project partner Scandia and used this program to predict the flow parameters in the refuelling cycle, essentially fulfilling the role of the system model in this thesis. Similarly, they also assumed a multi-buffer system with 3 buffer tanks at various pressures as opposed to a single high-pressure buffer tank. Furthermore, the code in MassTran also allowed them to predict the heat transfer through the tank walls, and they were able to validate these results of the vehicle tank temperature in MassTran with experimental data.

They also studied the cooling effect of the expansion process in the turboexpander for various assumed turbine efficiencies (40% - 70%) and the effect that this would have on the requirements of the pre-cooler in the system, concluding that the turboexpander indeed improves the efficiency of the station and reduces the cooling requirements of the pre-cooler. Furthermore, they conclude the section on the system modelling with the following quote:

*"There may be challenges developing turbomachinery designed for the low flowrates of light-duty fuel cell electric vehicle tanks. It is likely that simpler and more efficient designs of turboexpanders are possible for heavy-duty vehicles flowrates. Heavy-duty applications of this technology should be explored due to the ease of application and larger potential energy savings."*

This lies completely in line with the results of this thesis in which a higher mass flow rate has been assumed for this exact reason.

After validating the relevance of the application and defining the operating conditions of the turboexpander, the report continues with a section dedicated to turbine design which initially lists several possible turbine configurations but only continues to explore two concepts:

- The first preliminary design was, similar to this thesis, a radial inlet turbine. Interestingly enough, this already assumed a shrouded turbine which would indeed mitigate the significant contribution of the clearance losses that have been found. However, the reason for this initial design assumption is not provided. Furthermore, a large difference can be observed in the design philosophy. Where this thesis made an initial guess of an optimal performance point and used that to size the turbine accordingly - eventually leading to a trade-off between very small design features or very high rotor speeds - the work by NREL limited the rotor speed from the start and simply accepted that the design efficiency would be far from what is theoretically achievable but that the resulting design would be technically feasible to manufacture and operate. However, the report does not go into much detail regarding the exact design procedures and results that were used.
- The second preliminary design assumed an axial multi-stage turbine in an attempt to increase the turbine efficiency for lower rotor speeds which also lies in line with the conclusions of this thesis. A multi-stage design would allow for a smaller expansion ratio - and thus lower isentropic work - for each stage. This would, for the same work coefficient, lead to a lower tip speed of the rotor, effectively reducing the required rotor speed for a more optimal expansion.

Interestingly enough, the project continued working on the radial inlet turbine as opposed to the axial multi-stage turbine because of its higher perceived simplicity. They did run into issues when continuing to design the system around the rotor as they found that for the small mass flow and high pressures, the required nozzle size - the space between the stator vanes- would indeed be extremely small and hence pivoted towards a 2 stage design of a so-called "partial arc admission impeller". Although there are several illustrations provided, it is not entirely clear how this design is supposed to operate but it does appear that this is also no longer a radial

inlet, axial outlet turbine but rather a purely radial turbine. Unfortunately, no further details regarding the design or the design procedures are provided. However, they do, refer to the manufacturability of the design and state that it should be possible with Electronic Discharge Machining (EDM).

Next, the report covers a section on the techno-economical feasibility of integrating a turboexpander in a hydrogen refuelling station. The estimations of the capital investments required for the infrastructure and machinery predict that the hybrid system with a turboexpander would be only half as expensive as a traditional system; €35,000.00 instead of €70,000.00. As for the operational costs, no actual assessment has been included regarding the energy saved or recovered per refuelling cycle or per kg of hydrogen refuelled but instead it refers to the work of Elgowainy et al. [139] and mentions a reduced power consumption of 45 kWh /day as the cooling system can be reduced in size and does not require a large thermal buffer which has to be kept cool continuously. However, this assumption is somewhat out of context and should not be used as a general source for conclusions as it is very specific to one system design in a rather specific use case.

Finally, the report concludes with a description of the results and the statement that integrating a turboexpander with an efficiency higher than 50% in a hydrogen refuelling station could be technically feasible and would result in both capital and operational cost savings. It also highlights that light-duty applications, such as most automotive applications, are not ideal design cases and that there is more potential in refuelling cycles for heavy-duty applications where higher mass flows can be achieved.

All in all, the conclusions of this study are very much in line with what has been found in this thesis. However, its findings are arguably far more difficult to reproduce or even substantiate due to the lack of clarity surrounding the applied calculation and design methods.

# 7 Conclusions and recommendations

## 7.1 Conclusions

The initial scope of this thesis project was to find a suitable application for and develop a conceptual design of an expander used to recover potential energy stored in compressed hydrogen.

Through the initial literature study, a broad array of hydrogen applications and technologies has been explored. This lead to the finding that the most suitable application would be that of a Hydrogen Refuelling Station. The main reasons for this can be summarised in five points:

- First, the scale of the application proved to be decent middle-ground. Smaller applications such as in-vehicle expanders or pressure regulators were already predicted to have too small mass flows to result in any practical designs and would be plagued by cost, size and weight limitations. Larger, industrial-sized applications proved to be too complex and specific to design a general system model for. Instead, hydrogen refuelling stations proved to be relatively standardised systems that operate on a sufficiently large scale to result in a feasible design concept.
- Second, the few available publications that explored the topic of recovering potential energy from compressed hydrogen through a turboexpander all pointed towards hydrogen refuelling stations as a suitable application.
- Third, the existing standardisation of hydrogen refuelling processes and regulations provided a framework that could be used to develop a system model.
- Fourth, the available literature surrounding hydrogen refuelling stations themselves seemed to suggest that this is a system in which there is still a lot of room for future improvement and development, even the general architecture of such an HRS is not set in stone yet exemplified by ongoing research on the optimal amount of buffer tanks and pressure levels in storage tanks. This essentially proves that there is some flexibility in how these systems can be designed or be operated.
- Finally, the fact that there simply is a lot of energy to be recovered between the station's buffer tanks and the vehicle tank. Integrating a turboexpander in this application still has the potential to yield a significant return.

Based on this information, an HRS system model has been developed following a cascade buffer tank architecture in which three buffer tanks store hydrogen at different pressure levels. Within this HRS system model, a turbine model has been implemented around a single-stage radial inlet turbine configuration. The decision of this specific type of expander was primarily driven by the available literature as each of the three past publications on recovering potential energy from compressed hydrogen referred to a single-stage radial inlet turbine. Beyond that, this decision was further supported by the mechanical simplicity of rotating turbomachinery, the apparent relative simplicity of a single-stage design, and by the fact that for a single stage expander, a radial inlet turbine would be able to provide a higher expansion ratio than an axial turbine would be able to.

For the design and modelling of this turbine, a particular flow and work coefficient were assumed according to the available literature on optimal design parameters, as well as an assumed isentropic efficiency and several limiting parameters such as maximum rotor speed and minimum expansion ratio. This led to a set of potential turbine designs for different design points. Each

of these designs was then evaluated based on a set of loss models, and the design that provided the best overall performance was selected. This design consists of a 49.44 mm diameter rotor with 10 rotor blades that vary in height from 0.104 mm to 0.127 mm, designed to operate at a maximum rotor speed of 500,000 RPM.

This design would potentially operate at a 42.7% total-to-static efficiency and deliver 0.456 kWh of electric energy per 10 kg refuelling cycle (assuming a 70% efficient electric generator). Additionally, the fact that the hydrogen is expanded through a turbine in which work is extracted from the flow, leads to a cooling effect on the flow. This is opposed to the traditional practice of expansion through a throttling valve, in which the negative Joule-Thomson effect would result in a heating effect. Compared to a conventional HRS system, this cooling effect results in another energy saving of 1.31 kWh per refuelling cycle. Resulting in a net saving of 1.766 kWh per refuelling cycle or $0.1766\frac{kWh}{kg}$ of hydrogen. Compared to a total energy consumption of $2.43\frac{kWh}{kg}$, this presents a 7.36% saving in the operational energy expenditure of a hydrogen refuelling cycle. Based on an electricity price of €0.1347 per kWh and a station capacity of 1,000 $\frac{kg}{day}$, this would yield a €8,679.9 annual cost saving for a single refuelling station. However, that is purely an operational cost saving; other literature has predicted more significant savings when taking the infrastructure and maintenance costs into account.

Apart from the HRS system model and the 1D turbine model, a validation case has also been set up in Ansys, where a specific operating point has been modelled and simulated. In part, it is to visualise the flow behaviour around the predicted turbine design and, in part, to compare the performance of this 3D model to what has been found in the 1D model. At first glance, the flow appears to behave as predicted, with a clearly visible shockwave in the throat - as the rotor is choked at the selected operating point - and a decent flow path. Yet, there is a clear flow separation around the leading edge of the blade, indicating that the design could be further optimised to correct for slip. In addition to this, the results of the 3D model seem to indicate a much higher efficiency than what the 1D model finds. 79% total to static rotor efficiency in the 3D model as opposed to 42.7% total to static rotor efficiency in the 1D model. However, upon considering the differences between the two models, particularly the lack of clearance losses in the 3D model, the results appear to be consistent.

However, these are theoretical results. In practice, a turbine operating at a peak rpm of 500,000, generating up to 35 kW and having design features of 0.1 mm is far from realistic. Because of this, a first-order sensitivity analysis has been performed on some of the initial design assumptions. In particular, the assumed corrected mass flow rate, the maximum rotor speed, the flow coefficient, the work coefficient and the combination of the flow and work coefficient. As only these parameters have been changed and no other adjustments have been made to other parameters that would have been determined iteratively, this analysis is limited and eventually results in numerical errors for changes to the input that are too large. However, the results show that these initial guesses are not optimal either. In particular, they highlight the following facts which can be taken into consideration for future work.

- Increasing the mass flow and related variables (Essentially scaling the system) has a very large positive effect on both the efficiency and the feasibility of the design.
- Reducing the maximum rotor speed has the opposite effect. It leads to an increase in diameter and, with that, a lower blade height. The efficiency also reduces. However, it might be a practical limitation, and it is thus good to understand in which direction the results would move.
- The assumed flow coefficient is already quite close to its optimum point for efficiency. However, a change in that direction would lower the blade height and have a negative

effect on the feasibility of the design.

- Increasing the work coefficient however would result in both an increase in performance and an increase on the blade height and thus the feasibility of the design.

All in all, from this sensitivity study, it can be concluded that the current design can be improved by a more educated first guess of the flow and work coefficients. This would lead to both a more realistic and a better-performing design. Additionally, scaling up the system would provide another significant increase in both aspects. However, this would only be sensible if a suitable application can be found that could work on this scale. The current model already assumes a mass flow rate that has been described as technically feasible for medium- to heavy-duty refuelling applications (Buses, trucks, and heavy machinery) but has not yet been implemented in practice. Furthermore, in the current field of hydrogen applications and systems, there is no regulatory or technical framework to support refuelling cycles at these increased flow rates. However, it could be reasoned that applications in, for example, the marine and aerospace sectors are of a sufficiently large scale to allow for refuelling mass flow rates that go beyond what is currently in practice in automotive refuelling stations.

Finally, comparing these results to the very limited available literature and to the recently published interim report of Post et al. it can be concluded that the results found in this thesis align very well with all the previous work but also that it adds a lot of specificity and clarity surrounding the calculation and design methods used.

On the general topic of recovering potential energy from compressed hydrogen, only 4 publications have been found. Each of these also focused on Hydrogen Refuelling Stations as an application, but none of which went into the details providing an actual design methodology. Instead, all the previous studies relied on very broad performance assumptions. That makes, to the author's knowledge and as far as could be found in the publicly available literature, this the first study that presents an actual conceptual design of a turboexpander for the application in an HRS. Beyond that, it also covers where all the assumptions and design decisions stem from, an assessment of the performance of the design in the developed HRS system, a validation case using CFD software and an assessment of the practical limitations of the proposed design as well as suggestions for improvement. However, to provide an actual feasible design proposal, much more work would be required and the following section will detail several concrete recommendations for future work.

## 7.2 Recommendations

As there are several aspects to this thesis, the recommendations for future work will be split into several subsections. First, Subsection 7.2.1 will cover any recommendations and suggestions relating to the selected application and the system model of the HRS. Secondly, Subsection 7.2.2 will provide a set of recommendations relating to the design assumptions, procedures and analysis of the the turbine in the 1D model and finally Subsection 7.2.3 will present all the suggestions relating to the 3D simulation and the validation case.

### 7.2.1 On the system model

Starting with the selected application and the system model thereof. As outlined in both the results and the conclusion of this thesis, it has been shown that both the practical feasibility of a turbine design and its performance can be improved by increasing the scale of the system. The chosen application is that of a hydrogen refuelling station and within that context, the system

has already been scaled to the limits of what is currently deemed feasible following existing hydrogen refuelling protocols and regulations. These are however, based on singular refuelling events in the automotive sector, tailored to cars, buses, trucks and heavy machinery.

A first recommendation would therefore be to explore if the system can be scaled up even further for other applications in which a vehicle is refuelled. Examples would be refuelling cycles for aerospace or marine applications. These vehicles typically have fuel capacities that are orders of magnitude larger than what can be found in the automotive sector. Although there is recent interest in hydrogen as a fuel in both of these sectors, there does not yet appear to be a standardised protocol or dedicated research into these refuelling events but at some point there must be if this technology is to mature in those sectors.

However, there are several other recommendations to be made regarding the implementation of the current system model of an HRS.

First of all, the current system model does have its shortcomings, many assumptions and simplifications have been made which could be revised. For example:

- The heat transfer between system components such as the buffer tanks and the connecting lines to the ambient environment.
- The frictional losses throughout the system in valves, pipelines, fittings and bends.
- The simplified thermal effects in adding or removing mass to the buffer and vehicle tanks
- An idealised representation of the pre-cooler and dispenser with an instantaneous thermal effect.

Furthermore, the system model currently only represents a single refuelling event. In reality, a system would need to be able to handle periods of down time and several back-to-back refuelling events, each of which would be reflected in the state of the buffer tanks and the thermal balance between the components.

Taking these aspects into account, a second recommendation would thus be to improve the overall system model to present a more accurate representation of real-world conditions. Although these aspects could in theory be added to the existing model it is probably more interesting to adopt an existing, more robust, HRS model in which the module relating to the expander is interchanged with that of a turboexpander. Results of the literature study do show that research in the modelling of an HRS is already far more developed than that of designing and integrating a turboexpander in such a system.

Next, another recommendation would be to size the system following a concrete example of an existing HRS. The current model assumes certain sizes and initial conditions of the buffer tanks and performance specifications of the cooler and the dispenser based on reference in literature. However, not all references are consistent and choices had to be made based on what was deemed most relevant or based on what was expected to work well for this application with a turboexpander in the HRS. It would be interesting to see how the design and operation of a turboexpander would vary when it is implemented in a system that is not originally designed and sized for it.

Beyond the thermodynamical modelling of the components of the HRS, it would also be interesting to explore the control strategy of such a system. In the current model, the operation of the system is based on the mass flow rate which is calculated based on the optimal operation of the the expander itself. In practice, there might be other limitations that drive the control of the

system in which case the turbine would operate in sub-optimal conditions. This is something that has not been explored in the current work but would surely yield interesting conclusions. In very practical terms, this could provide an answer to the turbine's performance when it's design is not just scaled for a lower RPM but actually just limited to a maximum value for certain parts of its operation.

### 7.2.2 On the turbine design assumptions and methodology

Next, there are the recommendations relating to the design assumptions, design methods and the performance predictions of the of the turboexpander itself.

This thesis already presented several very concrete points of improvement such as a different set of initial assumptions, in particular, the flow and work coefficients which can be varied quite independently. Several other assumptions such as the maximum rotor speed, the expansion ratio and the clearances around the rotor could also be revised but are not fully independent as they might be limited by practical limitations. After all, this work presented a very idealised design which might need to be dialed down a bit to match real-life limitations.

Furthermore, a slightly simpler recommendation would also be to apply a correction for the slip factor of the rotor. As can be observed in the results of the 3D model, there is some separation around the leading edge of the blade and on the pressure side, indicating that the inflow angle might be too steep.

Beyond that, another recommendation would be to explore the applicability of the adopted loss models. As previously explained, these are the combined result of many other authors and are relatively widely adopted for more traditional turbomachinery applications. However, the design has some interesting features such as the very small blade height, the extremely high rotor speed and the very high pressures. As the loss models appear to include at least some empirical factors or relations it can be put to question how accurate these loss models are for this specific application. Of course, there wouldn't exist a specific set of equations for this exact application but a deeper look into the origin and make-up of loss models would be interesting as well as exploring variations of these models.

Finally, a more conceptual recommendation would be to explore a different type of turbomachine entirely. As already reasoned in this report, the choice of a single-stage radial inlet turbine has been based on what had been considered in previous work, the relative mechanical simplicity and the fact that for a single stage, a higher expansion ratio would be possible than with an axial stage. However, upon adopting the multi-buffer cascade system in the system model (which could potentially even be changed to 4 or 5 different buffer tanks), the expansion ratio actually lowered quite a bit. Furthermore, the main practical concerns regarding the current design are the high rotor speed and the small blade height. In fact, the assumption of the rotor speed is the result of a balance between these two practical limits. However, following Equation 7.1, it can be seen that for a certain stage, the tip speed is determined by the work coefficient and the isentropic enthalpy change across that stage. Thus, if the overall expansion process were divided over multiple stages, the enthalpy change for each individual stage would be less, which would, for a given work coefficient, result in a lower tip speed. This would in turn, result in a different balance between the maximum rotor speed $\omega$ and the blade height $b_2$.

$$u_2 = \sqrt{\frac{\Delta h_{tt,isen}}{\Phi}} \tag{7.1}$$

Aside from adopting a multi-stage design, adopting an axial architecture would bring an additional benefit relating to the design's manufacturability. As stated, the current design presents design features of 0.1mm in height, which, although not impossible, is definitely very difficult to achieve, and on this scale, the importance of surface roughness and other imperfections also becomes critical. In a radial inlet turbine, this also means that in traditional mahcining, operations have to happen in multiple planes as the passage evolves from radial to axial. An axial design, however, would only require these machining operations to happen in one plane and as suggested by Peirs et al. [145], this becomes possible with electro-discharge machining (EDM). This presents the practical benefit of a simple die being used instead of a rotating tool, which creates individual chips; this should aid in the accuracy of the turbine's surface finish. Alternatively, additive manufacturing techniques can also be explored but this would require a machine that can achieve sufficiently small layer heights.

Based on this, the recommendation would be to explore a multi-staged axial turbine instead of a radial inlet turbine. This reasoning was at some point also adopted in the study from NREL [146] but did not see any continuation.

### 7.2.3 On the 3D simulation of the turbine

Finally, some recommendations regarding the 3D modelling and simulation of the turbine can be provided.

Starting with the 3D design of the turbine. Currently, this is performed with the BladeGen module in Ansys. Although suitable for the job, it also appeared to be slightly limited in functionality. To properly match the mass flow between the 1D and 3D models, it was crucial to get the throat area right. In Bladegen, it is indeed possible to observe the flow area between the blades for this purpose. However, it is not a feature that can be controlled directly. Instead, this has to be done by manually tweaking the wrap angle of the blade around the rotor or by tweaking the shape of the spline of the blade angle and observing the calculated throat area in a different window. In truth, this is a very finicky process which is far from ideal. Therefore the recommendation would be to explore other modules in Ansys or in other software packages that can be used for generating the 3D shape of the turbine.

Similarly, the next block, TurboGrid, also appears to be limited in its functionality. In principle, it generates a mesh fully automatically, after which certain mesh settings and variables can be adjusted. However, this often resulted in negative volume errors and there was no consistent way in which the mesh could or should be changed to resolve these errors. Part of the reason for the limited mesh density in the spanwise direction is exactly this. That TurboGrid would consistently present erroneous results when the mesh was attempted to be refined. Therefore, it would also be worthwhile to explore if there are other modules within Ansys or entirely different software packages that can be used to generate a suitable mesh.

As for the CFX solver module, the functionality was perfect for this work, but recommendations would include adapting the boundary conditions to approximate the 1D model better. Very specifically, the current module does not include any clearance between the rotor and the shroud and the wall that is placed instead rotates along with the domain. This leads to the 3D model not being able to predict the effect of the clearance losses which have been shown to be a major contributor to the overall losses of the turbine.

In a similar fashion, the inlet domain also had to be adjusted to prevent backflow through an inlet boundary. As the inlet conditions are now specified at a different location, their values at the actual location of the rotor inlet are fully representative of the 1D model. However, the

backflow through an inlet domain or the interaction with the stator vanes is a very practical problem. A possible solution and general improvement of the 3D model could be to also model the stator vanes as a proper inlet domain and specify an interface between the stationary and rotating domains as is done with the outlet. This would, however, include a more intricate 3D model, which BladeGen doesn't provide.

Furthermore, a final recommendation would be to attempt to improve the modelling of boundary layer losses and turbulence effects. Due to challenges with the meshing software, the mesh has not been optimised to include a refined boundary layer and the turbulence settings of the domain have also been kept at the default settings.

# Bibliography


[1] A. Willige. *The colors of hydrogen: Expanding ways of decarbonization.* Accessed on 25/11/2023. July 28, 2022.

[2] Ibrahim Dincer and Canan Acar. "Review and evaluation of hydrogen production methods for better sustainability". In: *International Journal of Hydrogen Energy* 40.34 (2015), pp. 11094–11111. ISSN: 0360-3199. DOI: https://doi.org/10.1016/j.ijhydene.2014.12.035.

[3] *Hydrogen from methane reforming + CCS - carbon capture and storage.* Accessed on 06/04/2023.

[4] K. Liu, C. Song, and V. Subramani. *Hydrogen and Synsgas Production and Purification Technologies.* 2010.

[5] *Hydrogen Production: Electrolysis.*

[6] P.J. Linstorm and W.G. Mallard. *NIST Chemistry WebBook, NIST Standard Reference Database 69.* 1997.

[7] M. Aasadnia and M. Mehrpooya. "Large-scale liquid hydrogen production methods and approaches: A review". In: *Applied Energy* 212 (2018), pp. 57–83.

[8] S. Al Ghafri et al. "Hydrogen liquefaction: a review of the fundamental physics, engineering practice and future opportunities". In: *Energy Environ. Sci.* 15 (7 2022), pp. 2690–2731. DOI: 10.1039/D2EE00099G.

[9] D. Kim and A. Fischer. *Distributed energy resources for net zero: An asset or a hassle to the electricity grid?* Accessed on 05/04/2023.

[10] B. Miao, L. Giordano, and S. H. Chan. "Long-distance renewable hydrogen transmission via cables and pipelines". In: *International Journal of Hydrogen Energy* 46.36 (2021), pp. 18699–18718.

[11] H. Ritchie, M. Roser, and P. Rosado. "Energy Mix". In: (2022). Accessed on 05/04/2023.

[12] *Converting the Natural Gas Grid for Hydrogen Delivery.* Accessed on 05/04/2023.

[13] C. Findlay. *Repurposing natural gas infrastructure for hydrogen.* Accessed on 05/04/2023. Sept. 11, 2020.

[14] B.D. James et al. *Analysis of Advanced H2 Production & Delivery Pathways.* Accessed on 19/04/2023. June 2019.

[15] *Silyzer 300 - The next paradigm of PEM electrolysis.* Accessed on 20/04/2023. 2020.

[16] *Siemens Energy gas turbine portfolio.* Accessed on 20/04/2023. 2022.

[17] *Fuel cells.* Accessed on 06/04/2023.

[18] B. Sundén. *Chapter 8 - Fuel cell types - overview.* Ed. by B. Sundén. 2019.

[19] *HySTRA: CO2-free Hydrogen Energy Supply-chain Technology Research Association.* Accessed on 05/04/2023.

[20] R. Gerboni. "11 - Introduction to hydrogen transportation". In: *Compendium of Hydrogen Energy.* Ed. by R. B. Gupta, A. Basile, and T.N. Vezoroğlu. Woodhead Publishing Series in Energy. Woodhead Publishing, 2016, pp. 283–299.

[21] *Hydrogen Transport & Distribution.* Accessed on 09/04/2023. Nov. 2021.

[22] *Increased hydrogen capacity of GH 2 road trailers.* Accessed on 09/04/2023. Feb. 7, 2022.

[23] *Calvera Hydrogen Develops for Shell Hydrogen The Tube Trailer Model for Transporting Hydrogen, with The Highest Capacity in The World.* Accessed on 09/04/2023. Feb. 10, 2023.

[24] R. van Rossum et al. *European hydrogen infrastructure vision covering 28 countries.* Accessed on 09/04/2023. Apr. 2020.

[25] E. Lycklama and A. Nijeholt. *Hydrogen network Netherlands.* Accessed on 09/04/2023.

[26] M. Penev, J. Uboy, and C. Hunter. "Economic analysis of a high-pressure urban pipeline concept (HyLine) for delivering hydrogen to retail fueling stations". In: *Transportation Research Part D: Transport and Environment* 77 (2019), pp. 92–105.

[27] *Transporting Pure Hydrogen by Repurposing Existing Gas Infrastructure: Overview of existing studies and reflections on the conditions for repurposing* . Accessed on 09/04/2023. July 16, 2021.

[28] *Hydrogen Energy Supply Chain Pilot Project between Australia and Japan.* Accessed on 11/04/2023. Feb. 2022.

[29] *World's first liquid hydrogen carrier completes round trip.* Accessed on 11/04/2023. 2022.

[30] *Kawasaki Develops Cargo Containment System for Large Liquefied Hydrogen Carrier with World's Highest Carrying Capacity.* Accessed on 11/04/2023. May 6, 2021.

[31] J. Chen et al. "Dynamic simulation of the potential of integrating a turbo-expander in a hydrogen refueling station". In: *Applied Thermal Engineering* 202 (2022), p. 117889.

[32] *Energy storage – the role of electricity.* Accessed on 05/04/2023.

[33] A. Alexander, M.D. Shamsuddoha, and B. Gangadhara Prusty. "A review of Type V composite pressure vessels and automated fibre placement based manufacturing". In: *Composites Part B: Engineering* 253 (2023). ISSN: 1359-8368.

[34] *All about liquid hydrogen.* Accessed on 10/05/2023.

[35] *Large scale Hydrogen Storage in German salt caverns.* Accessed on 27/04/2023. Jan. 20, 2023.

[36] *H2 in the underground: Are salt caverns the future of hydrogen storage?* Accessed on 27/04/2023. July 27, 2021.

[37] *Storing Hydrogen.* Accessed on 27/04/2023. July 27, 2021.

[38] *Gas turbines: essential for the transition to renewable energy sources.* Accessed on 06/04/2023.

[39] *Hydrogen fueled gas turbines.* Accessed on 06/04/2023.

[40] J. Goldmeer and J. Catillaz. *Hydrogen for power generation: Experience, requirements, and implications for use in gas turbines.* Accessed on 06/04/2023.

[41] J. Goldmeer. *Is there a Hydrogen Future for Your Gas Turbine?* Accessed on 06/04/2023. Nov. 8, 2021.

[42] *Zero Emission Hydrogen Turbine Center – on the path to decarbonization.* Accessed on 06/04/2023.

[43] N. Tekin. *Enhancement of Fuel Flexibility of Industrial Gas Turbines by Development of Innovative Hydrogen Combustion Systems.* Accessed on 05/06/2023. 2023.

[44] *Hydrogen Gas Turbine - Decarbonizing power generation with minimal modifications.* Accessed on 06/04/2023.

[45] *Power From Hydrogen Gas For Carbon Reduction.* Accessed on 06/04/2023.

[46] S. Öberg, M. Odenberger, and F. Johnsson. "Exploring the competitiveness of hydrogen-fueled gas turbines in future energy systems". In: *International Journal of Hydrogen Energy* 47.1 (2022), pp. 624–644.

[47] C. Paolo, L. Giovanni, and M. Luigi. "Using Hydrogen as Gas Turbine Fuel". In: *Journal of Engineering for Gas Turbines and Power-transactions of The Asme - J ENG GAS TURB POWER-T ASME* 127 (Jan. 2005). DOI: 10.1115/1.1787513.

[48] *A literature review of Hydrogen and Natural Gas turbines: Current state of the are with regard to performance and NOx control*. Accessed on 06/04/2023. Aug. 12, 2020.

[49] *Hydrogen workshop for fleet operators*. Powerpoint slides retrieved on 21/04/2023. May 23, 2006.

[50] W.J. McLean et al. "Hydrogen as a reciprocating engine fuel". In: *Future Automotive Fuels* (1977).

[51] *Module 3: Hydrogen use in internal combustion engines*. Accessed on 21/04/2023. Dec. 2001.

[52] *Toyota Developing Hydrogen Engine Technologies Through Motorsports*. Accessed on 20/04/2023. Apr. 22, 2021.

[53] *H2 – key player in the Maritime Energy Transition*. Accessed on 20/04/2023.

[54] *NedStack PEMGen Solutions*. Accessed on 06/04/2023.

[55] *European first emergency power supplies on green hydrogen in Groningen.* Accessed on 06/04/2023.

[56] *Europe's first Data Centre powered by PEM fuel cell technology has opened today at NorthC Datacenters in Groningen*. Accessed on 06/04/2023.

[57] *Applications: The energy transition at the heart of our projects*. Accessed on 06/04/2023.

[58] *A Guide to Hydrogen Generators (Gensets)*. Accessed on 06/04/2023. Nov. 16, 2022.

[59] "H2Live". *Hydrogen vehicles: All models at a glance*. Accessed on 04/04/2023.

[60] H. Basma and F. Rodrígues. "Fuel cell electric tractor-trailers: Technology overview and fuel economy". In: *International Council on Clean Transportation* (July 2022).

[61] R. M. Samsun et al. "Deployment Status of Fuel Cells in Road Transport: 2021 Update". In: *Energie & Umwelt /Energy & Environment* 542 (July 2022). Accessed on 04/04/2023.

[62] *China Launches 100-mph Hydrogen Supercapacitor Train*. Accessed on 04/04/2023. Jan. 24, 2023.

[63] P. Ridden. *Hydrogen-powered trains enter passenger service in Germany*. Accessed on 04/04/2023. Aug. 25, 2022.

[64] *ENvironmentally Friendly Inter City Aircraft powered by Fuel Cells (ENFICA-FC)*. Accessed on 04/04/2023.

[65] *Global observer, aerovironment's extreme endurance unmanned aircraft system, achieves historic first hydrogen-powered flight*. Accessed on 04/04/2023. Jan. 11, 2011.

[66] *HY4 Aircraft*. Accessed on 04/04/2023.

[67] *ZeroAvia Makes Aviation History, Flying World's Largest Aircraft Powered with a Hydrogen-Electric Engine*. Accessed on 04/04/2023. Jan. 19, 2023.

[68] S. Doll. *Universal Hydrogen's 40-passenger hydrogen electric plane completes maiden flight*. Accessed on 04/04/2023. Mar. 2, 2023.

[69] *ZEROe: Towards the world's first zero-emission commercial aircraft*. Accessed on 04/04/2023.

[70] *Airbus reveals hydrogen-powered zero-emission engine*. Accessed on 04/04/2023. Nov. 30, 2022.

[71] *Our future flies in clean skies*. Accessed on 04/04/2023.

[72] M. Genovese and P. Fragiacomo. "Hydrogen refueling station: Overview of the technological status and research enhancement". In: *Journal of Energy Storage* 61 (2023), p. 106758.

[73] *Fuel cells vs. batteries: what's the difference?* Accessed on 06/04/2023. May 27, 2022.

[74] *Viritech signs an MOU with ANEVOLVE.* Accessed on 06/04/2023.

[75] C. Crownhart. *How hydrogen and electricity can clean up heavy industry.* Accessed on 06/04/2023. Oct. 12, 2022.

[76] L. Rodgers. *Climate change: The massive CO2 emitter you may not know about.* Accessed on 06/04/2023. Dec. 17, 2018.

[77] *Cement Kilns in a Green Hydrogen Economy.* Accessed on 06/04/2023. Nov. 24, 2022.

[78] F. B. Juangsa et al. "Thermodynamic analysis of hydrogen utilization as alternative fuel in cement production". In: *South African Journal of Chemical Engineering* 42 (2022), pp. 23–31.

[79] C. Hoffmann, M. Van Hoey, and B. Zeumer. *Decarbonization challenge for steel - Hydrogen as a solution in Europe.* Accessed on 06/04/2023. June 3, 2020.

[80] A. Toktarova et al. "Pathways for Low-Carbon Transition of the Steel Industry — A Swedish Case Study". In: *Energies* 13.15 (2020). ISSN: 1996-1073.

[81] C. Kurrer. *The potential of hydrogen for decarbonising steel production.* Accessed on 06/04/2023. 2022.

[82] K.S. Satyendra. *Hydrogen gas and its use in Iron and Steel industry.* Accessed on 08/05/2023. Jan. 14, 2019.

[83] *The role of hydrogen and ammonia in meeting the net zero challenge.* Accessed on 08/05/2023.

[84] H. Chen et al. "Study on real-gas equations of high pressure hydrogen". In: *International Journal of Hydrogen Energy* 35.7 (2010). 2008 International Hydrogen Forum (HyForum2008), pp. 3100–3104.

[85] J. Chen et al. "Modeling a hydrogen pressure regulator in a fuel cell system with Joule–Thomson effect". In: *International Journal of Hydrogen Energy* 44.2 (2019), pp. 1272–1287.

[86] *Joule–Thomson effect.* Accessed on 20/04/2023.

[87] N. Mukherjee. *Joule Thomson effect [JT]: A short review.* Accessed on 18/04/2023. Mar. 6, 2022.

[88] J.Q. Li et al. "A study on the Joule-Thomson effect of during filling hydrogen in high pressure tank". In: *Case Studies in Thermal Engineering* 41 (2023), p. 102678.

[89] *Compressed air – the fourth utility of the modern world.* Accessed on 25/04/2023. Apr. 8, 2021.

[90] Health & Safety Office of Environment. *Calculating the Stored Energy of a Pressurized Gas Vessel.*

[91] *Underground Hydrogen Storage.* Accessed on 27/04/2023. 2022.

[92] *Prospects for hydrogen and fuel cells.* Accessed on 27/04/2023. 2005.

[93] U. Bossel. *Well-to-Wheel Studies, Heating Values, and the Energy Conservation Principle.* 2003.

[94] *Fueling Protocols for Light Duty Gaseous Hydrogen Surface Vehicles J2601_202005.* May 2020. DOI: https://doi.org/10.4271/J2601_202005.

[95] *Global technical regulation on hydrogen and fuel cell vehicles*. June 27, 2013.

[96] J.C. Garcia-Navarro. *What does a hydrogen refueling station look like?* June 5, 2021.

[97] R. Caponi et al. "Thermodynamic modeling of hydrogen refueling for heavy-duty fuel cell buses and comparison with aggregated real data". In: *International Journal of Hydrogen Energy* 13 (Feb. 2021).

[98] E. Rothuizen and M. Rokni. "Optimization of the overall energy consumption in cascade fueling stations for hydrogen vehicles". In: *International Journal of Hydrogen Energy* 39 (Jan. 2014), pp. 582–592. DOI: 10.1016/j.ijhydene.2013.10.066.

[99] *Pioneer's innovative Cascade Technology - Offering more hydrogen refills and greater utilisation*. Accessed on 17/04/2023. June 27, 2013.

[100] "Effects of pressure levels in three-cascade storage system on the overall energy consumption in the hydrogen refuelling station". In: *International Journal of Hydrogen Energy* 46.61 (2021), pp. 31334–31345. ISSN: 0360-3199.

[101] E. Rothuizen et al. "Optimization of hydrogen vehicle refueling via dynamic simulation". In: *International Journal of Hydrogen Energy* 38 (Apr. 2013), pp. 4221–4231. DOI: 10.1016/j.ijhydene.2013.01.161.

[102] R. Burgess. *Turboexpander: Alternative Fueling Concept for Fuel Cell Electric Vehicle Fast Fill – Proof of Concept Testing*. June 14, 2018.

[103] M. Post and D. Leighton. *Turboexpander: Alternative Fueling Concept for Fuel Cell Electric Vehicle Fast Fill*. Apr. 30, 2019.

[104] J. Yoshida et al. "Thermodynamic analysis of high pressure hydrogen gas refueling system with turbo-expanders". In: *Mechanical Engineering Journal* 6 (Apr. 2019). DOI: 10.1299/mej.18-00388.

[105] *European patent application: EP3421865*. Feb. 1, 2019.

[106] M. Francesconi, E. Dori, and M. Antonelli. "Analysis of Balje diagrams for a Wankel expander prototype". In: *Applied Energy* 238 (2019), pp. 775–785. ISSN: 0306-2619. DOI: https://doi.org/10.1016/j.apenergy.2019.01.096.

[107] D. Olivier et al. "Comparison of a scroll, a screw, a roots, a piston expander and a Tesla turbine for small-scale organic Rankine cycle". In: Sept. 2019.

[108] M. Gambini and Vellini M. *TUrbomachinery - FUndamentals, Selection and Preliminary Design*. Ed. by S.B. Choi. Springer Tracts in Mechanical Engineering, 2014. DOI: 10.1007/978-3-030-51299-6.

[109] M. Pini. *Lecture slides of AE4206 Turbomachinery*. Internal publication. 2023.

[110] "Fluid Mechanics and Thermodynamics of Turbomachinery (Seventh Edition)". In: ed. by S.L. Dixon and C.A. Hall. Seventh Edition. Boston: Butterworth-Heinemann, 2014. ISBN: 978-0-12-415954-9. DOI: https://doi.org/10.1016/B978-0-12-415954-9.00011-5.

[111] M. Schobeiri. *Turbomachinery Flow Physics and Dynamic Performance*. Nov. 2012. ISBN: 978-3-642-24674-6. DOI: 10.1007/978-3-642-24675-3.

[112] S. Korpela. *Principles of Turbomachinery*. Vol. 108. Nov. 2011. ISBN: 9780470536728. DOI: 10.1002/9781118162477.ch12.

[113] Erian A. Baskharone. *Principles of Turbomachinery in Air-Breathing Engines*. Cambridge Aerospace Series. Cambridge University Press, 2006. DOI: 10.1017/CBO9780511616846.

[114] M.R. Anderson. *Performance Corrections for Compressor Maps*. Accessed on 13/05/2023. Mar. 29, 2019.

[115] H. Chen and N.C. Baines. "The Aerodynamic Loading of Radial and Mixed-Flow TUrbines". In: *International Journal of Mechnaical Science* 36.1 (1994), pp. 63–79.

[116] C. Rodgers. *Mainline performance prediction for radial inflow turbines.* Lecture Series 1987-07. 1987.

[117] S.K. Ghosh, R.K. Sahoo, and S.K. Sarangi. "Mathematical analysis for off-design performance of cryogenic Turboexpander". In: *ASME J Fluids Eng* (2011).

[118] G.Q. Deng et al. "An integrated design and optimization approach for radial inflow turbines. Part I: automated preliminary design". In: *MDPI Appli Sci* (2018).

[119] A. Meroni et al. "A methodology for the preliminary design and performance prediction of high-pressure ratio radial-inflow turbines". In: *Energy* (2018).

[120] G.A. Wasserbauer and A.J. GLassman. *Fortran program for predicting off-design performance of radial-inflow turbines.* NASA TN D-8063. 1975.

[121] J. Qi et al. "Supercritical CO2 radial turbine design performance as a function of turbine size parameters." In: *J Turbomach* (2017).

[122] A. Glassman. *Enhanced analysis and users manual for radial-inflowturbine conceptual design code RTD.* Techical Report. NASA, Washington D.C., USA. 1995.

[123] N.C. Baines. *Radial turbine design. In: Moustapha H (ed) Axial and Radial Turbines.* White River Junction, Vt, Concepts NREC. 2003.

[124] L. Jiang et al. "Research on aerodynamic characteristics of two-stage axial micro air turbine spindle for small parts machining". In: *Advances in Mechanical Engineering* 12 (Dec. 2020), pp. 1–12. DOI: 10.1177/1687814020984373.

[125] Matthew Post et al. *Turboexpander for Direct Cooling in Hydrogen Vehicle Fueling Infrastructure.* 2023.

[126] I.H. Bell et al. "Pure and Pseudo-pure Fluid Thermophysical Property Evaluation and the Open-Source Thermophysical Property Library CoolProp". In: *Industrial & Engineering Chemistry Research* 53.6 (2014), pp. 2498–2508.

[127] Daniel Heere. *Modelling and Optimisation of a Hydrogen Refuelling Station based on CH2P Technology Delivering decentralised hydrogen and electricity for mobility.* Apr. 2019.

[128] *Refueling Protocols for Medium and Heavy-Duty Vehicles.* Apr. 2022.

[129] Krishna Reddi et al. "Impact of hydrogen SAE J2601 fueling methods on fueling time of light-duty fuel cell electric vehicles". In: *International Journal of Hydrogen Energy* 42.26 (2017), pp. 16675–16685. ISSN: 0360-3199. DOI: https://doi.org/10.1016/j.ijhydene.2017.04.233. URL: https://www.sciencedirect.com/science/article/pii/S0360319917316853.

[130] C. Zwyssig, J.W. Kolar, and S.D. Round. "Megaspeed Drive Systems: Pushing Beyond 1 Million r/min". In: *Mechatronics, IEEE/ASME Transactions* 14.5 (2009), pp. 564–574.

[131] A.H. Epstein et al. "Shirtbutton-sized gas turbines: The engineering challenges of micro high speed rotating machinery". In: (2000).

[132] *e+a MotorScout.* Last retrieved online on 09/01/24.

[133] *High-Speed Generators for Turbomachinery.* Last retrieved online on 09/01/24.

[134] *High Speed Generator.* Last retrieved online on 09/01/24, last data update on 25/05/2014.

[135] *Turbomachinery High-speed motor elements.* Last retrieved online on 09/01/24.

[136] *High-Speed Electric Motor Generators for High Efficiency and Power Density.* Last retrieved online on 09/01/24.

[137] *ate-system product information*. Last retrieved online on 09/01/24.

[138] *High-speed motors with up to 500,000 revolutions per minute*. Last retrieved online on 09/01/24.

[139] A. Elgowainy et al. "Techno-economic and thermodynamic analysis of pre-cooling systems at gaseous hydrogen refueling stations". In: *International Journal of Hydrogen Energy* 42.49 (2017), pp. 29067–29079. ISSN: 0360-3199. DOI: https://doi.org/10.1016/j.ijhydene.2017.09.087.

[140] *Electricity price statistics for non household consumers in 2023*. Last retrieved online on 09/01/24.

[141] *Refueling solutions*. Last retrieved online on 27/01/24.

[142] *Hydrogen refueling stations catalogue 2021: Power your mobility with clean energy*. Last retrieved online on 27/01/24.

[143] *Hydrogen Fueling Stations Cost*. Last retrieved online on 09/01/24.

[144] "Energetic evaluation of hydrogen refueling stations with liquid or gaseous stored hydrogen". In: *International Journal of Hydrogen Energy* 44.13 (2019), pp. 6795–6812. ISSN: 0360-3199. DOI: https://doi.org/10.1016/j.ijhydene.2019.01.087.

[145] Jan Peirs, Dominiek Reynaerts, and Filip Verplaetsen. "https://www.sciencedirect.com/science/article/p In: *Sensors and Actuators A: Physical* 113.1 (2004), pp. 86–93. ISSN: 0924-4247. DOI: https://doi.org/10.1016/j.sna.2004.01.003.

[146] G. Parks et al. *Hydrogen Station Compression, Storage, and Dispensing Technical Status and Costs*. Last retrieved online on 09/01/24. May 2014.

# A Parameters of the real gas model of hydrogen in Ansys.


*Figure A.1: Screencapture of the options under the H2 real gas model in Ansys 1/3.*

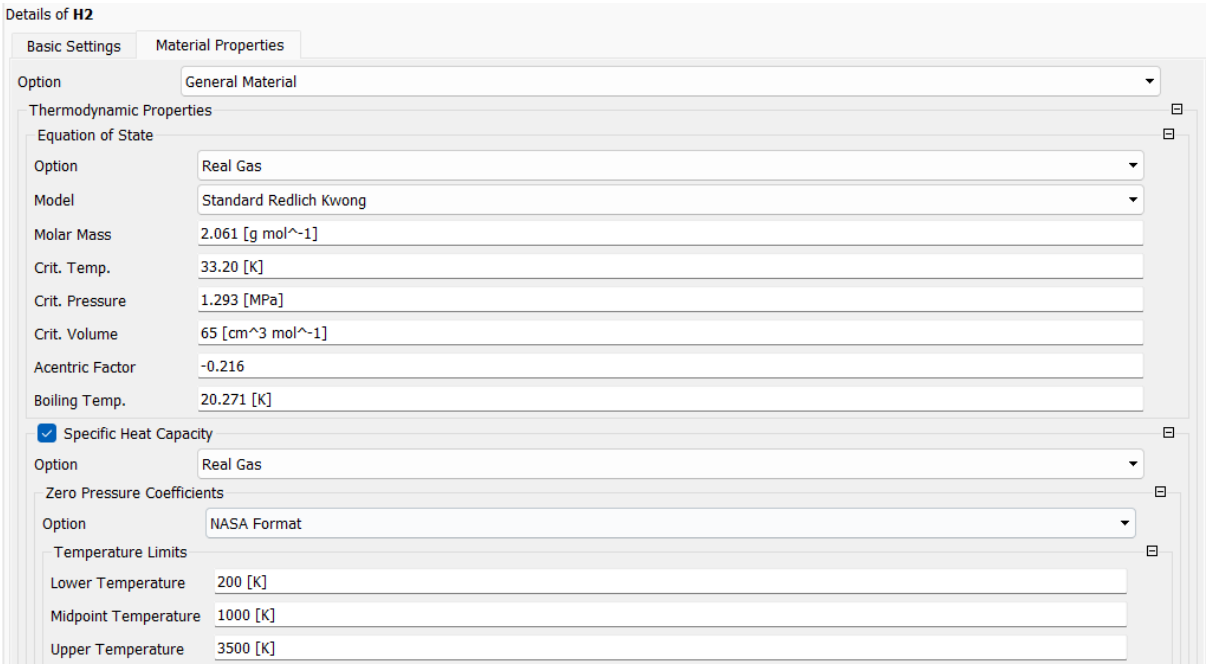


*Figure A.2: Screencapture of the options under the H2 real gas model in Ansys 2/3.*

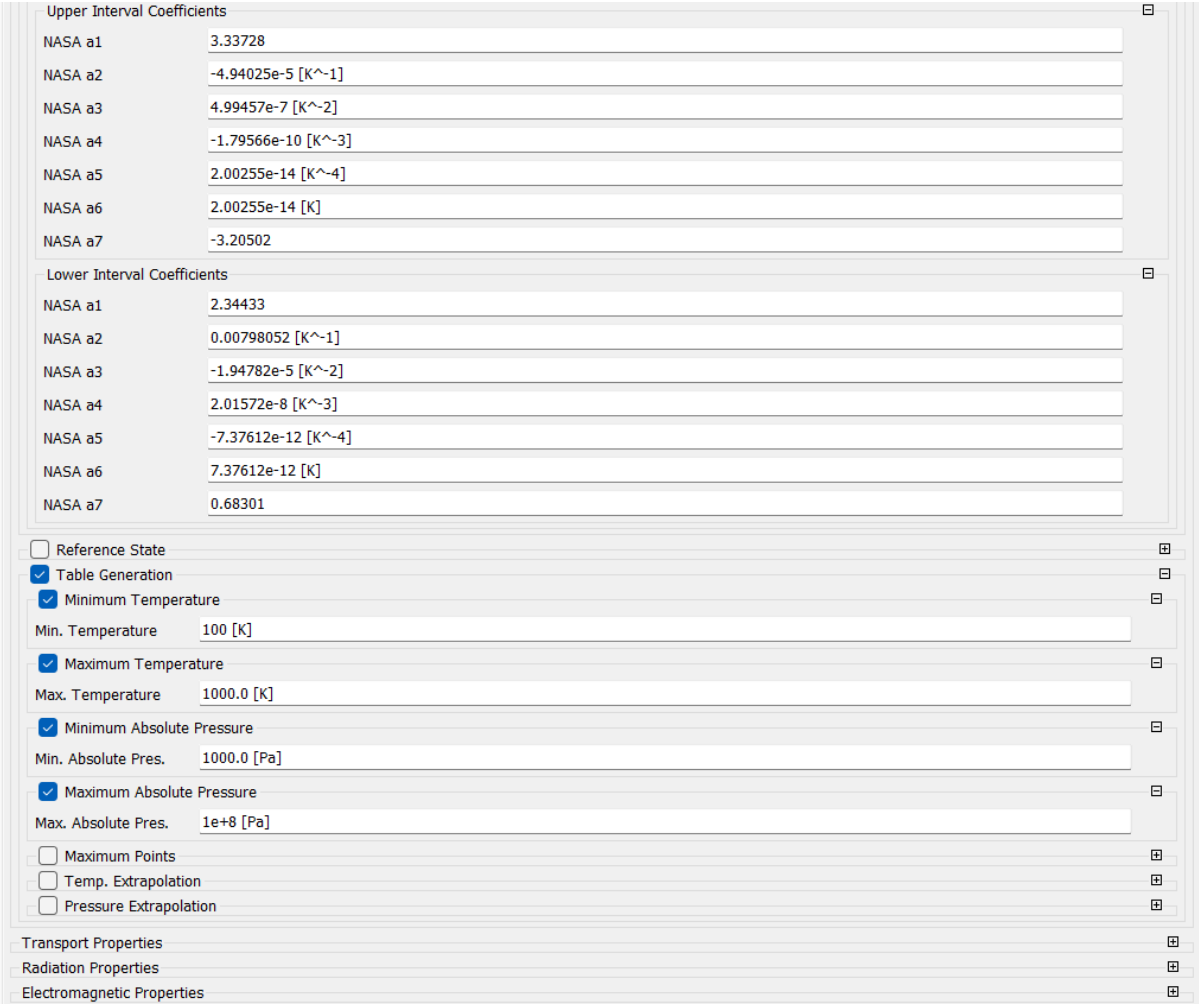


*Figure A.3: Screencapture of the options under the H2 real gas model in Ansys 3/3.*

# B Graphical results of the CFD simulations

This appendix serves to provide all the relevant contour plots generated in Ansys in a sufficiently large figure size. First, the velocity streamlines and magnitudes are shown in Section B.1. After this, Section B.2 presents the results of the Mach number of the flow and Section B.3 shows the results of the different pressure variables, Section B.4 those of the temperature, Section B.5 those of the density. Of all these properties, the static value is shown as well as the total value in both the relative and stationary reference frames. Finally, Section B.6 shows the contour plots of the static enthalpy and the total enthalpy in the stationary reference frame.

The naming of the variables is consistent with the definitions used in Ansys which can be summarised as follows:

- **Static** pressure and temperature mean just that, the static pressure and temperature which are unaffected by which definition of velocity is used.
- **Total in the stationary frame** relates to the total pressure pressure and temperature calculated with the absolute velocity component, $v$.
- **Total in the relative frame** relates to the total pressure and temperature calculated with the relative velocity component, $w$.

## B.1 Velocity plots

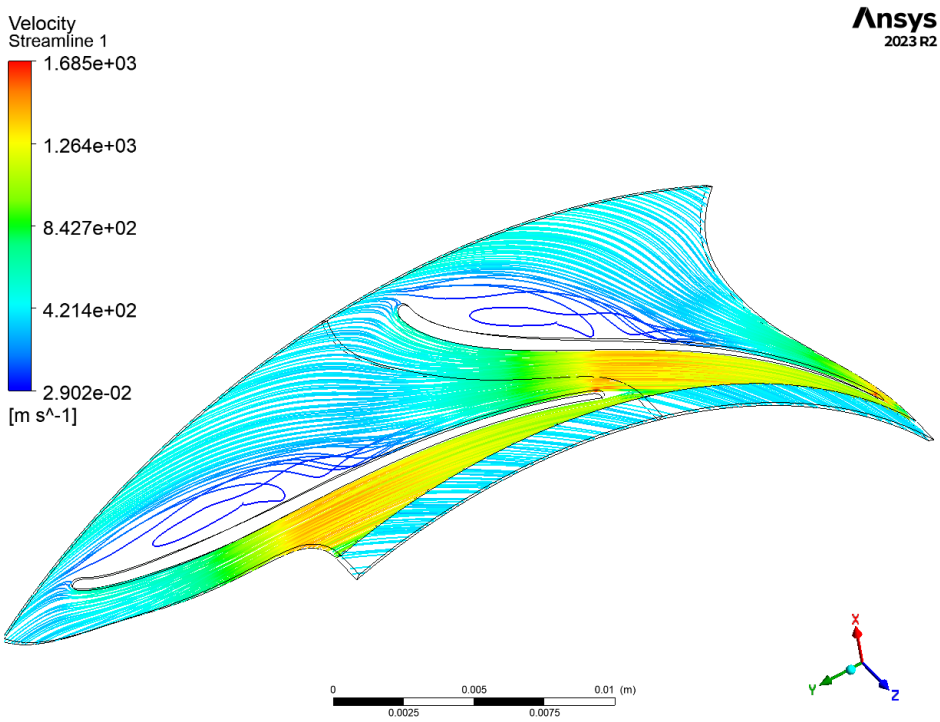


*Figure B.1: Velocity streamlines relative in the relative frame.*

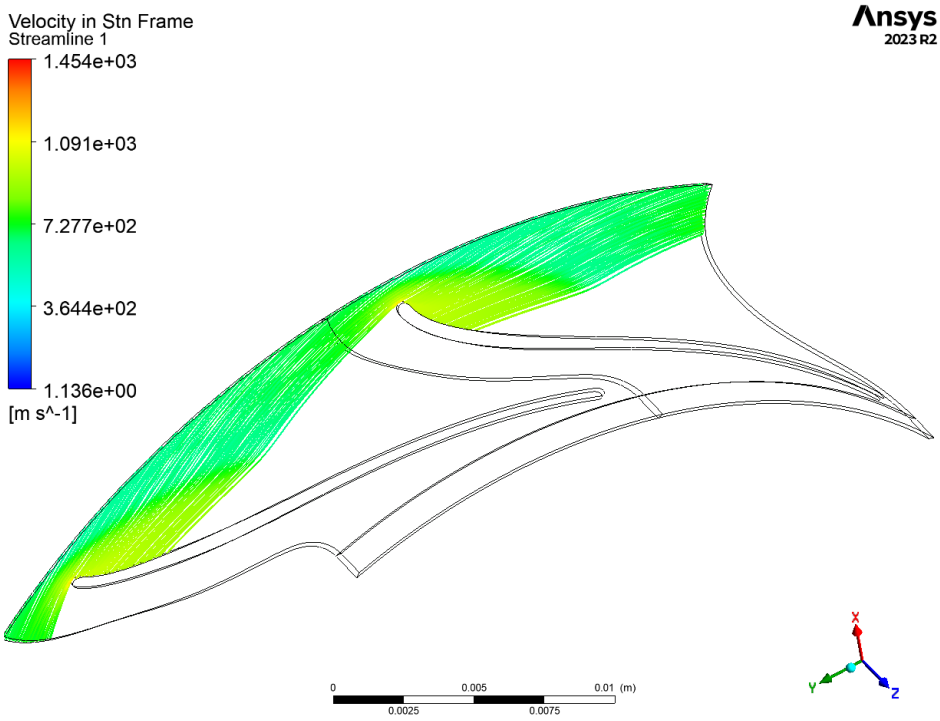


*Figure B.2: Velocity streamlines relative in the stationary frame.*

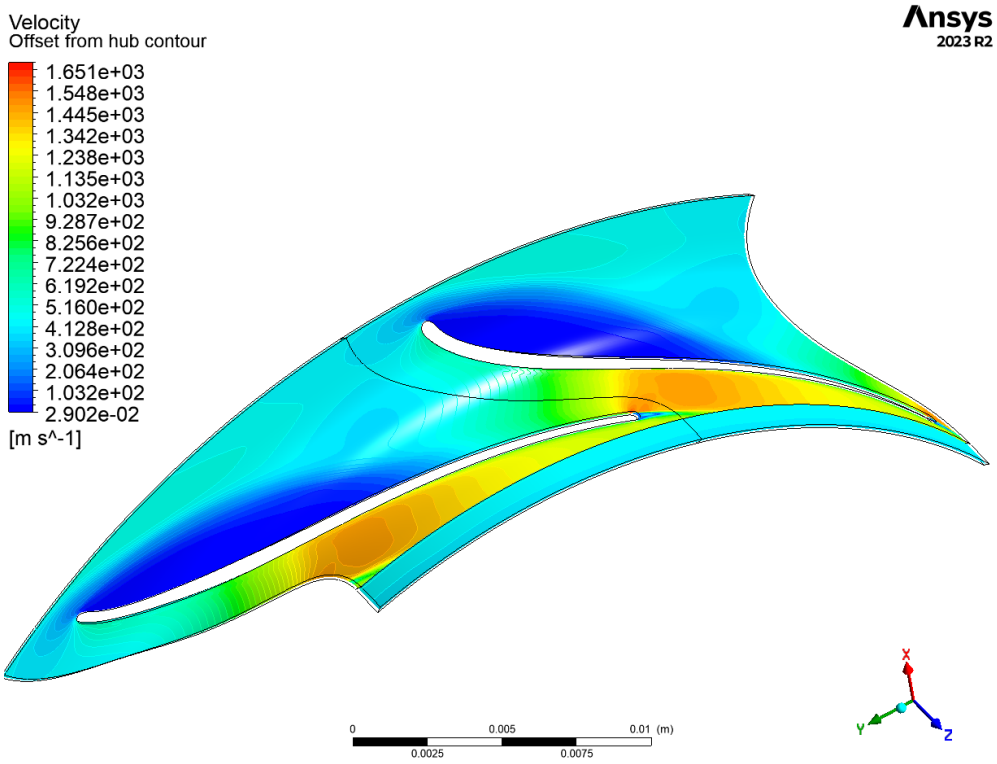


*Figure B.3: Contour plot of the velocity in the relative frame.*

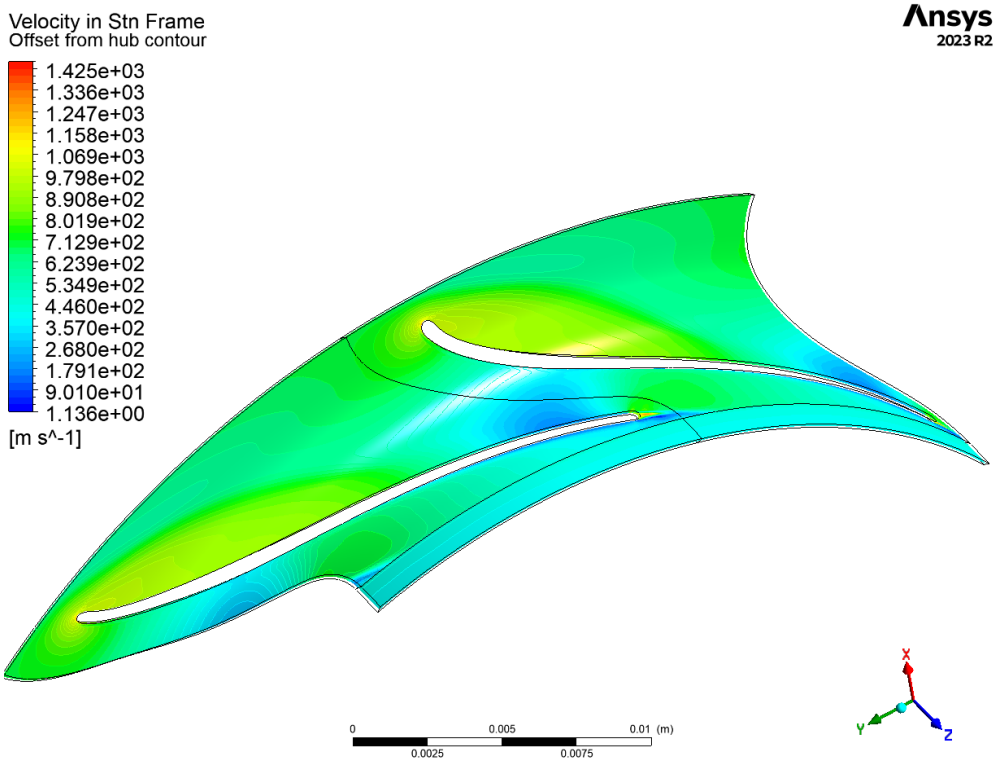


*Figure B.4: Contour plot of the velocity in the stationary frame.*

## B.2 Mach number contour plots

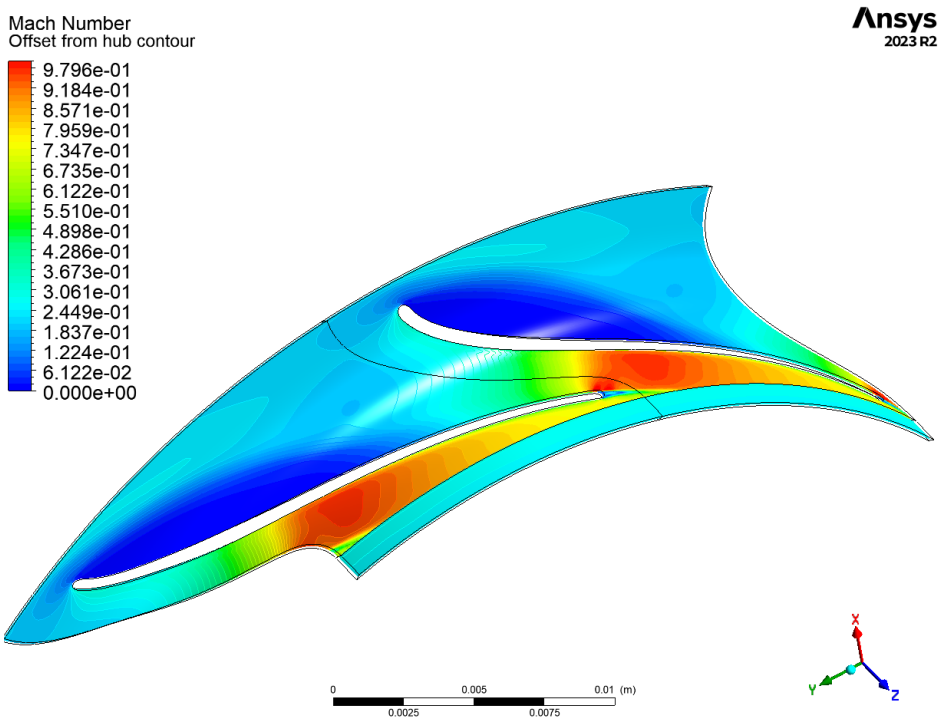


*Figure B.5: Contour plot of the Mach number in the relative frame.*

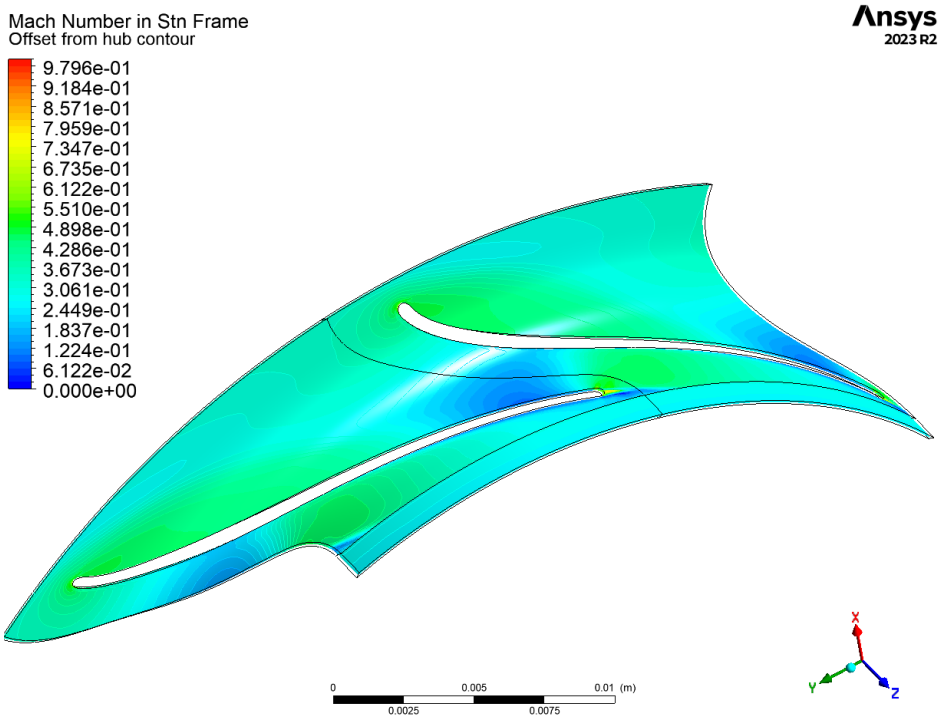


*Figure B.6: Contour plot of the Mach number in the stationary frame.*

## B.3 Pressure plots

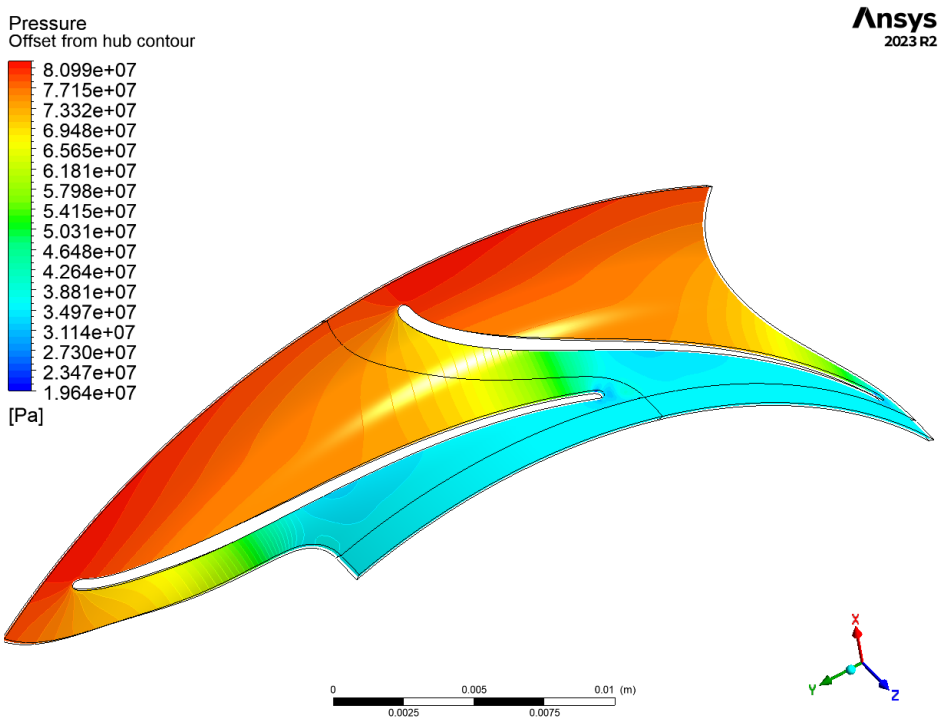


*Figure B.7: Contour plot of the static pressure.*

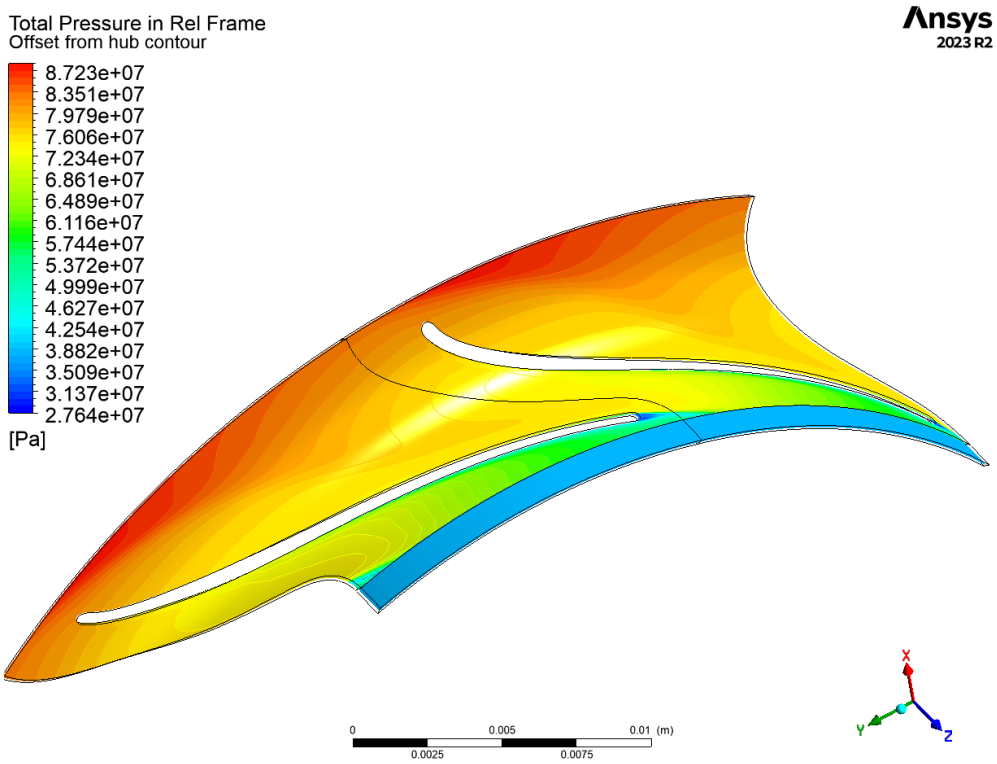


*Figure B.8: Contour plot of the total pressure in the relative reference frame.*

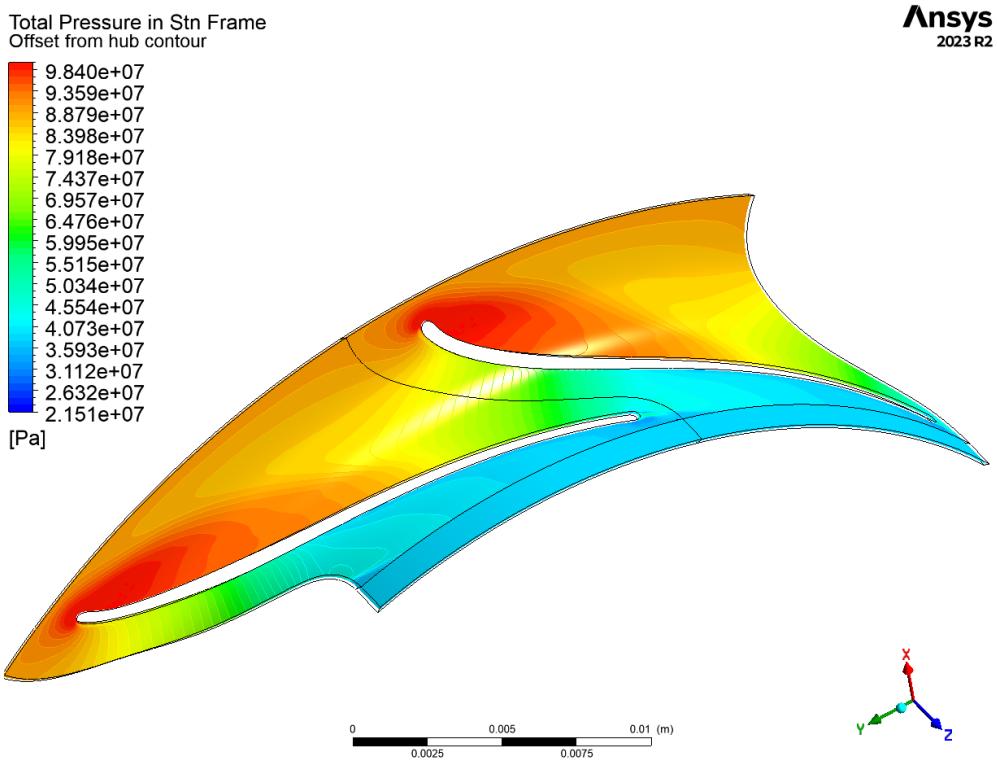


*Figure B.9: Contour plot of the total pressure in the stationary reference frame.*

## B.4 Temperature plots

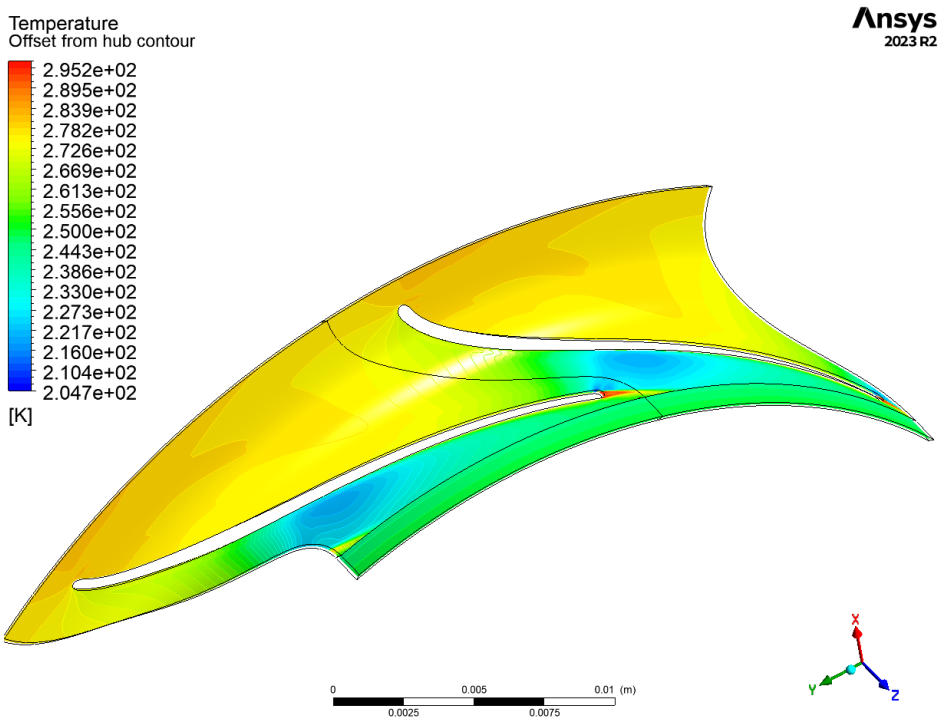


*Figure B.10: Contour plot of the static temperature.*

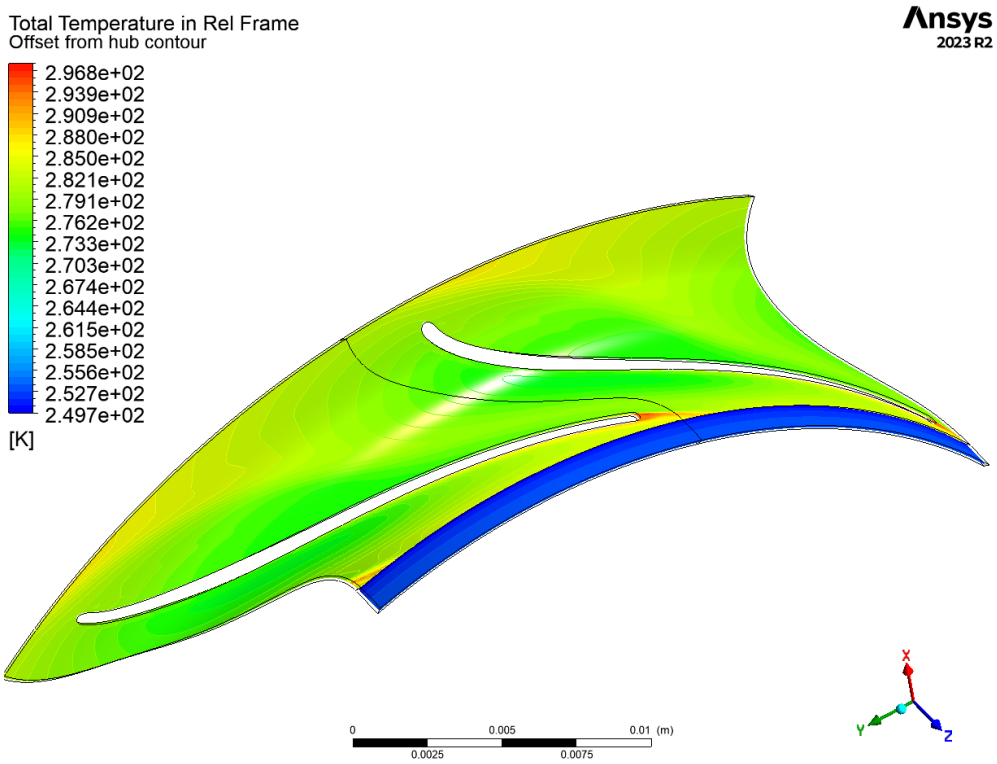


*Figure B.11: Contour plot of the total temperature in the relative reference frame.*

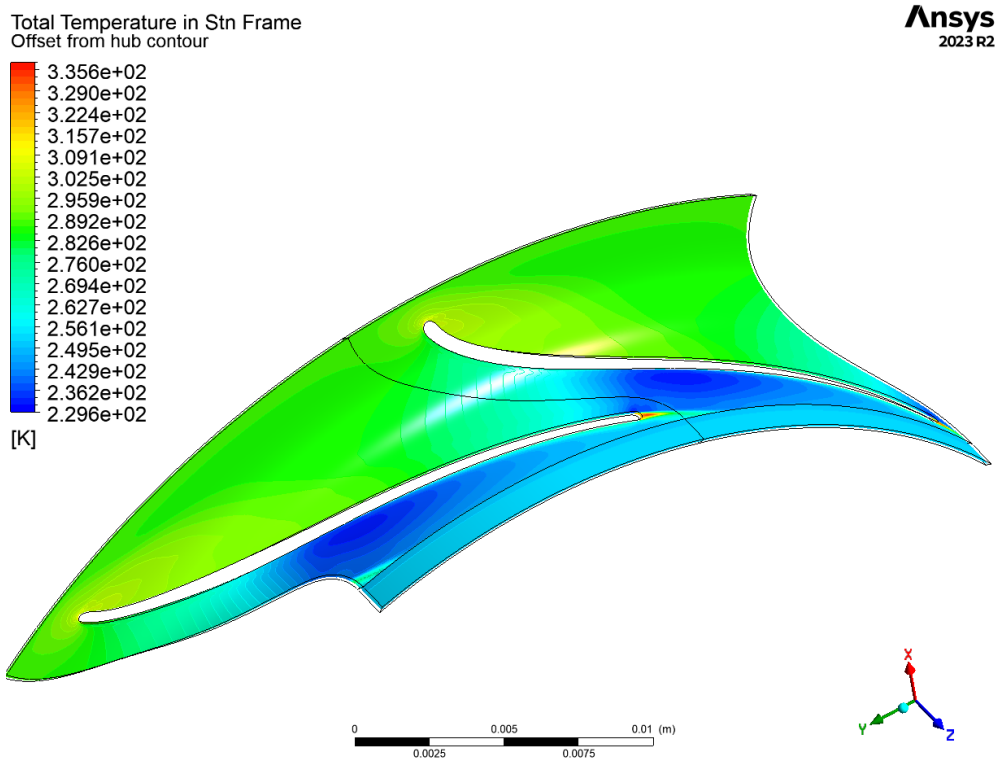


*Figure B.12: Contour plot of the total temperature in the stationary reference frame.*

## B.5 Density plots

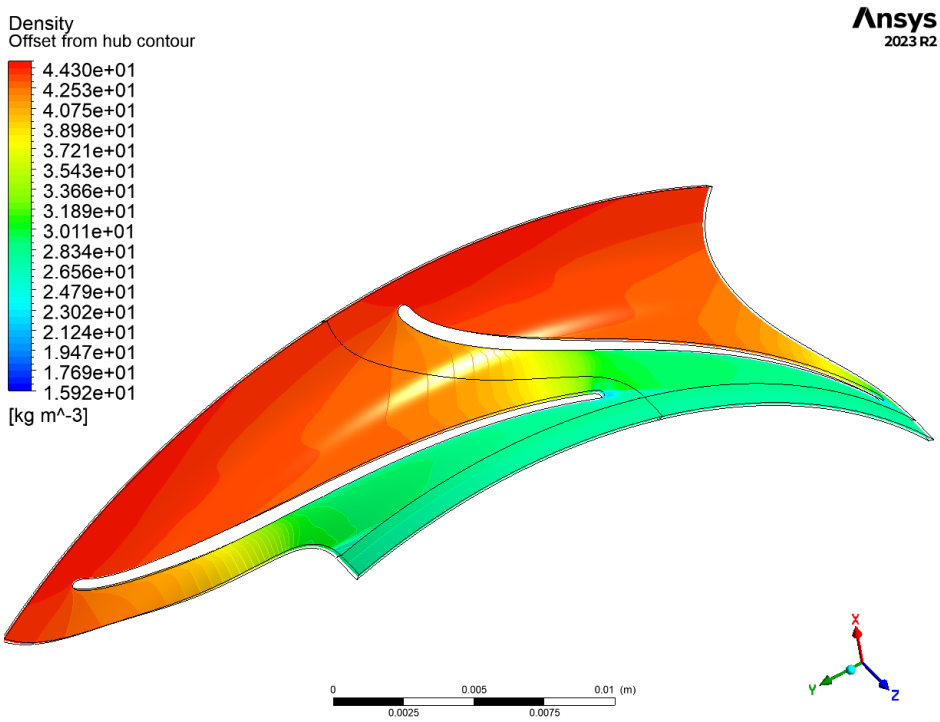


*Figure B.13: Contour plot of the static density.*

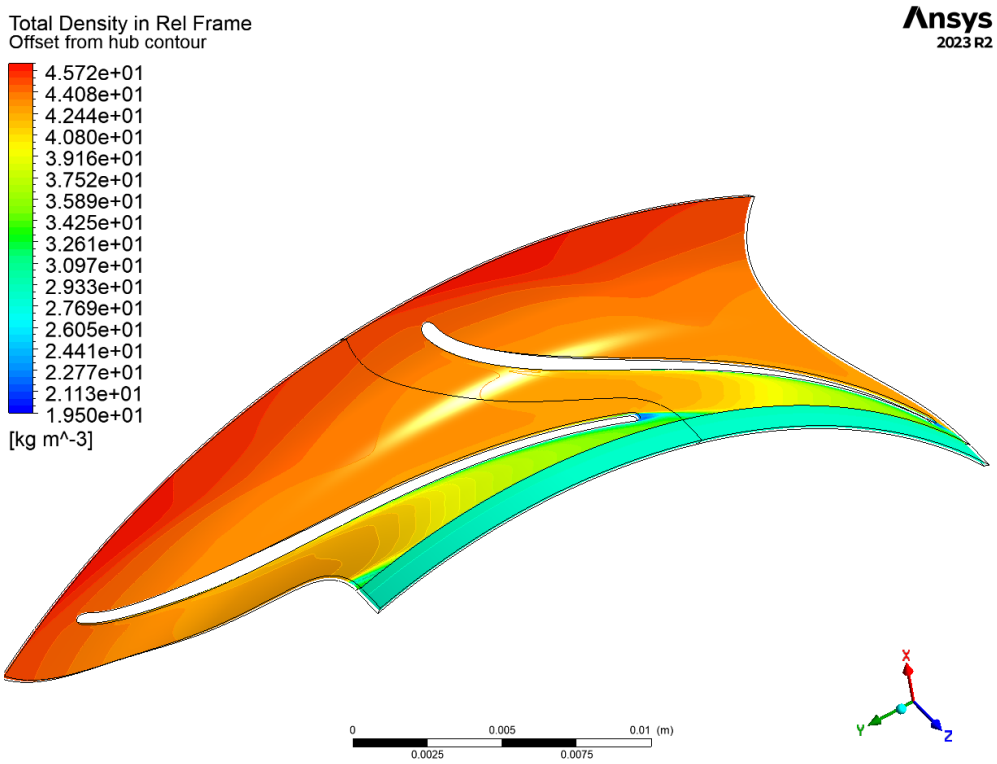


*Figure B.14: Contour plot of the total density in the relative reference frame.*

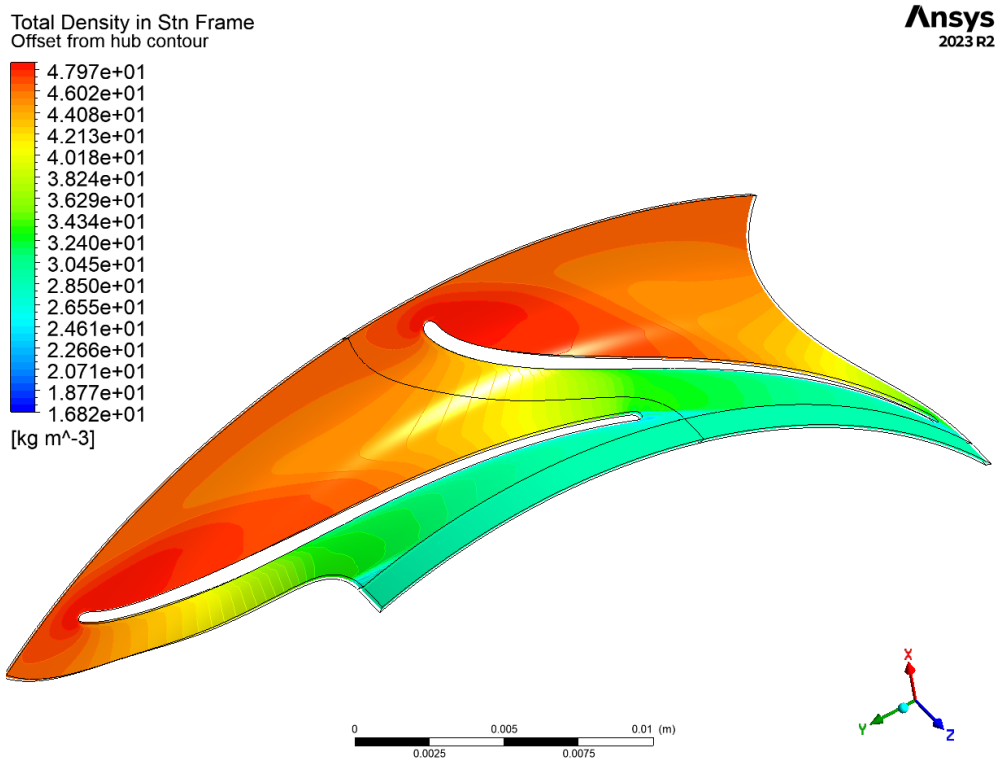


*Figure B.15: Contour plot of the total density in the stationary reference frame.*

## B.6 Enthalpy plots

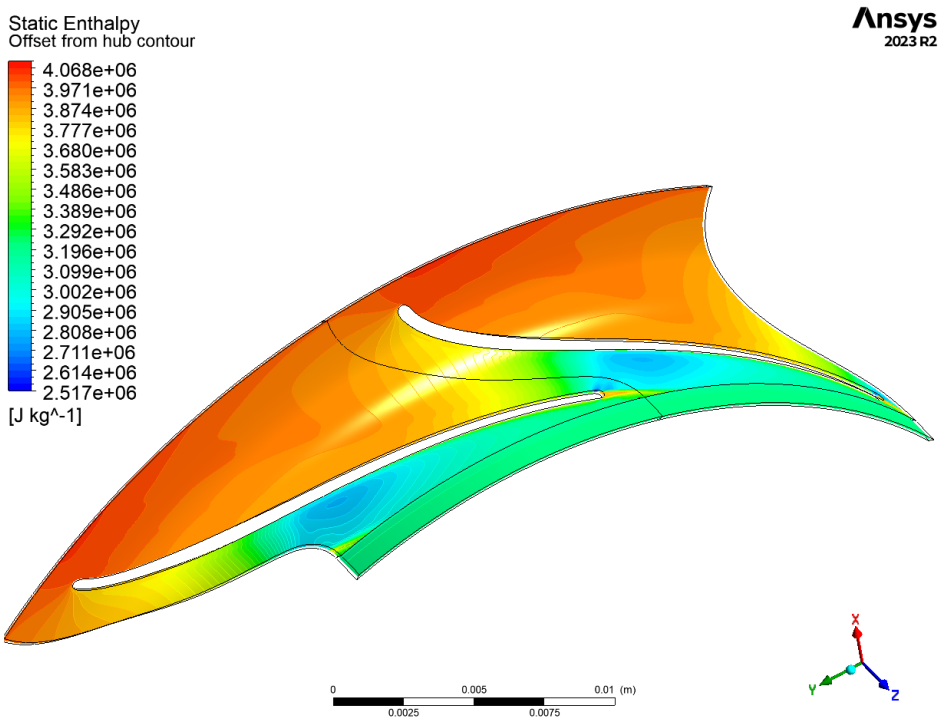


*Figure B.16: Contour plot of the static enthalpy.*

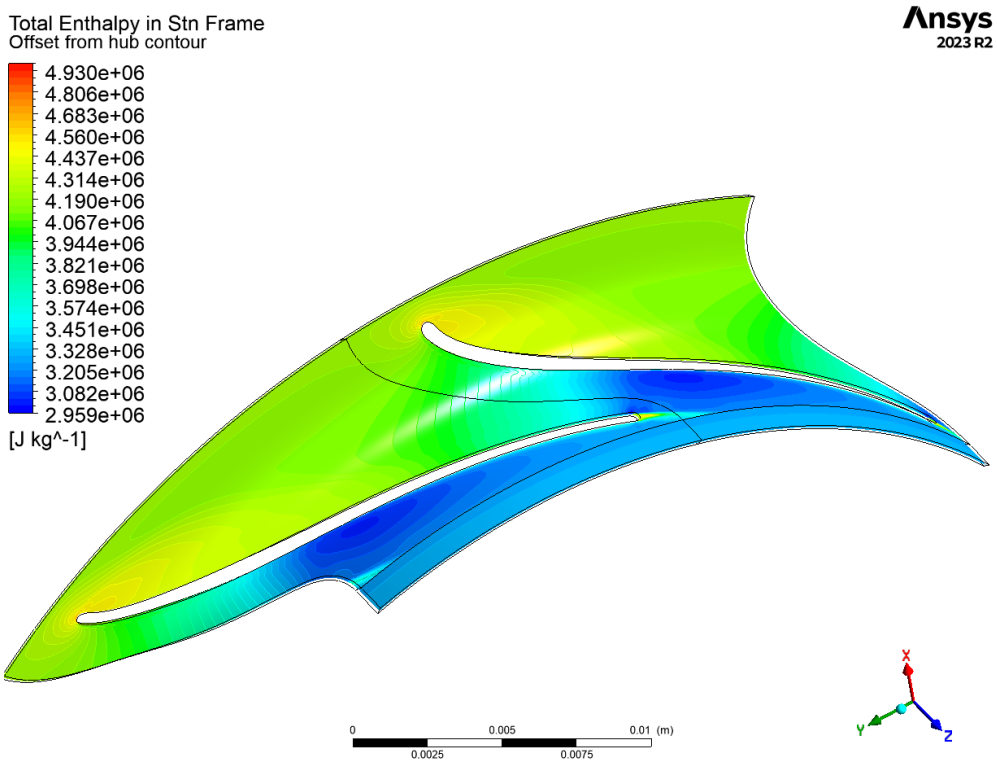


*Figure B.17: Contour plot of the total enthalpy in the stationary reference frame.*